UNIVERSITY OF CALIFORNIA,
IRVINE

Continuum Reverberation Mapping of Active Galactic Nuclei via Robotic Observations

DISSERTATION

submitted in partial satisfaction of the requirements
for the degree of

DOCTOR OF PHILOSOPHY

in Physics

by

John William Montano

Dissertation Committee:
Professor Aaron J. Barth, Chair
Professor Kevork Abazajian
Associate Professor Paul Robertson

2025

TABLE OF CONTENTS

LIST OF FIGURES

LIST OF TABLES

ACKNOWLEDGMENTS

The text of Chapter 3 of this dissertation is an adaption of the material as it appears in Montano, J. W., Hengxiao, G., Barth, A. J., U, V., Remigio, R., Gonzalez-Buitrago, D. H., & Hernandez Santisteban, J. V. (2022). Optical Continuum Reverberation in the Dwarf Seyfert Nucleus of NGC 4395. The Astrophysical Journal Letters, 934(2), L37. DOI 10.3847/2041-8213/ac7e54. Used with permission from the author and the Astrophysical Journal. The coauthors listed in this publication are Hengxiao Guo, Aaron J. Barth, Vivian U, Raymond Remigio, Diego H. Gonzalez-Buitrago, and Juan V. Hernandez Santisteban.

The figures of portions of Chapter 5 of this dissertation are an adaption of the material as it appears in Kara, E., Barth, A. J., Cackett, E. M., Gelbord, J., Montano, J., Li, Y., Santana, L., Horne, K., Alston, W. N., Buisson, D., Chelouche, D., Du, P., Fabian, A. C., Fian, C., Gallo, L., Goad, M. R., Grupe, D., Gonzalez Buitrago, D. H., Hernandez Santisteban, J. V., Kaspi, S., Hu, C., Komossa, S., Kriss, G. A., Lewin, C., Lewis, T., Loewenstein, M., Lohfink, A., Masterson, M., McHardy, I. M., Mehdipour, M., Miller, J., Panagiotou, C., Parker, M. L., Pinto, C., Remillard, R., Reynolds, R., Rogantini, D., Wang, J. -M.,Wang, J., & Wilkins, D. (2023). UV-Optical Disk Reverberation Lags despite a Faint X-ray Corona in the Active Galactic Nucleus Mrk 335. The Astrophysical Journal, 947, 62. DOI 10.3847/1538-4357/acbcd3. This material is used with permission from the author Dr. Erin Kara and the Astrophysical Journal. The coauthors listed in this publication are Aaron J. Barth, Edward M. Cackett, Jonathan Gelbord, John Montano , Yan-Rong Li, Lisabeth Santana, Keith Horne, William N. Alston, Douglas Buisson, Doron Chelouche, Pu Du, Andrew C. Fabian, Carina Fian, Luigi Gallo, Michael R. Goad, Dirk Grupe, Diego H. Gonzalez Buitrago, Juan V. Hernandez Santisteban, Shai Kaspi, Chen Hu, Stefanie Komossa, Gerard A. Kriss, Collin Lewin, Tiffany Lewis, Michael Loewenstein, Anne Lohfink, Megan Masterson, Ian M. McHardy, Missagh Mehdipour, Jake Miller, Christos Panagioutou, Michael L. Parker, Ciro Pinto, Ron Remillard, Christopher Reynolds, Daniele Rogantini, Jian-Min Wang, Jingyi Wang and Dan Wilkins.

This work makes use of observations from the Las Cumbres Observatory global telescope network. LCO telescope time was granted by NOIRLab through the Mid-Scale Innovations Program (MSIP). MSIP is funded by NSF. This paper is based on observations made with the MuSCAT3 instrument, developed by the Astrobiology Center and under financial supports by JSPS KAKENHI (JP18H05439) and JST PRESTO (JPMJPR1775), at Faulkes Telescope North on Maui, HI, operated by the Las Cumbres Observatory. We thank the staff of Las Cumbres Observatory and particularly Emily Manne-Nicholas for invaluable assistance in planning the MuSCAT3 observations. We thank Ying Zu for helpful discussions. Research at UC Irvine was supported by NSF grant AST-1907290. DHGB acknowledges CONACYT support #319800. JVHS acknowledges support from STFC grant ST/R000824/1. We acknowledge Haleakalā as a land of spiritual and cultural significance to the Native Hawaiian people. The use of this important site to further scientific knowledge is done so with appreciation and respect.

This work is also based on observations collected at Schmidt 67/92 telescope (Asiago Mount Ekar, Italy) INAF - Osservatorio Astronomico di Padova.

The Liverpool Telescope is operated on the island of La Palma by Liverpool John Moores University in the Spanish Observatorio del Roque de los Muchachos of the Instituto de Astrofisica de Canarias with financial support from the UK Science and Technology Facilities Council.

This work makes use of observations collected at the Centro Astronomico Hispanoen Andaluci (CAHA) at Calar Alto, operated jointly by the Andalusian Unviversities and the Instituto de Astrofisica de Andalucia (CSIC). Funding for the Lijiang 2.4 m telescope has bene provided by the Chinese Academy of Sciences (CAS) and the People's Government of Yunnan Province.

Support for HST program GO-16196 was provided by NASA through a grant from the Space Telescope Science Institute, which is operated by the Association of Universities for Research in Astronomy, Inc., under NASA contract NAS5-26555.

I would like to thank, firstly, my advisor Aaron Barth for taking me as his student. I am highly grateful for his patience and wisdom provided during my graduate career. I came into graduate school without direction of what I wanted to do in research although I knew it would be in astronomy. Despite never meeting before we had a connection between a previous graduate student of the group, now a Professor at my undergraduate Cal State San Bernardino, Carol Hood. This short link made me confident enough to ask Aaron about his research despite not having a scheduled time with him when touring UCI. When I was accepted into the UCI PhD program I was confident in sticking to observational astronomy and I could do that with Aaron. Despite my shortcomings and anxiety Aaron has been resolute in staying as my advisor. It is thanks to him that I was introduced to the STORM 2 project and was able to be a part of it.

The collaborative group of STORM 2 is another group of people I would like to thank as their feedback and participation has been a large part of my growth as a scientist. I am grateful to have been allowed to work on such a novel data set and develop skills as a part of it.

I would like to thank my friends, those made in my undergraduate and graduate time. The new friends I made in graduate school astound me in their kindness towards me. We've become such good friends that our lives, although paths may diverge, have become intertwined. I was given the opportunity to connect with them and share myself. It is thanks to them that I have explored nature even more and explored the world bit by bit. To Rob and Bri, I do not know what I did to deserve such friends and I never want to stop calling you two my friends.

I would like to thank the individuals within Cal-Bridge and the program itself. I can clearly recall applying for Cal-Bridge as an undergraduate. I was working in a material sciences lab and applied along side my friend, Alessa Ibrahim (now Wiggins). I was afraid of applying,

thinking it would not be for me, yet we both were accepted into the program. This was when Cal-Bridge was a smaller program than it is now (since then it has expanded state-wide with more funding and supports different fields). I was assigned two mentors, Sara Callori as part of my home institution and Kevork Abazajian (at UCI) outside of it. Together they would regularly check on my progress as a student and helped me develop myself to apply for graduate school. With their guidance and support, along with workshops, conferences and a lot more they showed me who I could be.

I would like to thank those from my undergraduate institution Cal State San Bernardino in the department of physics, specifically Carol Hood, Sara Callori, Maureen Murphy and Laura Woodney. They served as inspiration of who I wanted to be coming into grad school, although my career choice has changed I still look up to them. Part of my CSUSB physics experience was the Murillo Family Observatory. It was one of my first real exposures to astronomy and is what inspired me to actively pursue research. It is through that small observatory that I was able to gain experience and confidence. Being a part of that observatory led me to traveling to Kitt Peak mountain to observe a clear unobstructed night sky, it is one of few times in my life I have been able to see the sky unobstructed and filled with stars.

There are many more people I would like to thank, including my family and those who have gone unnamed. Thank you all for your support, I would not be the individual I am today without all of you.

VITA

John William Montano

EDUCATION

Doctor of Philosophy in Physics **2025**
University of California, Irvine *Irvine, California*

Bachelor of Science in Physics **2019**
California State University San Bernardino *San Bernardino, California*

RESEARCH EXPERIENCE

Graduate Research Assistant **2019–2025**
University of California, Irvine *Irvine, California*

Undergraduate Research Assistant **2018**
University of California, Irvine *Irvine, California*

Undergraduate Research Assistant **2016–2018**
California State University, San Bernardino *San Bernardino, California*

TEACHING EXPERIENCE

UCI Teaching Assistant

Basic Physics II **Summer 2024**
University of California, Irvine
Physics 3B

Classical Physics **Spring 2024**
University of California, Irvine
Physics 7D

Basic Physics II **Summer 2023**
University of California, Irvine
Physics 3B

Cosmology **Spring 2023**
University of California, Irvine
Physics 20B

Fundamentals of Experimental Physics **Fall 2022**
University of California, Irvine
Physics 52A

Intro to Astronomy **Summer 2022**
University of California, Irvine
Physics 20A

Classical Physics **Fall 2020**
University of California, Irvine
Physics 7C

Basic Physics III **Spring 2020**
University of California, Irvine
Physics 3C

Intro Math Methods **Fall 2019**
University of California, Irvine
Physics 2

Cal-Bridge Physics Tutor **2019–2020**
University of California, Irvine

FIRST-AUTHOR REFEREED JOURNAL PUBLICATIONS

Reverberation Mapping of Dwarf Seyfert Galaxy NGC 4395 **2022**
Astrophysical Journal Letters

FIRST-AUTHOR SUBMITTED JOURNAL PUBLICATIONS

AGN STORM 2. XII. Ground-based Optical Photometry and Lag-Measurements of Mrk 817 **2025**
Astrophysical Journal

OTHER REFEREED JOURNAL PUBLICATIONS

AGN STORM 2. X. The Origin of the Interband Continuum Delays in Mrk 817 **2024**
Astrophysical Journal

AGN STORM 2. VII. A Frequency-resolved Map of the Accretion Disk in Mrk 817: Simultaneous X-ray Reverberation and UVOIR Disk Reprocessing Time Lags **2024**
Astrophysical Journal

AGN STORM 2. IX. Studying the Dynamics of the Ionized Obscurer in Mrk 817 with High-resolution X-ray Spectroscopy **2024**
Astrophysical Journal

Intensive Swift and LCO Monitoring of PG 1302-102: Active Galactic Nucleus Disk Reverberation Mapping of a Supermassive Black Hole Binary Candidate **2024**
Astrophysical Journal

AGN STORM 2. V. Anomalous Behavior of the C IV Light Curve of Mrk 817 **2024**
Astrophysical Journal

AGN STORM 2. VI. Mapping Temperature Fluctuations in the Accretion Disk of Mrk 817 **2024**
Astrophysical Journal

AGN STORM 2. IV. Swift X-ray and Ultraviolet/OPtical Monitoring of Mrk 817 **2023**
Astrophysical Journal

AGN STORM 2. II. Ultraviolet Observations of Mrk 817 with the Cosmic Origins Spectrograph on the Hubble Space Telescope **2023**
Astrophysical Journal

UV-Optical Disk Reverberation Lags despite a Faint X-Ray Corona in the Active Galactic Nucleus Mrk 335 **2023**
Astrophysical Journal

AGN STORM 2. I. First results: A Change in the Weather of Mrk 817 **2021**
Astrophysical Journal

SOFTWARE

pyautophot `https://github.com/jwontano/autophot`
Python pipeline that performs photometry for heterogeneous image sets for reverberation mapping campaigns to produce intercalibrated uncertainty-adjusted light curves for lag measurements.

ABSTRACT OF THE DISSERTATION

Continuum Reverberation Mapping of Active Galactic Nuclei via Robotic Observations

By

John William Montano

Doctor of Philosophy in Physics

University of California, Irvine, 2025

Professor Aaron J. Barth, Chair

Continuum reverberation mapping is an observational technique that allows one to measure spatial information of the sub-parsec regions in active galactic nuclei (AGN) on size scales that cannot be directly resolved due to the small angular size of the AGN. Reverberation mapping (RM) makes use of the time delay between emission processes by using temporal accuracy, from high cadence observing, to achieve high spatial accuracy. This technique has grown the past decades to move beyond the structure of the broad-line region (BLR) and now to the inner region at milli-parsec scales of the accretion disk.

The Space Telescope and Optical Reverberation Mapping (STORM) 2 project is a multi-wavelength observing campaign of Markarian 817 (z=0.031455) utilizing space and ground-based facilities to measure the geometry and gas outflow behavior of the AGN. As part of my work in STORM 2, I developed a python-based light curve production code that would automate the photometric and intercalibration procedures using freely available python packages such as Astropy and PyCALI. The program produces light curves for the multiple broad-band filters and telescopes used in a reverberation mapping observing campaign, which are the primary data products used to measure time lags.

This dissertation presents the results of multiple reverberation mapping projects completed during my graduate career. These RM projects focus on optical continuum observations to

measure inter-band time lags in an attempt to characterize the sub-parsec regions of AGN. Each project utilizes the automated photometry code I developed and lag measurements were completed either by myself or collaborators. The AGN that I provided light curves for are NGC 4395, Mrk 335, Mrk 817, and PG 1302-02. For NGC 4395 and Mrk 817 I measured inter-band time-lags to produce a lag-spectrum per object with multiple methods. Both NGC 4395 and Mrk 817 display lag spectra that fit a $\lambda^{4/3}$ power law, however they deviate from the expected thin accretion disk model. From my work Mrk 817 currently has the longest high-cadence light curves of any AGN and is one of the first continuum RM objects to show time lags changing on short timescales. NGC 4395 is one of the first intermediate mass black holes on which optical inter-band continuum reverberation mapping has been performed, providing a unique data point for continuum RM scaling relations.

Chapter 1

Active Galactic Nuclei - Black Holes

1.1 A Very Short History of Black Holes and Active Galactic Nuclei

As massive stars reach the end of their lifetimes and radiative pressure from fusion can no longer counteract the force of gravity, they then collapse under their own gravity. The collapse happens at extraordinary speeds, reaching relativistic velocities, and the mass (and metallicity) determine the outcome. One of those outcomes is a black hole (BH), which may grow over cosmic time up to masses on the order of millions to billions of solar masses (Kormendy & Ho, 2013). The growth of black holes can happen through many mechanisms, such as tidal disruption events where stars veer close to the BH and gas is stripped from them; or galactic mergers where black holes have a chance to merge with other black holes. Black holes are not separate from the galaxies they inhabit and are thought to influence each others growth. It is now well-known that every galaxy has a black hole so with such a ubiquitous nature they are thought to play a role in the growth/evolution of galaxies. While

they may be ever-present in galaxies, the space they occupy is very small in comparison to the host, which makes observing them incredibly difficult.

The reality of studying black holes is that they themselves do not emit any light, because of the massive gravitational potential well that not even light can escape. Instead, we study the space around a black hole such as the accretion disk, broad-line region (BLR), narrow-line region (NLR), jets, the dusty torus, or the surrounding gas under the BH's gravitational influence. These are some of the basic components that mark a black hole as an active galactic nucleus (AGN). AGN are incredibly luminous reaching luminosities comparable to that of the galaxies they reside in. Defining and classifying AGN is a whole field by itself, as AGN emit light throughout almost the entire energy spectrum.

The "first" discovery of AGN began with quasars (quasi-stellar objects). When observed, they looked like stars (point-like), but exhibited strong emission lines with incredibly broad wings over a wide wavelength range. To understand the significance of such broad emission lines we will quickly go over Doppler broadening of gravitationally bound objects. For an object that is gravitationally bound apply the virial theorem which gives $M = \frac{v^2 R}{G}$ where v is the velocity of the bound object, R is the distance to the mass, and G the gravitational constant. For objects in an orbit emitting light, the Doppler broadening of emission lines can be measured to estimate the emitting source's velocity distribution which may then be connected to our virial argument to estimate the central mass it orbits. Early research showed that the limit for unresolved nuclei was under 100 pc for Seyfert galaxies and when applied to the measured radial velocities of the broad-emission lines, which were on the order of 1000's km/s, gave an estimated mass of $M \approx 10^{9\pm1}\ M_\odot$ (Oke, 1965). At that time stellar astronomy was well-established and we knew that stellar mass ranges may be on the order of $10^{-1} - 10^2\ M_\odot$, so it was a shocking discovery that a singular object would be so massive. Black holes were thought to exist before their observational discovery; this was worked out through Einstein's theory of general relativity. Shortly after Einstein's work was

published, Schwarzschild provided an exact solution for the case of a non-rotating spherical mass. While this all happened during 1915-1916 it would not be observationally confirmed until decades later and the theory of black holes would be expanded further by others such as Subrahmanyan Chandrasekhar and Roy Kerr.

As the research of AGN has grown over the past half-century plus we have learned that, observationally, AGN do not fall into a clean or simple schematic to describe them. AGN do have taxonomic classifications that focus on the observational properties, e.g. radio emission, variability in wavelengths, or the presence or absence of emission and absorption lines. Separate from this taxonomy are the host galaxies themselves, such as Seyfert or Markarian galaxies, which commonly contain AGN. It is useful to define Seyfert galaxies here, as most of the objects in this dissertation are Seyfert galaxies. Seyfert galaxies are named after the astronomer that observed a number of galaxies with bright centers and broad emission lines, Carl K. Seyfert. Seyfert galaxies are categorized between Seyfert 1 or 2 based on their observed emission line properties. Seyfert 1 galaxies have broad and narrow emission lines, while Seyfert 2 only have narrow emission lines. One proposed explanation for the difference in emission lines is the inclination angle and dust surrounding the galaxies. Regardless of their host galaxy type, black holes pose unique observational challenges.

As previously mentioned, we cannot "look" at a black hole so all methods of observation are generally indirect and focus on matter that surrounds the black hole. Fantastic feats of ingenuity have allowed researchers to achieve high spatial resolutions to image the accretion disk. This is exemplified by the now-famous image of the Milky Way's central black hole's accretion disk as generated through the observations of the Event Horizon Telescope (Event Horizon Telescope Collaboration et al., 2019a,b). Gravitational lensing is another technique used to view distant quasars that would be too dim to view without it (Treu, 2010). Another observational method makes use of temporal resolution in lieu of spatial resolution and is known as reverberation mapping (RM).

1.2 Reverberation Mapping

1.2.1 RM History

Blandford & McKee (1982) provided the baseline methodology to reverberation mapping properly formalizing it, with information on what to possibly expect and how to perform it. This is not to say that it was the first use of RM; for example Bahcall et al. (1972) applied the method to gases such as in nebulae or novae. The general idea of "reverberations" was not novel at the time, and it was found to be applicable to certain celestial objects, AGN being one of them. During this time the focus was on emission line responses from the BLR which typically has lags on the order of 10's of days for nearby super-massive black holes (SMBHs) and even longer for quasars (Cackett et al., 2021). A couple of major requirements for measuring time delays in time series are to have a cadence of at least at a fraction of the time delay, and that the duration of observing be longer than the time delay expected (Peterson & Horne, 2004). This requirement however is under some simple assumptions that will be explored in this section.

As observational technology advanced from photographic plates and phototubes to the invention of the charged-coupling device (CCD), reverberation mapping became more accessible and feasible. The importance and capabilities that CCDs have enabled for astronomy cannot be overstated. The short review paper of CCDs and their history in astronomy by Lesser (2015) provides a concise background. CCDs have high quantum efficiencies and are able to be exposed repeatedly then read off to generate images instantly (in comparison to previous methods). As astronomy grew, so too were reverberation mapping projects being published and collaboration efforts made. The International AGN Watch was a collaboration focused on monitoring multiple AGN such as NGC 5548, NGC 4151, Akn 564, and Fairall 9. Most of the efforts of AGN watch were published during the 1990's and early 2000's (Clavel et al., 1991; Peterson et al., 1991, 1992; Dietrich et al., 1993; Peterson et al., 1994, 2002).

The Lick AGN monitoring project (LAMP) furthered the progress of RM by observing 12 objects and creating a sample for other researchers to use (Bentz et al., 2008, 2009; Walsh et al., 2009; Woo et al., 2010).[1] LAMP served as a great example to the rest of the AGN community as it used a collection of facilities and produced lag-measurements for use of mass estimates. It continued in the future and widened the parameter space it explored in terms of AGN (U et al., 2022).

About a decade later with telescope networks such as the Las Cumbres Observatory global telescope network (LCOGT), observing campaigns for multiple objects at a time are possible. Around the mid-2010s, the LCOGT group had commissioned multiple 1 meter telescopes and other large sky surveys had been underway such as the Sloan Digital Sky Survey (SDSS). A new collaboration group created the Space Telescope and Reverberation Mapping project which made use of multiple space telescopes and ground-based observatories to monitor the AGN NGC 5548 for roughly a year at a high cadence. This was one of the first successful instances of a multi-wavelength high-cadence project in RM (De Rosa et al., 2015a; Edelson et al., 2015; Fausnaugh et al., 2016; Goad et al., 2016). One of the main goals of AGN STORM was to measure disk continuum time delays and they did, showing a lag-spectrum that shows time-lags increase with wavelength. This project solidified the field of disk continuum reverberation mapping, sometimes referred to as Intensive Disk Reverberation Mapping (IDRM) or Intensive Broadband Reverberation Mapping (IBRM). Regardless of acronym, the focus is on the inner-most regions of the AGN.

1.2.2 RM and Lag Measurement Techniques

There are a few major assumptions that are made with reverberation mapping. These were outlined originally for broad-line region RM, yet are still relevant to disk continuum RM which will be discussed in the next section. The assumptions are

[1] `https://www.physics.uci.edu/~barth/lamp.html`

1. There exists an irradiating central source, such as a hot X-ray plasma corona above the BH;

2. There is a relationship/correlation between the ionizing continuum and the responding continuum (or line);

3. Light-travel time is the most relevant timescale: $\tau = R/c$.

To understand these assumptions and what they imply for observing we should analyze no. 2. If the continuum and responding emission line are related, not necessarily in a linear relation, we can account for the response with a transfer function and equation. The transfer equation is defined as

$$L(t) = \int \Psi(\tau) C(t-\tau) d\tau, \tag{1.1}$$

where $L(t)$ is the emission line light curve, $\Psi(\tau)$ is the transfer function, and $C(t-\tau)$ is the continuum light curve. The transfer function contains information on how the continuum light curve is being convolved into the observed responding light curve. This does come along with the caveat that it is a one-dimensional view of the transfer equation, and it may assume a linear relationship. The general assumption is that responding light curves are smoothed and shifted versions of the driving light curve. To solve for the transfer function one needs to find the Green's function for the system and finding said solution is highly dependent on the quality and cadence of the light curves used (Peterson, 1997). Since data quality, in signal-to-noise and cadence, was not as high compared to today's standards a cross-correlation analysis sufficed.

The interpolated cross-correlation function (ICCF) analysis is fundamental now to reverberation mapping and one of its strengths is that it makes no physical assumptions of the data. It is a straightforward mathematical analysis of two time series that is used in a variety

of fields, such as in exoplanets or medicine (Saylor et al., 2018; Rezaeitavabe et al., 2024; Schill et al., 2023). That being said, there are additions to the cross-correlation analysis that provide conservative uncertainties to the time delays measured. Today the cross-correlation analysis is a standard practice, take for example the program PyCCF which is a python version of the cross-correlation analysis that was done in languages like C,C# and IDL in the past. PyCCF utilizes a process called Flux-Redistribution/Random Subset Selection (FR/RSS) to generate the uncertainties via Monte-Carlo methods (Gaskell & Peterson, 1987a; Peterson et al., 1998a). Flux-Redistribution/Random Subset Selection are two separate processes joined to generate statistically sound uncertainties based on the bootstrap method. Flux-Redistribution deals with the uncertainties the flux-values have by assuming a standard Gaussian distribution. Each flux value is altered by a random Gaussian deviate within a single σ (standard deviation) of the uncertainties distribution. Added to that is the random subset selection that randomly samples the light curves with redundant selections allowed. The sampling is repeated to generate a correlation coefficient r distribution which is then used to gain the mean and standard deviation of r. The two together then create random realizations of the light curve N amount of times to generate a cross-correlation centroid distribution (CCCD) and a cross-correlation peak distribution (CCPD) along with a cross-correlation curve. The CCCD and CCPD are then used to estimate the lag by taking their median value and the root-mean-square (rms) width for uncertainty.

The CCF technique is tied to the transfer equation as the CCF's integral form is

$$F_{\mathrm{CCF}}(\tau) = \int L(t)C(t-\tau)dt \tag{1.2}$$

which is similar in form already to Eq. 1.1. To connect the CCF to the transfer function we apply the autocorrelation function (ACF). The autocorrelation function is

$$F_{\mathrm{ACF}}(\tau) = \int C(t)C(t-\tau)dt \tag{1.3}$$

(how much does the series correlate with itself and may also serve to assess periodicity within a series) which will be inserted into the CCF after making substitutions for $L(t)$ and manipulating the integrals which results in the CCF in the form of

$$F_{\mathrm{CCF}}(\tau) = \int \Psi(\tau') F_{\mathrm{ACF}}(\tau - \tau') d\tau'. \tag{1.4}$$

The CCF as shown above in Eq. 1.4 is the convolution of the transfer function and the ACF. The cross-correlation distributions and curve may inform one of some details, e.g. an asymmetry between the peak and centroid lag suggest that the transfer function has an extended tail.

Different time-delay measurement methods used include Just Another Vehicle for Estimating Lags In Nuclei (JAVELIN) (Zu et al., 2010) and PyROA (Rolling Optimal Average) (Donnan et al., 2021). These methods do make some physical assumptions, such as a driving light curve being used that is generated from a reference light curve. These methods will be explored in other chapters as they will be used to measure lags and compared to each other.

For a recent review of reverberation mapping the work by Cackett et al. (2021) goes into the different wavelength regimes such as X-rays and the Infrared which will not be heavily discussed in this work.

1.3 Disk Continuum RM

Accretion disk continuum reverberation mapping utilizes the same principles applied to broad-line region (BLR) reverberation mapping; the difference is in the spatial extent within the AGN and the use of broad-band photometry instead of spectroscopy. Time-delays for an accretion disk are radially stratified, increasing as you move out farther from the central

engine. To compare the two regions, BLR time-delays for a Seyfert 1 AGN within the mass ranges $10^8 - 10^9$ $M_\odot$ may range from 10 to 100+ days, so the observational requirements for measuring a time-delay must be at least as long as the expected time-delay (this is just to probe the lag, to fully map the transfer function would take much longer). For AGN accretion disks, the lags may on the order of less than a day to days for a Seyfert 1 AGN. The inner parts of the accretion disk produce even shorter lags, thus the observational requirements, primarily the cadence, need to be on a daily basis or shorter (the greatest difficulty coming from observing X-rays and far-UV). As mentioned before this is possible with multiple telescopes collectively observing, which may result in a sub-daily or daily cadence as will be shown in later chapters.

A concern that may arise is how the methods mentioned previously are able to measure a lag when the sampling may be close to the size of the lag. There are limitations to the measurements made based on how long an object is observed and how often. The largest effects are from the lag-measurement techniques themselves and how they differ. The differences in uncertainties from methods is frequently pointed out, for example Gaskell (2024) examines how lag-measurement uncertainties are generally under or overestimated depending on what method you use. Another example is the work by Yu et al. (2019), where simulated light curves are used to test what parameters have the greatest effect on the uncertainties per method. Light curves can be treated as smooth continuous functions, and when measurements are unevenly sampled in time, the light curves are interpolated (or generated from a fitted model) in order to sample the lag and uncertainty. Another limitation may be exemplified in projects such as the Zwicky Transient Facility (ZTF) survey reverberation mapping by Guo et al. (2022) where they began with the Million Quasar Catalog (MQC), a list of over 1.5 million AGN, to find suitable objects for the study. In the end the MQC was reduced down to roughly 10000 objects that were eligible, and then those available within the ZTF survey reduced down to around 500 objects. The challenges of AGN reverberation mapping stem from the selection of objects that can be studied while

reserachers can improve their observing cadence or observing windows, they cannot change what objects are viable. This point also emphasizes the dependence on an AGN's variability during observation, as it is possible to have such low variability that methods such as ICCF would fail to measure any significant lags and in those cases unfortunately, no publication would be made. A major assumption made with AGN light curves is that their variability may be modeled by a damped random walk (DRW), which has been tested and modeled with a great example coming from the SDSS projects showing the model fits to a wide-range of AGN (Zu et al., 2013; MacLeod et al., 2010). One should note that a DRW model is best-fitted to the data given and is not a full representation of the variability mechanisms in an AGN light curve.

Disk continuum RM operates in ultraviolet and optical wavelengths due to our theoretical understanding of AGN accretion disks. The standard model in disk reverberation mapping is a geometrically thin optically thick accretion disk (Shakura & Sunyaev, 1973a). The standard scenario presented for the reverberation mapping of accretion disks is the "lamp-post" reprocessing picture. As mentioned earlier, RM assumes the presence of a central engine/source. This source may be a hot plasma X-ray corona that produces synchrotron radiation from up-scattered electrons as they approach the center of the AGN and produces UV photons that will then irradiate the accretion disk (and BLR). The X-ray corona is close enough to the accretion disk to be considered co-planar and preferentially irradiates the inner regions first and then the outer disk due to light travel time.

The Shakura & Sunyaev (1973a) accretion disk model has a temperature profile of $T(R) \propto (M\dot{M})^{1/4} R^{-3/4}$, where M is the BH mass, $\dot{M}$ is the accretion rate, and R the radius. The temperature of the accretion disk affects the reprocessing of the irradiating source and has a characteristic emission wavelength of $T = Xhc/k\lambda$ where X deals with the conversion from T to λ due to a range of radii contributing to the emission at a given λ and is given as flux-weighted or responsivity-weighted value ($X = 2.49$ or $X = 3.36$), h is the Planck constant, c

the speed of light and k the Boltzmann constant. With time lags defined as light travel time $\tau = R/c$, and blackbody radiation having $\lambda \propto T^{-1}$, the temperature profile to a wavelength dependent lag profile may be rewritten as $\tau(\lambda) \propto (M\dot{M})^{1/3}\lambda^{4/3}$. The lag profile is generally reduced even further as $\tau(\lambda) \propto \lambda^{4/3}$. This gives us a simple model to compare our lag measurements to. More detailed models are present in the field, for example the theoretical thin disk model accounts for multiple parameters and is used to compare lag measurements to just an accretion disk. That model, which may be seen explained in Fausnaugh et al. (2016) section 5.3, starts with the radial profile mentioned earlier. The accretion disk temperature radial profile when accounting for the irradiation of the central source and viscous heating takes the form

$$T(R) = \left[\frac{3GM\dot{M}}{8\pi R^3\sigma} + \frac{(1-A)L_X H}{4\pi\sigma R^3}\right]^{1/4} \tag{1.5}$$

with the newly introduced variables L_X is the luminosity of the irradiator, A is the albedo of the accretion disk, H is the height of the source above the disk. The Shakura & Sunyaev (1973a) model in the majority of reverberation mapping projects is an underestimate when compared to observed lags. The issue has been dubbed as a disk size discrepancy since one can consider the light-travel time of the lag as a spatial estimate from the source to the responder.

1.3.1 Disk Size Estimates

It is well-established that disk size estimates obtained through lag measurements are extended. The extended disk size is not unique to reverberation mapping. Disk sizes have been measured through gravitational lensing and also show greater than expected disk sizes (Morgan et al., 2010, 2018). This raises the question of why are we seeing "extended" disks? It would be fair to classify this as a misnomer. For the case of continuum reverberation

mapping, we expect the lag-measurements to naively be based solely on emission from the accretion disk. This is a simplifying assumption made to grant us the basic view of what we might expect from our observations. In reality, an AGN contains a combination of emission and absorption processes from different regions with varying parameters and may be limited by our observational capacities. If one were to observe an AGN within an aperture, that could include the broad-line region, narrow-line region, dusty torus, galactic bulge, nuclear starbursts, etc.

The next section on diffuse continuum emission makes the issue of disk sizes clearer as we explore what diffuse continuum emission is and where it fits into RM. Reverberation mapping has developed rapidly over the past two decades as observational techniques and data quality have increased, so much so that the field has established measurable relations between time lags, BH mass, and luminosity. While those relations exist for BLR RM measurements, for example the $R_{\rm BLR} - L_{\rm AGN}$ relationship (Kaspi et al., 2005), it would not be a surprise to see it updated to accretion disk RM in the near future especially with the first light of the Vera Rubin Observatory which should increase the number of known AGN by orders of magnitudes. A small sample size of a luminosity-lag ($L_{5100} - \tau_{5100-5400}$) relation exists as seen by the work of Netzer (2022). It is important to investigate the history of our research fields just as much as we take part in them, as what was known 10 or 20+ years ago can illuminate both our understanding and our shortcomings in the field. Roughly 20 years ago the structure of the BLR was not mapped for any AGN, and now we can perform velocity resolved measurements to accurately model the structure of BLRs.

1.4 Diffuse Continuum Emission

In Fausnaugh et al. (2016) the diffuse continuum emission (DCE) is argued as one of the leading factors in extending the measured lags of NGC 5548. Their interpretation is that the

extended lags are due to Balmer continuum and Fe II emission specifically for the extended lags in the Swift U and ground-based u filters, which is a noted trend in RM. Another great example of extended U/u lags is with NGC 4593 shown by Cackett et al. (2018). Using the UV capabilities of the Swift space telescope, HST, and Kepler they were able to show a clear excess Balmer jump in the lag spectrum. The DCE contributions have been noted for a couple of decades, as shown by Korista & Goad (2019), and in their work show the expected Balmer and Paschen jump contributions. In the cases where the U/u band excess is not displayed/confirmed it may be ambiguous due to scatter in the lag measurements. One should be able to estimate the contribution of the DCE through spectral decomposition, which was performed in Fausnaugh et al. (2016). They simulated light curves to test what parameters most affect the lags and found that the ratio of fractional variability for line emission and continuum emission (line emission being from the BLR) can determine if a lag is extended. When the BLR emission has a higher fractional variability than the continuum emission then the line lag will dominate the observed lag. While these measurements are gained directly through the light curves other major properties in the AGN are also at play that may not be drawn out from just the light curves.

The accretion rate, $\dot{m}$, of a black hole is one of the most intrinsic parameters to modeling AGN accretion disks and emission. Changing the accretion rate in a model changes luminosity, the SED, temperature profile, accretion disk and BLR size etc. In Kammoun et al. (2019) their modeling considers accretion rate, but source height, in their model, has the greatest effect. From the same work the transfer function (response function) is shown for various values of accretion rate and source height. Accretion rate changes the amplitude of the response functions, as $\dot{m}$ increases the amplitude decreases and the function widens. This is a consequence of disk temperature decreasing due to a lower accretion rate, as the temperature profile of an accretion disk is dependent on $\dot{m}$.

Photoionization modeling of DCE has developed to allow for complex spectral components to be considered, take for example STORM 2, where disk winds are being modeled to explain the extension of the lags (this will be touched upon later in Chapter 4) (Netzer et al., 2024; Netzer, 2025). The topic of diffuse continuum emission opens up the consideration of other sources of "contamination". Disk winds are dense enough to reprocess the ionizing continuum source and in the same vein longer optical wavelengths would have reprocessed emission from the dusty torus. The greater contribution of disk winds comes from the changes to accretion rate and/or changes to the SED. How these different components are shown in the light curves is not a simple linear relationship and is difficult to decode.

Disk continuum lags are done via broad-band filter observations. Our simple assumption is that we should be able to observe the continuum emission change over time, however within the broadband filters lie many emission lines (broad, narrow and complex). This becomes clear when viewing a spectrum of an AGN compared to broad-band filter transmission curves, for example Figure 1.1 shows an HST spectrum of Mrk 817 with the ground-based filters used in STORM 2. More difficulties arise when observing the UV where the accretion disk continuum black body peaks and is most variable.

There has been a body of work to model the diffuse continuum emission since the early 2000's and before. This, although speculatively, was most likely overshadowed by the lack of observational data until the advent of projects like LAMP, STORM and others like it. Through early photo-ionization modeling it was clear that the DCE could generate enough emission to contribute to the observed lags and SED. To further prove the point this issue was likely encountered in one of the earlier RM works by Collier et al. (1999, 1998) on NGC 7469 where a disagreement was noted by Sergeev et al. (2005) between the concluding statements of Collier in contention with Berkley et al. (2000) who modeled a disk plane which would give shorter lags. This rings as the same issue we are seeing today of disk size estimates being extended in comparison to a thin disk model. There is a whole different discussion on

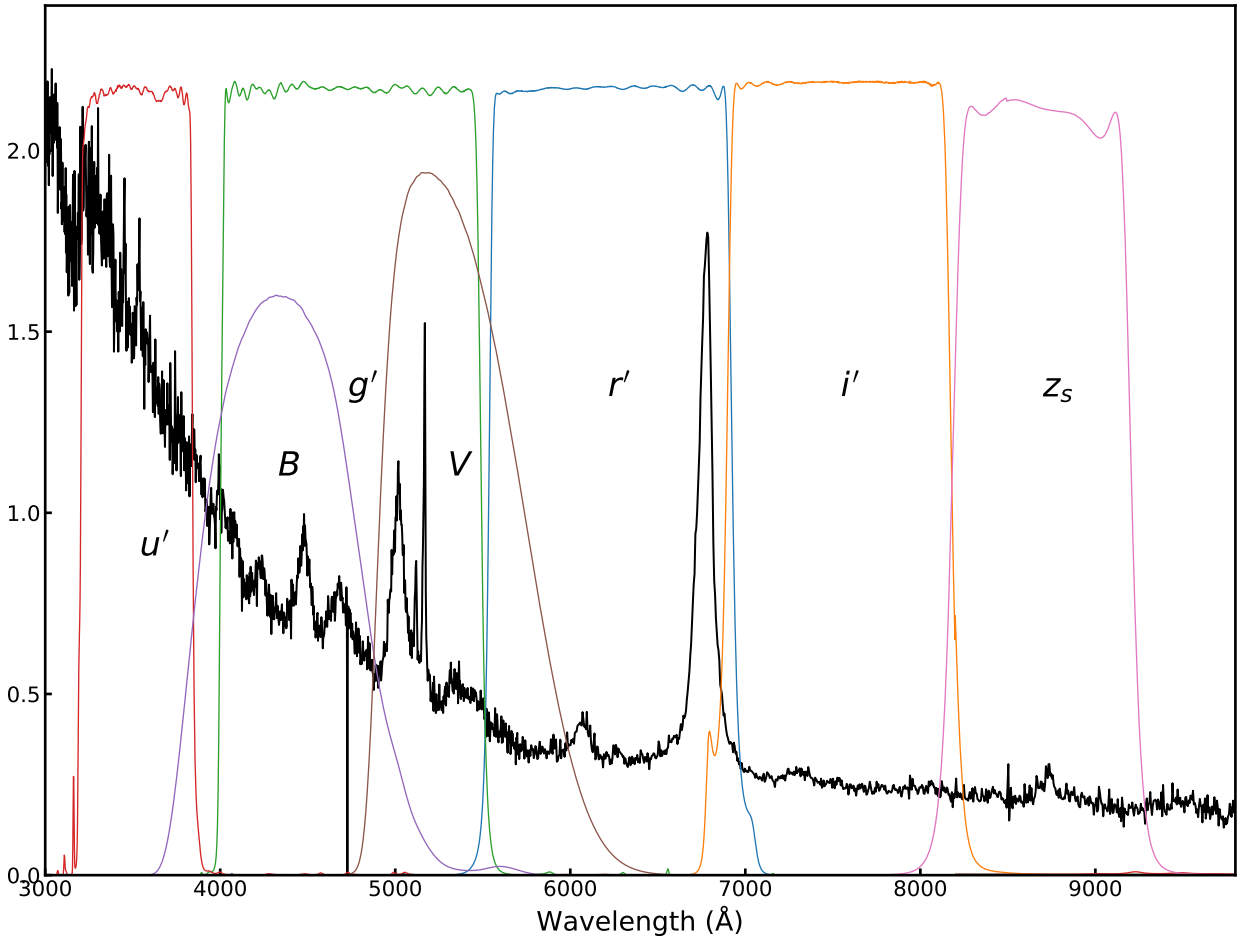

Figure 1.1: Mrk 817 STIS spectrum from the STORM 2 campaign centered on the optical wavelength range. The different colored curves show the optical filter-bands transmission curves typically used in reverberation mapping. In the r' filter lies the Hα emission line while the B,g', and V filters contain multiple emission lines.

why the characteristic sizes were sought after, such as attempting distance measurements which was unreliable due to the model dependencies, although this is still being sought after with reverberation mapping (Li et al., 2025).

To further elucidate the issue with diffuse continuum emission a view of transfer functions such as in Figure 1.2, where a log-normal function is used for a transfer function as shown in Cackett et al. (2022), to display what shapes transfer functions take. This particular model for transfer function shape is defined as

$$\Psi(t) = \frac{1}{S\sqrt{2\pi t}} \exp\left[\frac{(\ln(t) - M)^2}{2S^2}\right] \tag{1.6}$$

where M determines where the function will peak and S how broad it will be. In these cases an extended lag may come from a transfer function with a higher value of S as that would broaden it creating a long tail, whereas the left-column may better represent a disk response. The transfer functions are the convolutions that we assume are applied to the driving continuum and these cases only represent singular cases. More fitting to the issue of diffuse continuum emission would be the combination of transfer functions to account for the multiple responses. When a long tail is present the measured lags will be extended, despite the lower amplitude in the transfer function.

There are other explanations for the extended lags that consider different emission processes, geometries or disk temperature fluctuations propagating inward. It is again important to emphasize the original simple picture, the Shakura & Sunyaev (1973a) thin disk model. Deviating from that simple picture is not difficult especially when the observational data does not fully agree with it. One of the stronger agreements from the thin disk model is that the time lags will increase with wavelength by a power law ($\tau \propto \lambda^{4/3}$). Alternatives to the thin disk model include: considering the local temperature fluctuations, disks that have local scattering mediums which would affect the observed disk temperature, having the

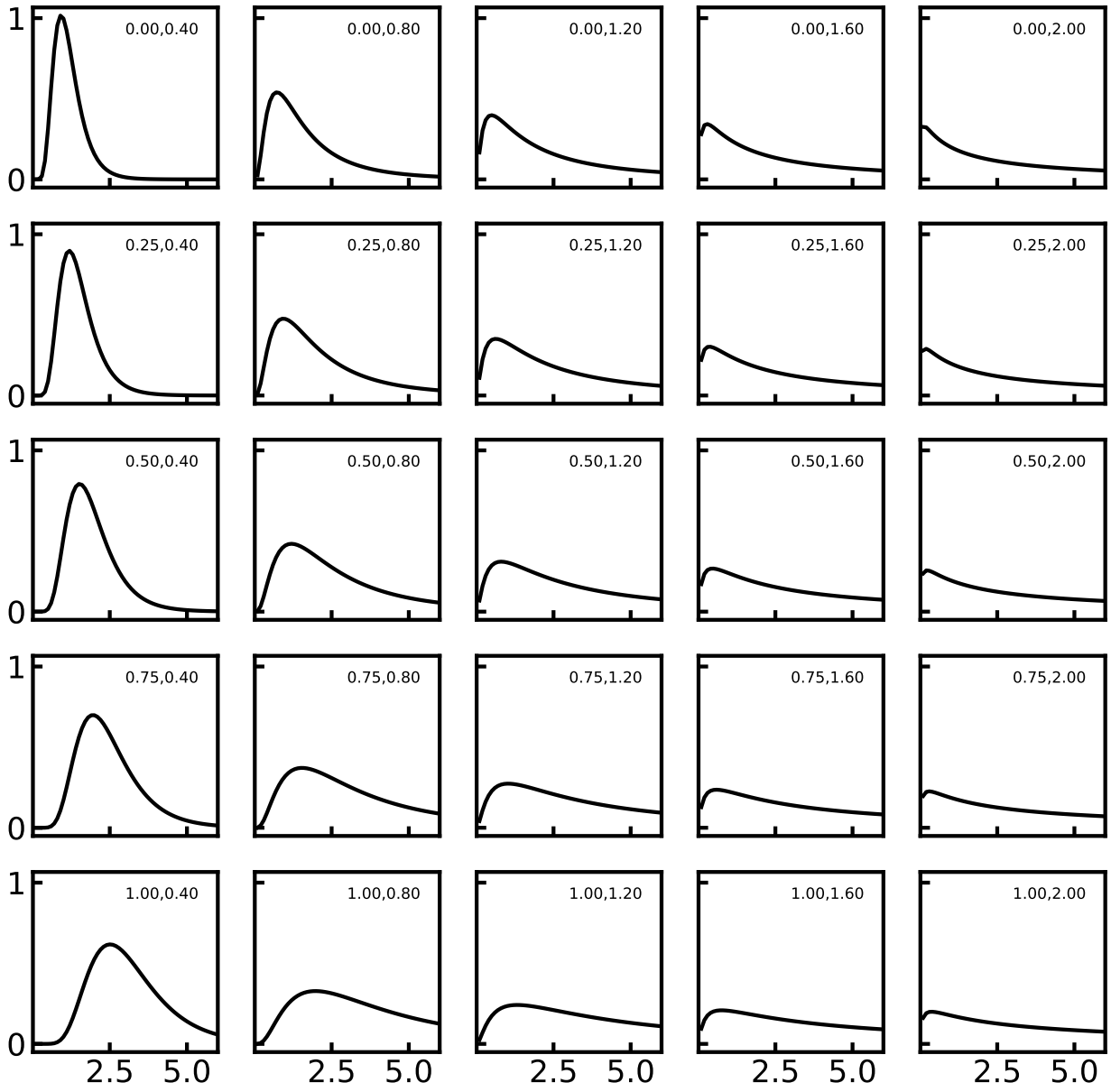

Figure 1.2: Log-normal function models of transfer functions with varying values of M and S, where the annotation in the top-right of the plots are the applied values of M and S. A combination of transfer functions may represent the true transfer function when DCE and line emission is considered.

ionizing continuum source have varying height which would in turn change the observed lags, different geometries of the accretion disk such as puffy disks, or magnetic field coupling that leads to accretion disk temperature fluctuations.

Do note that this discussion and dissertation focuses on the broad-band UV/optical side of RM. There are even more results to be discussed within the fields of X-ray and Infrared RM that were sparsely mentioned here.

1.5 Outline

This dissertation presents the research projects in AGN continuum reverberation mapping that I have completed and/or contributed to in some manner.

Chapter 2 is on the photometric python pipeline I designed to work on reverberation mapping projects, specifically for STORM 2, but has been applied to multiple AGN. The chapter will focus on the technical details of how the pipeline works starting from data acquisition to fully intercalibrated light curves. The methods described are what were applied to the light curves presented in the rest of the chapters.

Chapter 3 is on a Las Cumbres Observatory Global Network proposal project on NGC 4395 that granted us time to observe with the LCOGT network 2 meter telescope equipped with the MuSCAT imager. We successfully observed for two partial nights and measured disk continuum lags for the intermediate mass AGN. The chapter is adapted from an Astrophysical Journal Letter that was published in August of 2022 (Montano et al., 2022) and details the data reduction and analysis performed. NGC 4395 stands out as an intermediate-mass AGN in comparison to the rest of the AGN in this dissertation that are all considered supermassive. Historically NGC 4395 does have reverberation lags measured, but this work displays one of the first optical inter-band continuum lags measurements for it. The greatest

novelty of this project is displayed in the incredibly short timescale of the time lags and observing needed to accomplish such a feat.

Chapter 4 is on my work in AGN STORM 2 which focuses on the object Mrk 817 a Seyfert 1 galaxy that has been historically observed to be unobscured which changed quickly as the campaign began. For my contributions the application of chapter 2 is included which produced high quality intercalibrated light curves of seven ground-based optical filter bands $BVugriz$ for twelve telescopes. Continuing this work is a host of analysis such as lag-measurements with multiple methods, flux-flux analysis and modeling of those measurements. The STORM 2 project has over ten plus publications at the time of this writing that includes the work from the various other space and ground-based facilities such as the Hubble Space Telescope, the Swift Space Telescope, and XMM-Newton. Included in the publications outside of specific facilities are modeling and analysis papers that make use of the light curves produced from this specific chapter. This chapter is the largest focus of the dissertation and encapsulates a large amount of my work in my graduate career. At the time of the submission of this dissertation the text is in pre-submission form set to be submitted to the Astrophysical Journal as part of the series of STORM 2 publications.

Chapter 5 is on reverberation mapping projects where I provided a supporting role, in applying my photometric pipeline to assist other astronomers in completing reverberation mapping projects. This includes two AGN: Mrk 335 a Seyfert 1 galaxy with a rich X-ray history and in reverberation mapping, and PG 1302-102 a quasar that is being tested for black hole binary candidacy through reverberation mapping. Markarian 335 is now one of the very few mapped objects with wavelength coverage in the X-ray, UV and optical. The 100-day observing campaign combined multiple ground-based telescopes to create high-quality light curves in the $BVugriz$ filters and were used to measure time lags. The results of this work may be found in Kara et al. (2023) that details the observations, methods and results.

The PG 1302-102 project used a full LCO data set, where I produced light curves to ensure the fidelity of the authors own light curves in Liu et al. (2024).

Chapter 6 is on the continuation of the AGN STORM 2 monitoring campaign of Mrk 817 and preliminary results from the optical ground-based light curves. The extended campaign of Mkr 817 continued campaign through an LCO key-project and Swift space telescope observing to cover the ultraviolet. While the Swift section of the extended campaign is not yet complete at the time of this writing, I measure optical continuum lags with the optical g band filter as the reference and compare it to the original STORM 2 lags. Surprisingly the overall flux of the extended campaign was higher than the STORM 2 and the lags in the longer wavelengths are increased with the inclusion of the new data. The chapter will go over the methodology applied to the data set to produce the light curves and lag measurements while considering the future work to be done.

Chapter 7 holds the conclusions pertinent to my works in reverberation mapping and the state of the field moving forward. The projects presented in the previous chapters display the versatility of reverberation mapping and how it may be applied in the future. Future work to be done within the STORM 2 collaboration, Mrk 817 extended campaign and other prospects for reverberation mapping are discussed to close out this dissertation.

Chapter 2

Photometry in Reverberation Mapping Campaigns

2.1 Photometry

Photometry is the measurement of the amount of light coming from an object within an image captured via a CCD or other type of photon collector. Within the field of observational astronomy this is a technique widely known and practiced. There is a great availability of coding languages that have packages or headers dedicated to these methods, however differences in methods/practices still exist in how the measurement is done. Albeit the general procedure of photometry is usually the same, differences in technique can lead to differences in measurements. These differences may be caused by, but are not limited to, the use of different programming languages, background estimation methods, and aperture sizes. My introduction to creating a photometry pipeline began with AGN STORM 2 which required photometry for the ground-based imaging from the 12 separate telescopes located around the globe which will be discussed in a Chapter 4. Part of creating the pipeline was to

continually update light curves as the observing campaign progressed and other telescopes delivered data which is essential in intensive observing projects to monitor for certain features in the AGN. The process of photometry is straight forward by itself, however what creates the differences are the proceeding reductions/methods applied to create a data product such as a light curve. An image in this context is an array of values indicating how much light there is in a certain pixel. For example, astronomical images are delivered as FITS files that contain arrays the same size as the number of pixels in the CCDs (e.g. a 2-dimensional array that may be 2048x2048 elements). The data array is the image itself and attached to the same FITS file is detailed information about the observation made. Photometry with respect to FITS images is a measurement of the amount of light within a given aperture (see Figure 2.2) and the aperture has a pixel radius large enough to encompass the object of interest. The photometric measurement is a summation of the pixels in the assigned radius, accounting for partial coverage of a pixels. The next sections will detail the use of certain photometric functions available in public python packages and other functions to create a light curve data product.

2.2 Python Aperture Photometry Pipeline

Photometric reverberation mapping campaigns often include data from multiple telescopes that have different camera detectors, mirror size, and filter properties resulting in inhomogeneous data sets that require extra care to produce well inter-calibrated light curves. I created an aperture photometry pipeline designed specifically for AGN photometric monitoring campaigns for STORM 2. This pipeline was based/inspired in part on an earlier IDL-based pipeline by Pei et al. (2014) a previous graduate student of the Barth research group. My new pipeline is written in Python 3 and is primarily a wrapper for Astropy routines (Astropy Collaboration et al., 2013, 2018a, 2022) and uses the PyCALI method of

Li et al. (2014) to intercalibrate the light curves obtained from different telescopes.[1] This pipeline has previously been used for the first results of the Mrk 817 STORM 2 campaign (Kara et al., 2021), as well as campaigns on NGC 4395 (Montano et al., 2022), Mrk 335 (Kara et al., 2023), and PG 1302-102 (Liu et al., 2024). The largest contribution provided by this pipeline is for the STORM 2 publication, Chapter 4, focusing on the disk continuum reverberation mapping of the optical light curves. The program itself automates a majority of the work involved in light curve production, but requires user interaction and attention for the best performance. Outputs of the pipeline include tables recording measurements for nearly ever step along with plots and optional diagnostic plots. Below I provide a detailed description of the method.

2.2.1 Heterogeneous Data

Multiple telescopes are not required for reverberation mapping, it may be done with a single telescope and filter wheel. The next chapter is an example of that, where we observed NGC 4395 with LCO's Faulkes Telescope North site using the 2.0 m telescope located on Haleakala, Hawaii. While this is a possibility, it is highly dependent on the AGN's BH mass estimate as this will determine the time lags one would expect, so this means that for shorter time lags the observing duration would be shorter as well. Another factor to consider is how variable is the AGN at that time as strong variability features in a light curve allow for better lag measurements. With SMBH masses in the range of around 10^8 $M_\odot$ disk continuum time lags are typically on the order of days which requires a high cadence and multiple seasons of observing. To accomplish this feat on a single telescope would be difficult due to many reasons, e.g. time constraints (telescope time is shared and vied for), where the telescope is located relative to the object (seasonal/positional constraints), and how often one visits the object (cadence). To address these challenges a collective effort may be made

[1] https://github.com/jwontano/autophot

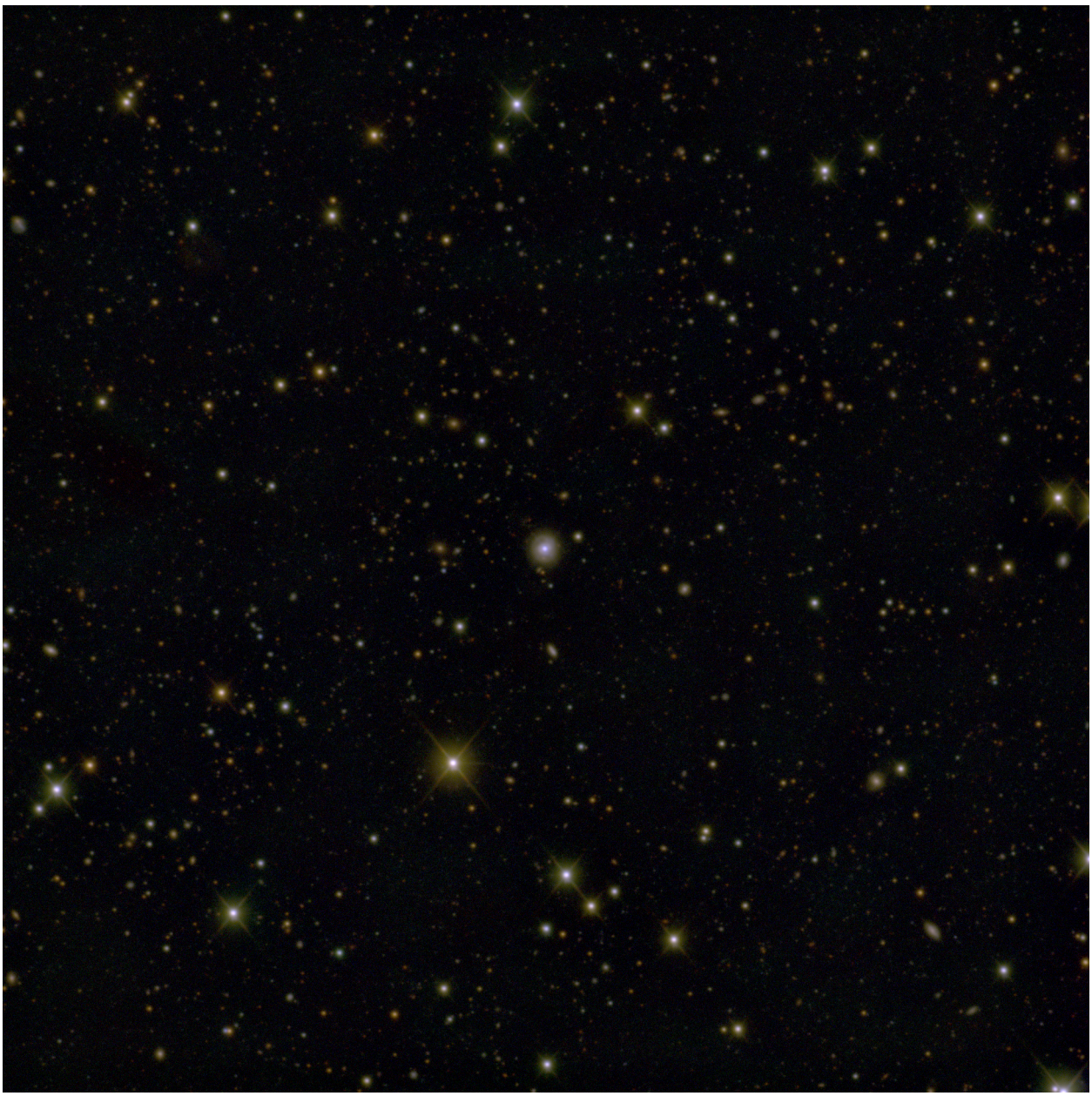

Figure 2.1: Co-added image of Mrk 817 from the STORM 2 campaign using the program Swarp, coloring performed by Aaron Barth. Mrk 817 is a spiral barred galaxy located at the center of the image.

to create an observing campaign using multiple telescopes to achieve a sub-daily (or near daily) cadence and long duration observing period. The data result of such a campaign is a large heterogeneous set of images (the amount of images generated may count from anywhere from 100's to 1000's), with separate methods of reduction (most are fairly similar though), delivery, location, cameras, lens size, noise profiles, transmission curves, etc. The 0th step, in the whole pipeline is to gather information about these attributes which, thankfully, is located within the images inside a FITS header or somewhere else easily available. The end result we strive for from all these images is to produce a data product (light curves) that is intercalibrated and fairly represent the uncertainties of the whole process.

2.2.2 Time Standards

A simple starting step is ensuring a uniform system of time is applied to all of the image headers. In RM projects the time part of the time series is typically reported as Modified Julian Date (MJD), but if we want to increase the accuracy a bit further we should be using Heliocentric Julian Date (HJD). The highest accuracy would be Barycentric JD exercised in exoplanet observing, which is not needed in RM due to the size of our lag uncertainties (perhaps in the future it may be practiced). HJD is a time standard that takes into account the location of the Earth with respect to the Sun, after all we are measuring time lags so getting rid of this time discrepancy from all images would benefit the accuracy our measurements (at most this can ± 8.3 minutes to the time stamp).

I calculate the HJD and MJD for the midpoint of each exposure using the information in each image header. Each image header I have encountered so far all have the header keyword "DATE-OBS" in UTC format. Both forms of the time are provided to the user. The date conversion is performed via the PyAstronomy package (Czesla et al., 2019).[2]

[2] `https://github.com/sczesla/PyAstronomy`

2.2.3 Comparison Stars

A time series of observations is not in the same flux scale due to a variety of reasons such as airmass differences, and weather conditions just to name a couple. If one were to take an image of a non variable source of light in the sky for the same amount of time, the measurements would not read the same every night due to the previously mentioned reasons. We use stars within the observing field of the AGN to normalize our measurements. Comparison stars are first chosen by the user visually to ensure that they are not saturated, faint, and are relatively isolated from other objects. Non-variable stars are incredibly stable compared to observing campaign timescales and we use multiple comparison stars to normalize the light curves. There is no set minimum or maximum for the amount of comparison stars, but in practice 5 to 10 similar magnitude stars (if available in the FOV) works well.

If we take the safe assumption that non-variable stars magnitude/flux won't change during our observing campaign then we can use them as a standard to calibrate the count flux (DN units) to flux-wavelength units. For the selection of comparison stars, out of testing it was found that stars with similar magnitude to the object of interest works best. The choice of brighter or dimmer stars could have unintended consequences when it comes to the later steps in the process (there may be non-linear effects). Another consideration is the types of stars chosen which may not have information readily available, at most you may have a catalog that only has recorded magnitudes. Certain stars may have different spectral profiles and therefore differing luminosities at certain wavelengths causing unintended consequences. Most of these issues may be addressed as long as the user reviews the outputs of the program, specifically that of Figure 2.4 where abberant behavior would be obvious.

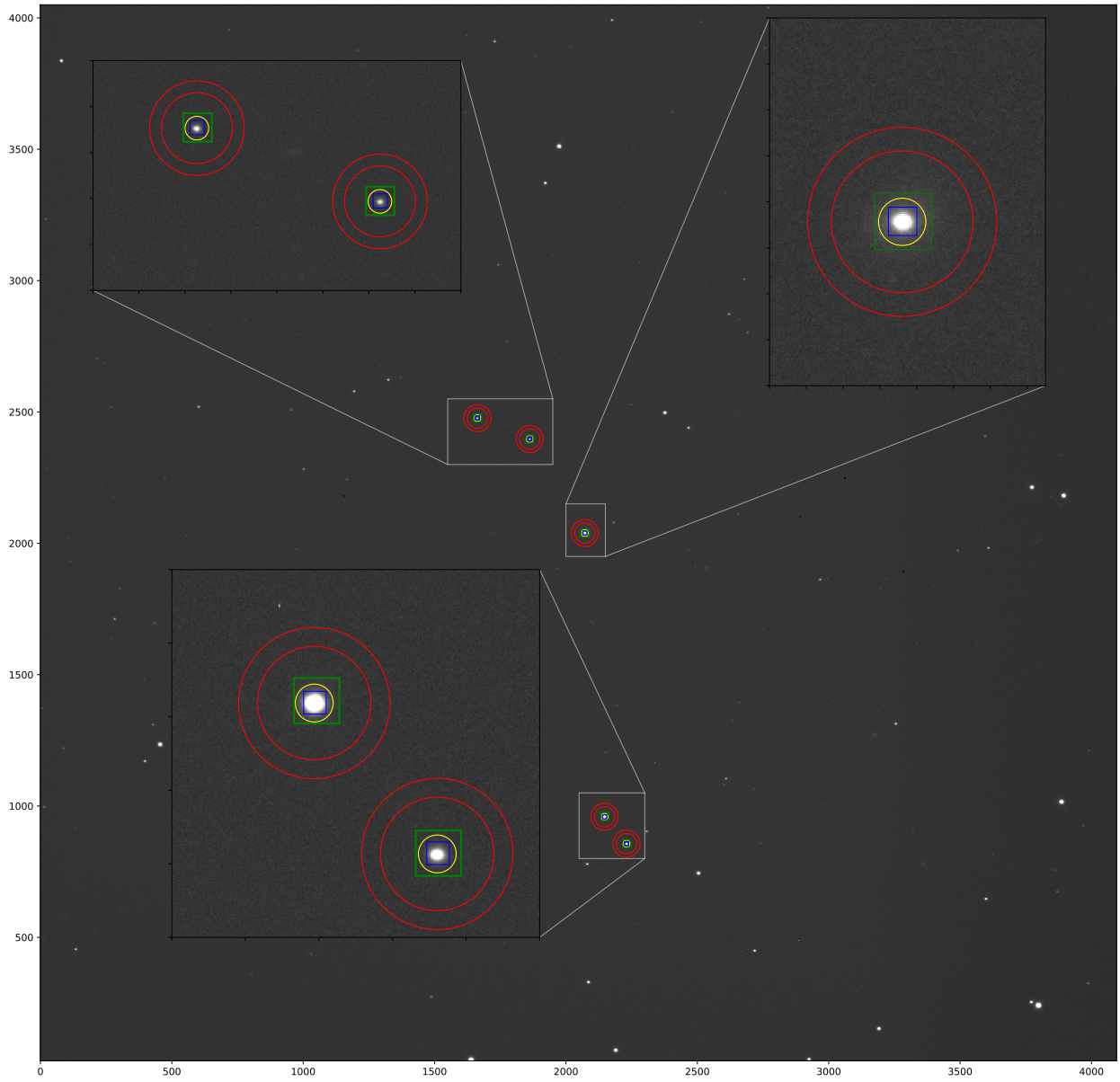

Figure 2.2: An example of a FITS image from the STORM 2 extended campaign with the centroiding process shown as different colored rings and squares. The green square is the first position to find the centroid, once that is found it is repeated with the new center which is shown as the blue square. The yellow circular 5″ aperture is placed at the 2nd centroid along with the 15″ and 10″ annulus rings shown in red. At the center of the image is the AGN and the other objects are comparison stars. This process is repeated for every image, filter and telescope in a project to produce light curves.

2.2.4 Aperture Photometry

To perform aperture photometry one needs information of where to look within the image. FITS image data is a pixel grid of photon counts, centered on the object, to position an aperture we need the pixel grid coordinates of our objects of interest. One may visually confirm these objects and their approximate grid location. The automated alternative is if they are existing cataloged objects then they have a recorded right ascension and declination (RA & DEC) which we can then use the World Coordinate System (WCS) header information to convert from (RA,DEC) to pixel coordinates (x,y).

For a given AGN field, a list of coordinates must be provided for the AGN and a set of comparison stars in the field. In each image the AGN and comparison stars are identified by coordinates using the Astropy WCS package and the code calculates their pixel coordinates via centroiding. Centroiding finds the center of mass (or peak) of a given aperture and we default to a center of mass method with optional arguments that allow for other methods such as a 2-d Gaussian. To ensure that the centroid is accurate we perform two iterations of centroiding for each object: the first iteration with a $10''$ square box then the second iteration with a $5''$ square box. The results of this process are center coordinates (in pixel coordinates) for the objects in a specific image. The size of the initial centroid box is defaulted to $10''$ but may be changed upon a users input. The secondary centroid is always half the radius of the first.

For the photometric measurements we default to a standard aperture radius of $5''$ and a $15''$–$20''$ annulus ring for background estimation across all image sets given. The aperture size in pixels is not uniform for all data sets as we convert the arcsecond radius to pixel size which is dependent on the pixel-scale of the camera used. The user is given the option to chose their own size of apertures. To estimate the sky level within the background annulus we follow a method similar to *DAOphot's* sky background estimation of $3 \times \text{median} - 2 \times \text{mean}$ (both

mean and median are sigma-clipped) if the mean is greater than the median, otherwise if the condition is not met the mean is used (Stetson, 1987). The user is given the option to use other methods such as a sigma-clipped median, where sigma-clipping is the removal of extreme outliers by criterion of being over a 5 standard deviation threshold. The sky value is then scaled by the number of pixels n in the photometric aperture and then subtracted from the aperture measurement ($background\ estimate \times aperture\ area$), where the aperture area for a circular aperture is $n\pi r^2$. The photometric uncertainty is determined by the photon statistics and read noise within the aperture. We use a standard definition of noise for astronomical images

$$\text{noise} = \sqrt{\text{expt} \times (\text{source} \times \text{gain} + \text{npix} \times (\text{sky} \times \text{gain} + \text{dark})) + \text{npix} \times \text{rdnoise}^2} \quad (2.1)$$

to determine the aperture uncertainty, expt being exposure time of the image, source is the aperture sum subtracted the scaled background estimate, gain is the conversion factor from data number (DN) to e^-, npix the number of pixels in the aperture (npix is the aperture radius squared $\times\ \pi$), sky is the sky background estimate mentioned earlier, dark is the dark noise counts, and rdnoise the read noise of the ccd. The last step here is to record these measurements made and that is done using Astropy's phot table. Phot tables are generated whenever the Photutils function *aperture_photometry*() is ran. The table itself is very similar to a pandas dataframe or other dataframe-esque objects which enables quick modification to add new headers to the table. To finish out this process we save: all the aperture measurements made (background subtracted aperture sum being the final measurement), header information such as the file name, time stamp(s), filter used, uncertainties, and other informative tags.

2.2.5 Normalization

When applying all these operations to the images we organize them according to the filters, in the optical we usually cover the $BVugriz$ filters which covers a wavelength range of approximately $3000 - 9000$ Å which for low-redshift Seyfert 1 galaxies a large amount of disk continuum light comes from. The pipeline is not limited to optical wavelengths as it should work as long as you have an image from a ground-based facility with the appropriate information.

Due to transparency variations and air mass differences the raw photometry from each night must be normalized to a consistent flux scale. For a given filter we carry out the normalization separately for each telescope and then merge the data from all of the telescopes at a later stage. The photometric measurements are normalized by determining a scale factor to apply to the flux measurements from each image. We calculate the scale factors via simultaneous fitting of all the comparison star light curves for a single telescope and filter. Using the comparison star photometry we calculate a scale factor s for each image through a χ^2 minimization, minimizing the following quantity:

$$\chi^2 = \sum_{i=1}^{K} \sum_{j=1}^{N} \frac{(s_j f_{ij} - \bar{f}_i)^2}{(s_j \sigma_{ij})^2} \tag{2.2}$$

where K is the number of comparison stars, N the number of images, s_j is the scale factor for image j, f_{ij} the count rate and σ_{ij} the uncertainty for star i in image j, and $\bar{f}_i$ is the mean count rate for star i across the time series. After determining the optimal scale factor for each image the count rate and uncertainties for the AGN and comparison star are multiplied by that scale factor. Along side the measurements are utility plots to track the progress and fidelity of the process. In Figure 2.3 and Figure 2.4 are plots generated to show the effects of normalization. The first Figure 2.4 shows the comparison stars for the AGN Mrk 817 before

and after normalization, and Figure 2.3 a plot comparing the AGN photometry before and after applying the scaling factors.

2.2.6 Flux-conversion

To convert the scaled count rates to flux units we look up comparison star magnitudes in the APASS catalog (Henden et al., 2018) or SDSS catalog. These magnitudes are then converted to units of erg s^{-1} cm^{-2} s^{-1} Å using zeropoints from Fukugita et al. (1996) and Bessell et al. (1998).

For each filter we determine a conversion factor from count rate to f_λ by determining the conversion factor for each comparison star and if any comparison star deviates greatly from the conversion factors it is removed from the average. The average conversion factor is then applied to the AGN light curve.

Multiple measurements from a given telescope taken within a window of 0.25 day are combined by weighted averaging to produce a single data point. The pipeline saves two versions of the AGN light curve, one including each individual photometric measurement and one with the nightly averaging applied. For the analysis and plots in this paper we use the nightly averaged light curves.

2.3 Intercalibration

A problem that comes with using data from multiple telescopes is that differences in wavelength-dependent throughput for different telescopes can result in slight differences in their overall flux scales after applying the above procedures (e.g., Hernández Santisteban et al., 2020). Additionally, the measurement uncertainties at this stage are only based on photon counting

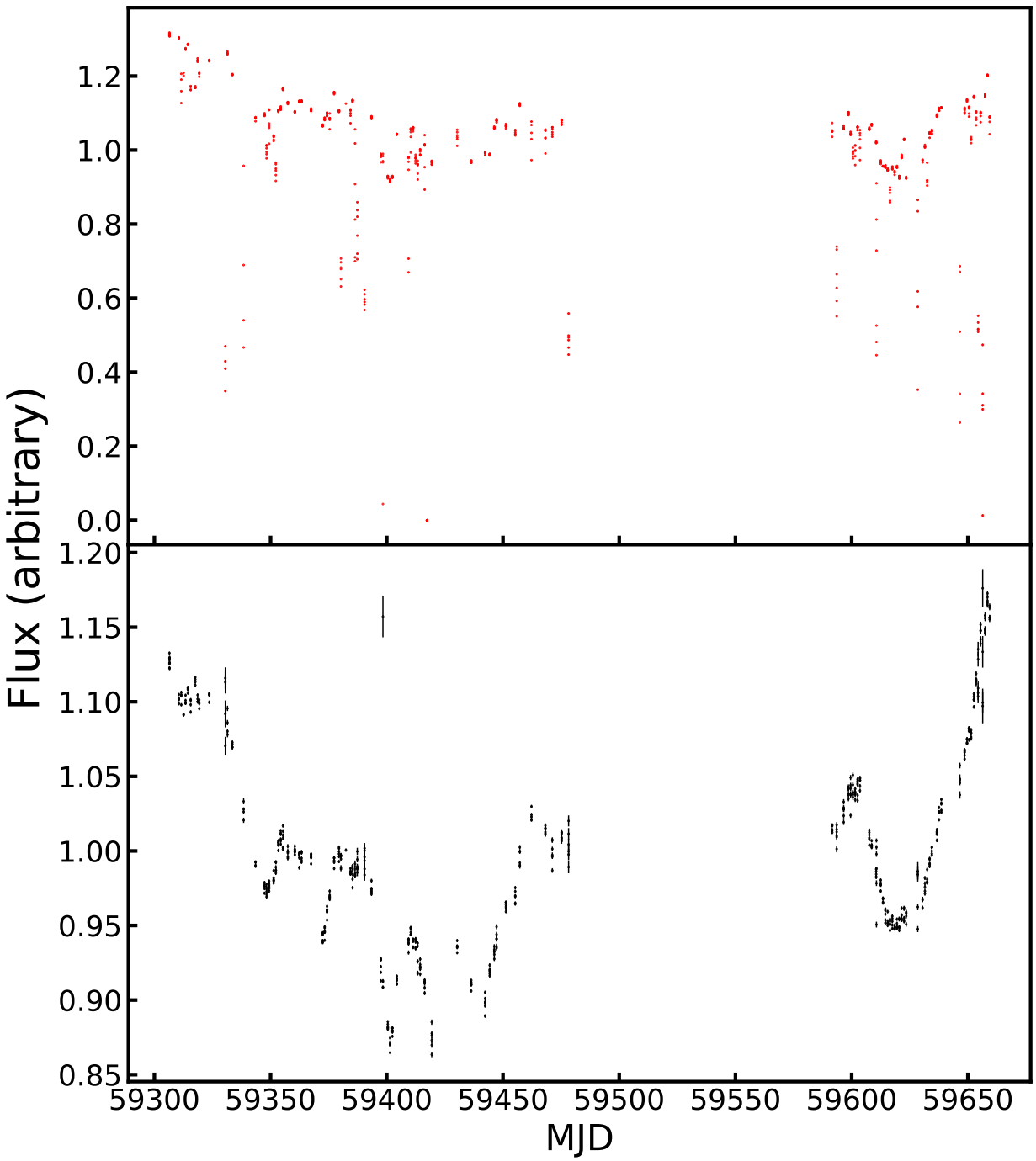

Figure 2.3: AGN light curves of Mrk 817 before and after normalization for a single telescope (specifically from the Las Cumbres Observatory 2.0 m which displays excellent SNR). Both light curves shown have been divided by their means to normalize the flux counts near 1. *Top*: The AGN light curve before normalization. Without normalization it is difficult to make out the signature variability of an AGN. The light curve also makes apparent how the different observing conditions effects our measurements. *Bottom*: The AGN light curve after normalization. The light curve has a clear defined variable structure that we expect out of AGN's, yet it still contains outliers that pass through the photometric process. Such outliers are dealt with in the intercalibration process.

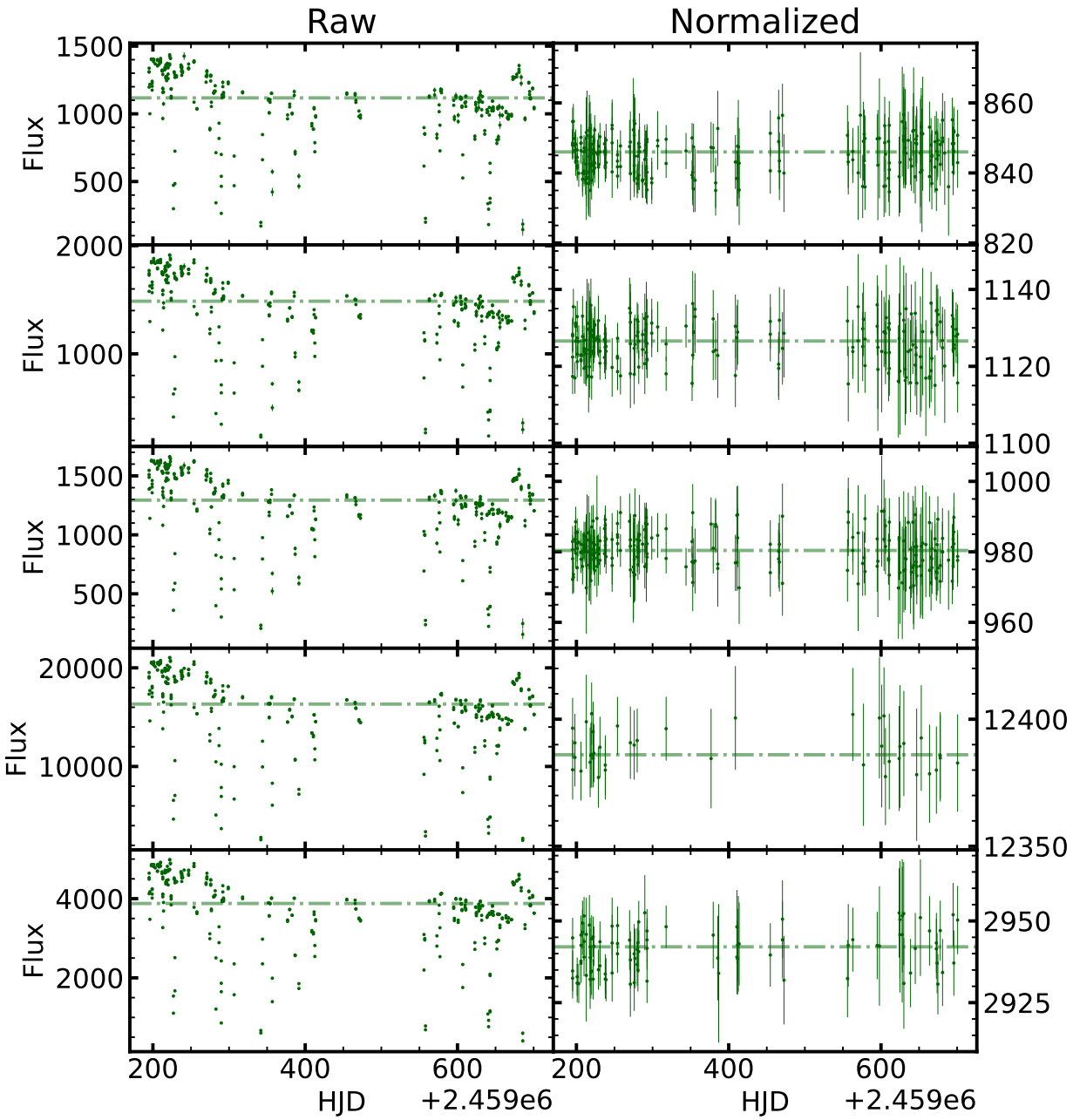

Figure 2.4: The comparison star light curves are shown for the AGN Mrk 817 for a single telescope (the measurements come from a Las Cumbres Observatory 1.0 m telescope with great signal-to-noise). For the left columns each point is a photometric measurement with errorbars before normalization scaling is applied, note that the points typically fall around similar flux values except for when they fall well below the dash-dotted line (the median value of the light curve) which indicates lower than optimal conditions that led to such reduced counts (this is usually due to weather conditions, in particular clouds). On the right column are the results of the light curves after normalization has been applied and outlier rejection for points that end up with errors too large or are 3σ from the new median.

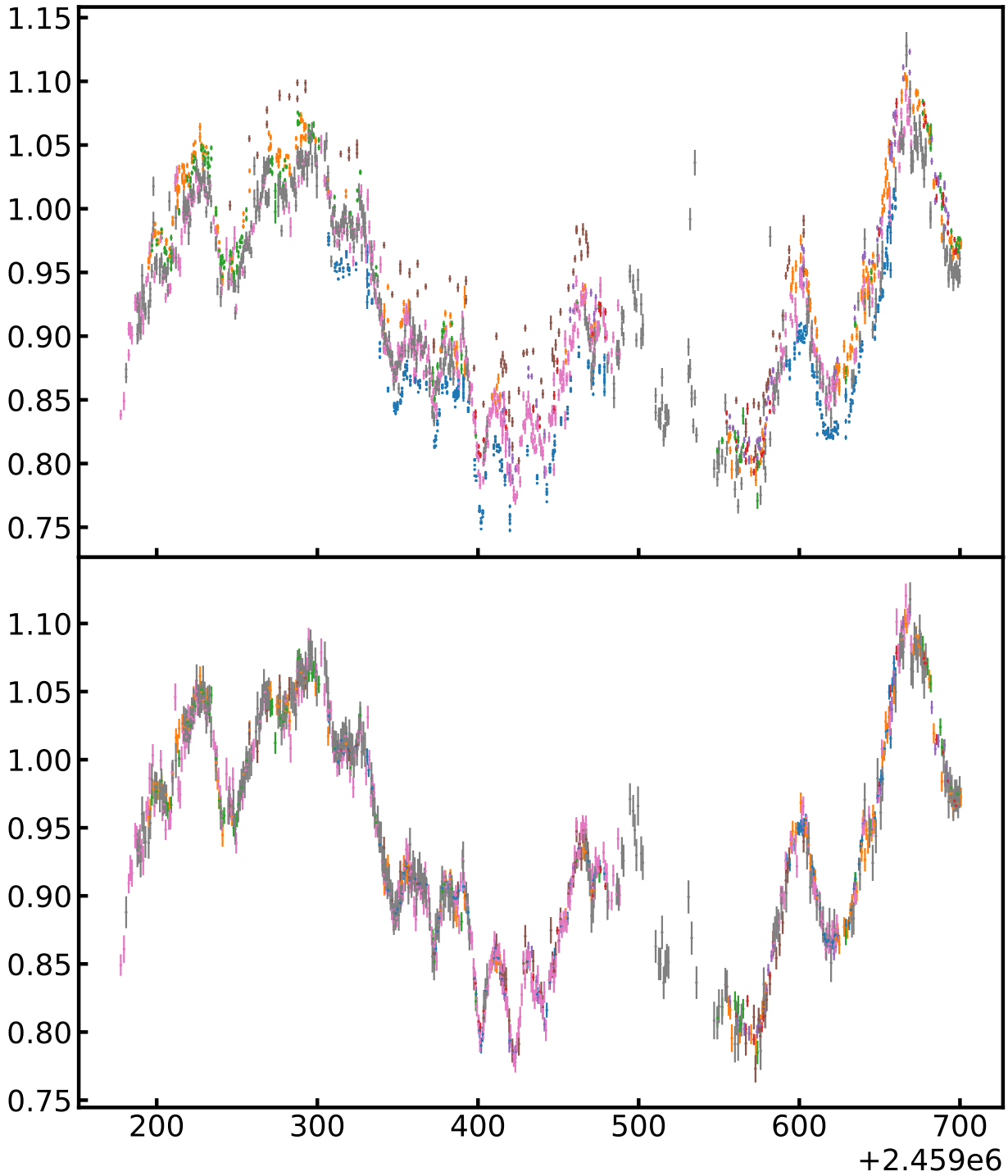

Figure 2.5: Light curve example before they are intercalibrated and after using PyCALI. The general shape of the light curve is present in the individual light curves. To intercalibrated them they need to be shifted and scaled to a reference light curve. The reference light curve is generally one with the longest duration and highest signal-to-noise.

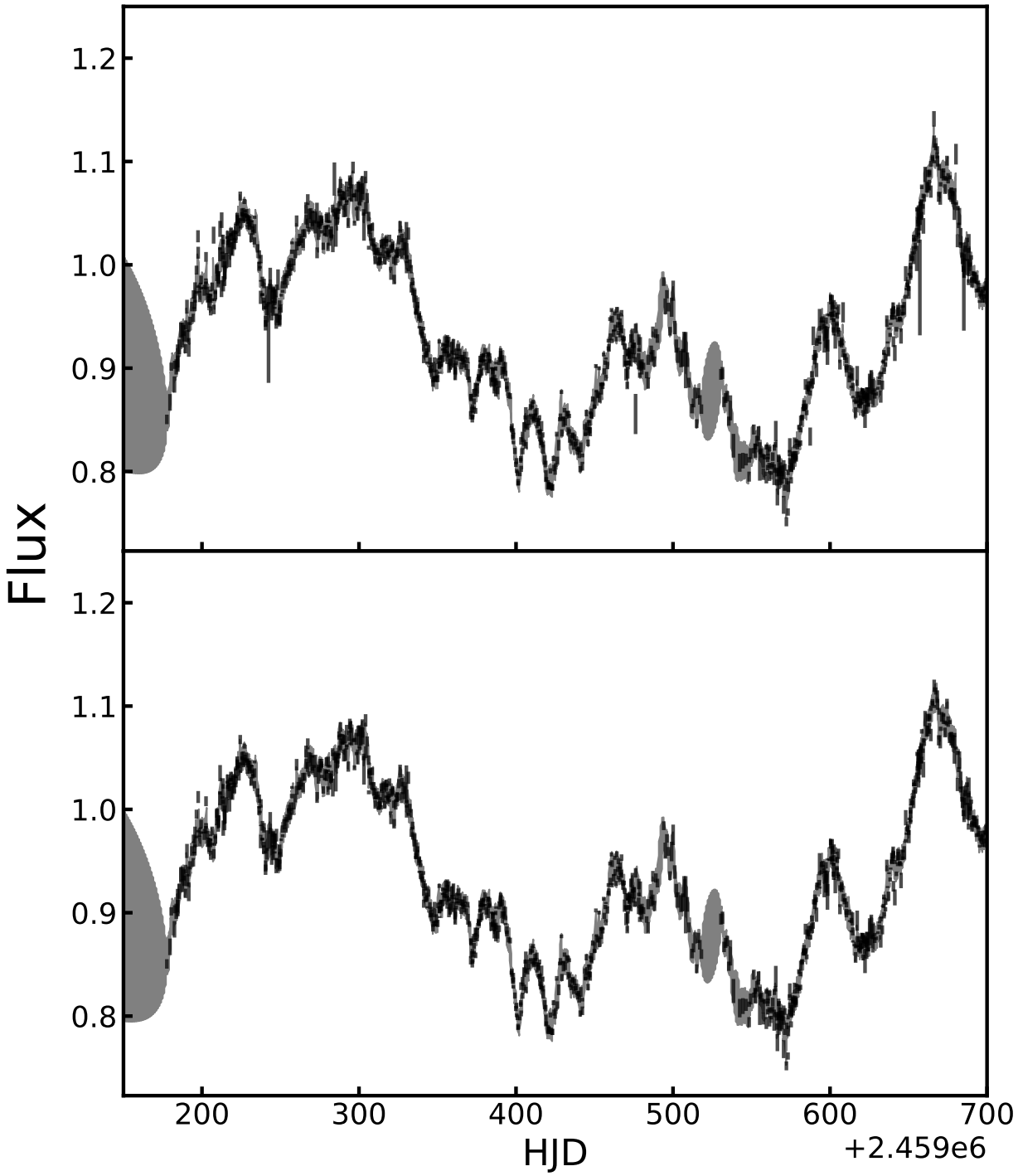

Figure 2.6: The light curves shown are intercalibrated with PyCALI and underlaid is the DRW model for the specific round. The first round of PyCALI does well intercalibrating the light curves together however the DRW model is straining to fit to each individual data point as a result of the low uncertainties. The second round of PyCALI, after uncertainty expansion and intercalibration shows a smooth DRW model that we then use to further check the intercalibration of the light curves by repeating the uncertainty expansion on individual telescopes.

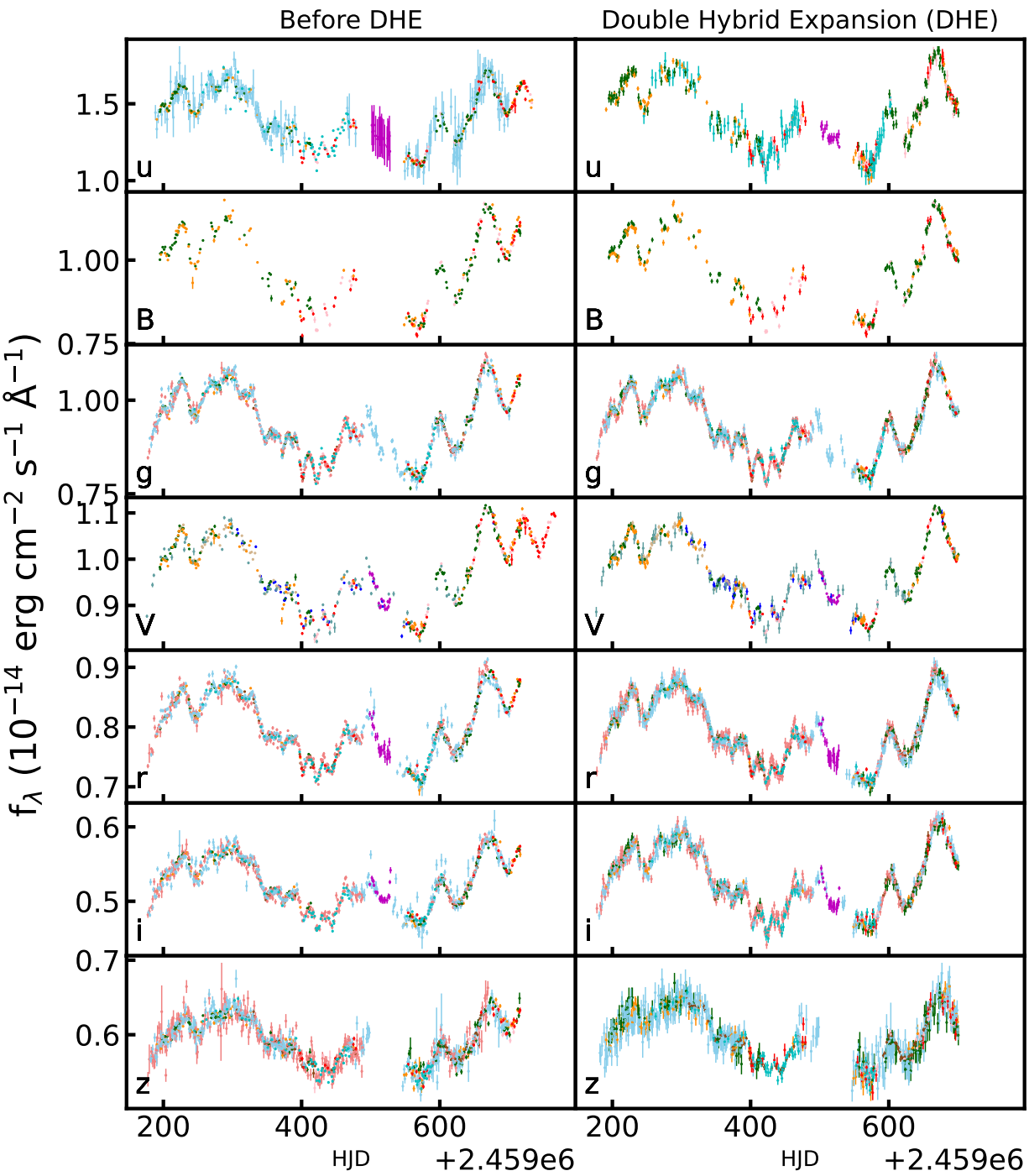

Figure 2.7: Before and after comparison of uncertainty expansion. The left-column are the default setting of uncertainty adjustment within PyCALI. The uncertainties are expanded to create a better fit to the damped random walk model, generated by PyCALI, via χ^2 minimization. There are several changes from the left column to the right aside form uncertainty changes: there is the exclusion of certain light curves due to high scatter and uncertainties in the u and z bands, more outliers are rejected, high quality light curves are preserved while low quality ones have their uncertainties appropiately expanded.

statistics and do not account for other systematic errors such as seeing variations or flat fielding errors. We then apply an intercalibration procedure to bring the flux scales, for a single filter, from different telescopes into agreement and adjust the error bars to account for additional systematics.

For intercalibration we use PyCALI, a code that applies an additive shift and a multiplicative scale factor to scale each telescope's light curve to a common flux scale (Li et al., 2014). The result of running this intercalibration program is shown in Figure 2.5 where each color represent a different telescopes light curve. Before they are close in flux value and afterwards are intercalibrated to the same flux scale which allows for more statistically sound lag measurements. PyCALI here takes advantage of the fact that AGN variability may be modeled as a damped random walk (DRW) (Zu et al., 2013; MacLeod et al., 2010).

PyCALI implements a damped random walk (DRW) to model the AGN's variability along with a Markov Chain Monte Carlo (MCMC) process to find the best parameters and uncertainties. We implement two modifications compared with the typical application of PyCALI. The first is that we apply PyCALI to the data twice in order to obtain a better DRW model fit. We found that due to the small statistical errors on the photometric data points the DRW model fit from the first PyCALI run exhibited too much high-frequency structure as the model strained to fit the individual data points. After the first PyCALI run we then expanded the errors on the data points following the procedure described below and ran PyCALI again on the intercalibrated light curves. The second PyCALI run then produced a smoother DRW model fit that provided a better intercalibration of the light curves. Figure 2.6 shows the before and after of this procedure with the top being the first PyCALI run and the bottom panel the second. The first run still has outliers, which are removed in the next run, and the gray outline DRW model strains at certain points where creating unrealistic structure, e.g. in the first quarter of the light curve there is a downward spike in the model

and in the tail end of the light curve. The ballooned sections of the DRW model are where no data points exist so the model creates high uncertainties between the adjacent points.

The second modification to the standard PyCALI procedures was to expand the errors on the data points through an additional error term added in quadrature. The additional error term is determined by finding the value that yields the best-fit to $\chi^2_{\rm dof} = 1$ with respect to the DRW model. We interpolate the DRW model to the light curve to measure the $\chi^2_{\rm dof}$ value. This additional error term is determined individually for each telescope. After the first PyCALI run and error expansion we reject data points that were $> 3\sigma$ outliers with respect to the DRW model fit. After the second PyCALI run the errors were adjusted one last time with the same procedure to obtain $\chi^2_{\rm dof} = 1$ to correct if the procedure under or over-fitted.

The final results are intercalibrated, uncertainty-expanded light curves as shown in Figure 2.7. Figure 2.7 shows the effects of the error expansion by comparing the light curve before this procedure was implemented. One can see that the uncertainties of telescopes that already were high are the most changed in comparison to telescopes that boast high signal-to-noise points. For those telescopes their defined structure does not become washed out due to the uncertainty expansion. Following this chapter all light curves shown in the optical filters are produced by this photometry pipeline. For some chapters the resulting light curves may be slightly different as they were created before certain major changes, e.g. the uncertainty expansion. The code itself is available for free use if wanted at `https://github.com/jwontano/autophot`.

Chapter 3

Optical Continuum Reverberation Mapping in the Dwarf Seyfert Nucleus of NGC 4395

3.1 Abstract

In order to constrain the size of the optical continuum emission region in the dwarf Seyfert 1 galaxy NGC 4395 through reverberation mapping, we carried out high-cadence photometric monitoring in the *griz* filter bands on two consecutive nights in 2022 April using the four-channel MuSCAT3 camera on the Faulkes Telescope North at Haleakalā Observatory. Correlated variability across the *griz* bands is clearly detected, and the r, i, and z band light curves show lags of $7.72^{+1.01}_{-1.09}$, $14.16^{+1.22}_{-1.25}$, and $20.78^{+1.99}_{-2.09}$ minutes with respect to the g band when measured using the full-duration light curves. When lags are measured for each night separately, the Night 2 data exhibit lower cross-correlation amplitudes and shorter lags than the Night 1 light curves. Using the full-duration lags, we find that the lag-wavelength

relationship is consistent with the $\tau \propto \lambda^{4/3}$ dependence found for more luminous AGN. Combining our results with continuum lags measured for other objects, the lag between g and z band scales with optical continuum luminosity as $\tau_{\rm gz} \propto L^{0.56\pm0.05}$, similar to the scaling of broad-line region size with luminosity, reinforcing recent evidence that diffuse continuum emission from the broad-line region may contribute substantially to optical continuum variability and reverberation lags.[1]

3.2 Introduction

The active galactic nucleus (AGN) in the dwarf spiral galaxy NGC 4395 is the nearest and best-studied example of an AGN containing a very low-mass black hole (BH). First identified from the broad wings on its Hα emission line (Filippenko & Sargent, 1989), it exhibits all of the characteristics of an accretion-powered Seyfert 1 nucleus, including a high-excitation photoionized narrow-line region (Kraemer et al., 1999), highly variable X-ray emission (Lira et al., 1999; Moran et al., 2005), and a compact radio core (Wrobel et al., 2001), but its bolometric luminosity is just $\sim 5\times10^{40}$ erg s^{-1} (Moran et al., 2005), and the broad component of its Hα emission line has a dispersion of only $\sigma \approx 600$ km s^{-1} (Cho et al., 2021). The mass of the BH in NGC 4395 is not precisely determined, but a variety of methods (including indirect estimates, reverberation mapping, and dynamical studies) point to a mass in the range $\sim 10^4$ to a few $\times10^5$ $M_\odot$ (Kraemer et al., 1999; Shih et al., 2003; Filippenko & Ho, 2003; Peterson et al., 2005; den Brok et al., 2015; Woo et al., 2019; Cho et al., 2020). While a growing number of AGN in this BH mass range have been detected in recent years (for a review, see Greene et al., 2020), NGC 4395 remains uniquely amenable to detailed study due to its proximity at $d \approx 4$ Mpc (Thim et al., 2004).

[1]This work is adapted from the Astrophyscial Journal Letter publication Montano et al. (2022) (Web-link)

The small physical size of the AGN in NGC 4395 results in much shorter timescales for variability and reverberation at ultraviolet (UV) and optical wavelengths than are typical of luminous AGN. By fitting the TESS light curve of NGC 4395 with a damped random walk (DRW) model, Burke et al. (2020) found the DRW damping timescale to be $\tau_{\rm DRW} = 2.3^{+1.8}_{-0.7}$ days, in contrast to luminous AGN having $\tau_{\rm DRW}$ in the range of hundreds to thousands of days. Its broad emission-line reverberation lags are just $\sim$1 hour, both for the C IV λ1549 line measured relative to the 1350 Å continuum (Peterson et al., 2005) and for the Hα line measured relative to the V-band continuum (Woo et al., 2019; Cho et al., 2020).

Continuum reverberation mapping can provide a direct probe of the size of the UV/optical continuum emitting region in AGN, if the UV/optical continuum variations result from reprocessing of coronal emission by the accretion disk and/or gas in the broad-line region (for a recent review see Cackett et al., 2021). While the continuum lags between UV and optical wavelengths in luminous Seyferts are typically a few days (e.g., Edelson et al., 2019), the continuum reverberation timescales in NGC 4395 are found to be much shorter. Using Hubble Space Telescope STIS UV observations from Peterson et al. (2005) combined with ground-based photometry, Desroches et al. (2006) measured a lag of 24^{+7}_{-9} minutes between the 1350 Å continuum and the optical V band. McHardy et al. (2016) presented a preliminary report of an XMM-Newton and ground-based campaign on NGC 4395. Using data from the XMM-Newton Optical Monitor with the UVW1 filter ($\lambda_{\rm cen}$ = 2600 Å) and ground-based g-band photometry, they detected time delays of 473^{+47}_{-98} and 788^{+44}_{-54} s for the UVW1 and g bands relative to the X-rays, which indicates that the lag of the g-band relative to the UVW1 band is $\sim$315 s.

Although time delays between UV and optical continuum bands in NGC 4395 have been measured, inter-band optical continuum lags have not been detected in prior work, largely due to the challenge of resolving very short timescales in observations that cycle between different filters on a single telescope (e.g., Edri et al., 2012). Extrapolating the 315 s time

delay between 2600 Å and the g band (McHardy et al., 2016) under the assumption of the $\tau \propto \lambda^{4/3}$ scaling relationship expected for reprocessing by a standard thin accretion disk (Cackett et al., 2007), the predicted lag between the g and z bands is just $\sim$11 minutes. The nightly V-band variability amplitude of the AGN is typically $\sim 0.05 - 0.1$ mag (e.g., Cho et al., 2020, 2021), and an inter-band lag of several minutes is potentially detectable if photometry can be obtained with sufficiently high cadence and signal-to-noise ratio. Measurement of broad-band optical reverberation lags in NGC 4395 would provide new constraints on the size of its optical continuum emission region and a significant extension to the luminosity range of AGN having such constraints. In this work, we report on the first unambiguous detection of continuum reverberation across the optical wavelength range in NGC 4395.

3.3 Observations

We observed NGC 4395 on 2022 April 26 and 27 (UT) using the MuSCAT3 camera (Narita et al., 2020) on the 2 m Faulkes North Telescope (FTN) located at Haleakalā Observatory. FTN is a part of the Las Cumbres Observatory (LCO) Global Telescope Network (Brown et al., 2013a). MuSCAT3 is a four-channel imager that observes simultaneously in g', r', i', and z_s filter bands (abbreviated as $griz$ hereinafter), with a $9\farcm1 \times 9\farcm1$ field of view and $0\farcs27$ pixels. We used the fast readout mode (readout time 6 s) in order to obtain a rapid observing cadence, given the expectation that the inter-band lags might be as short as a few minutes. Exposure times were set to 100 s in the g, i, and z bands. Since no suitable guide stars are available for use by the telescope autoguider in the field surrounding NGC 4395, we used the "guide off" mode, in which guiding is done using short exposures on one of the MuSCAT3 cameras. We chose the r band for guiding, and used 25 s exposures in r. On April 26 UT (Night 1), repeated observations in all four bands were carried out for a total duration of 6.7 hours, and on April 27 (Night 2) the observations spanned 6.2 hours.

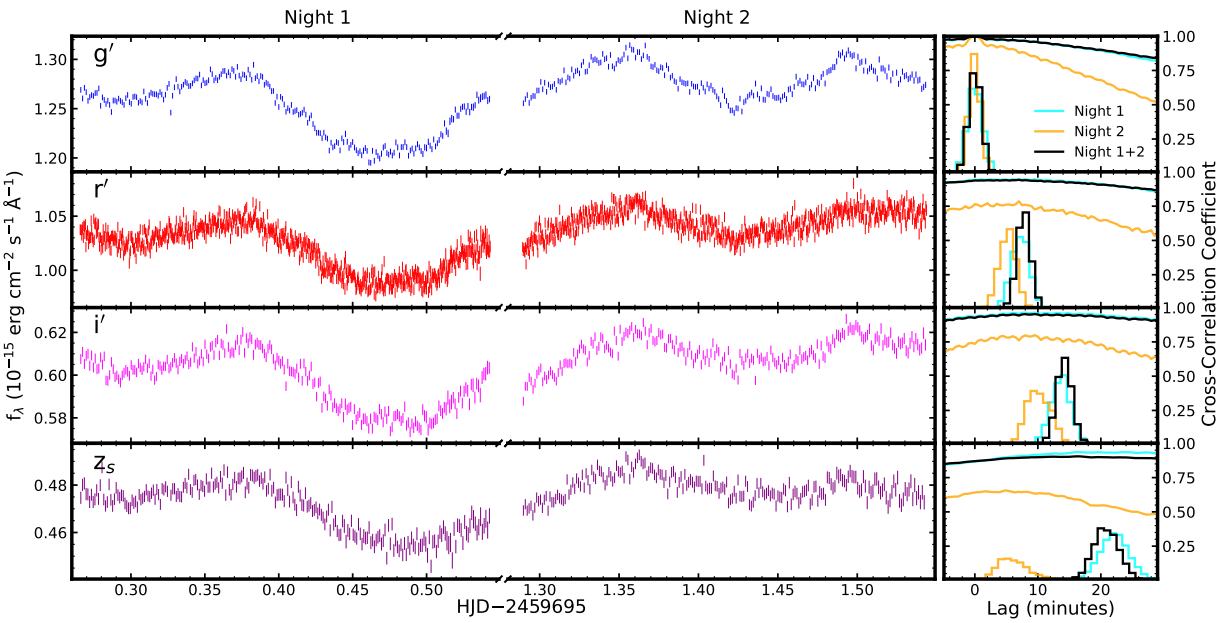

Figure 3.1: NGC 4395 light curves and cross-correlation lags. *Left:* MuSCAT3 light curves in the *griz* bands. *Right:* Cross-correlation results for each band, measured relative to the g band. Each panel shows cross-correlation functions (curves across the upper portion of the panel) and cross-correlation centroid distributions (histograms, renormalized to arbitrary units) for the data from Night 1 and from Night 2 separately, and for the combined Night 1 + Night 2 light curves. The g-band panel displays the autocorrelation functions and autocorrelation centroid distributions of the g-band light curves.

Conditions were mostly clear on both nights, and the median seeing for all observations was $0\farcs91$ with standard deviation $0\farcs14$.

3.4 Data Reduction and Photometry

The images were processed by the LCO BANZAI reduction pipeline, which includes bad pixel masking, bias subtraction, flat-field correction, and astrometric calibration using astrometry.net (Lang et al., 2010).

Photometry was carried out using an automated procedure based on Astropy (Astropy Collaboration et al., 2018b) routines for aperture photometry and background sky measurement. In each image, the AGN and a set of comparison stars were identified by their coordinates.

Aperture photometry was carried out using a photometric aperture radius of $3''$, with the sky annulus spanning $10 - 20''$. We found that the best results were obtained using a single comparison star, SDSS J122550.91+333310.1, located close to the central region of NGC 4395. Counts were converted into flux density units using *griz* photometric data obtained from the Sloan Digital Sky Survey (SDSS) for the comparison star. SDSS uses a z' filter while MuSCAT3 uses z_s, so the z-band calibration is only approximate, but the overall normalization of the light curves does not affect the reverberation measurements.

The final light curves are displayed in Figure 3.1 and the photometric data are listed in Table 3.4. Multiple features are present in the light curves, providing the required structure for cross-correlation lag measurement. The variations at longer wavelengths appear smoother and with lower amplitude than those in the g band, as expected for a more extended reprocessing region at longer wavelengths, combined with the increasing contribution of light from the surrounding nuclear cluster (Carson et al., 2015).

Filter Band	HJD−2459695	f_λ	$\sigma(f_\lambda)$
g	0.2661	1.269	0.003
g	0.2673	1.260	0.003
g	0.2685	1.271	0.003
g	0.2697	1.267	0.003
g	0.2709	1.258	0.003
g	0.2722	1.262	0.003
g	0.2734	1.264	0.003
g	0.2746	1.263	0.003
g	0.2758	1.266	0.003
g	0.2770	1.266	0.003
g	0.2783	1.271	0.003
g	0.2795	1.253	0.003
g	0.2807	1.261	0.003
g	0.2819	1.259	0.003
g	0.2831	1.255	0.003
g	0.2844	1.258	0.003
g	0.2856	1.254	0.003
g	0.2868	1.247	0.003
g	0.2880	1.258	0.003
g	0.2892	1.258	0.003
g	0.2904	1.257	0.003
g	0.2917	1.260	0.003

Table 3.1: The listed HJD values give the midpoint time of each exposure. This table has been published in its entirety in machine-readable format.

Band	Night 1		Night 2		Nights 1&2	
	$\tau_{\rm cen}$ (min)	$r_{\rm max}$	$\tau_{\rm cen}$ (min)	$r_{\rm max}$	$\tau_{\rm cen}$ (min)	$r_{\rm max}$
g (4770 Å)	$0.00^{+1.22}_{-1.25}$	1.00	$0.00^{+0.78}_{-0.79}$	1.00	$0.03^{+0.97}_{-0.97}$	1.00
r (6215 Å)	$7.23^{+1.43}_{-1.41}$	0.95	$5.21^{+1.33}_{-1.24}$	0.79	$7.72^{+1.01}_{-1.09}$	0.94
i (7545 Å)	$13.64^{+1.66}_{-1.58}$	0.95	$10.15^{+1.81}_{-2.00}$	0.80	$14.16^{+1.22}_{-1.25}$	0.95
z (8700 Å)	$22.15^{+2.28}_{-2.30}$	0.94	$5.93^{+2.17}_{-2.81}$	0.66	$20.78^{+1.94}_{-2.09}$	0.91

Table 3.2: Lags are given in the observed frame in units of minutes. Central wavelengths are listed for each filter. All lags are measured relative to the g band.

3.5 Lag Measurement

We measured the time lags of the *riz* bands relative to the g band using the interpolated cross-correlation function (ICCF) method (Gaskell & Peterson, 1987b), with the code PyCCF (Sun et al., 2018a). CCFs were measured over a lag search range spanning -72 to 72 minutes, with a sampling interval of 0.5 minutes. The measurements were performed on the Night 1 and Night 2 data separately, and also on the combined Night 1 and 2 light curves. Error analysis was carried out using the standard flux randomization/random subset selection (FR/RSS) method (Peterson et al., 1998b), with 10000 resampling iterations. In each iteration, the centroid of the CCF is determined from points above $0.8r_{\rm max}$, where $r_{\rm max}$ is the peak height of the CCF. We take the lag for each band to be the median of the cross-correlation centroid distribution (CCCD) from the 5000 FR/RSS iterations. The lags and $r_{\rm max}$ values are listed in Table 3.2.

Although the CCFs have very broad peaks, their centroids are well determined, with uncertainties of $\sim 1-2$ minutes on the $\tau_{\rm cen}$ measurements. The Night 1 light curves yield very high $r_{\rm max}$ values of 0.94–0.95, while the Night 2 data show substantially lower levels of inter-band correlation with $r_{\rm max}$ values of 0.66–0.80. This can be attributed in part to a lower fractional variability amplitude during Night 2, but intrinsic changes in the continuum emission region structure may be partly responsible as well. The Night 2 lags are systematically shorter than those of Night 1, and the differences increase with wavelength. In particular, the z-band lags exhibit a striking change, from 22.2 minutes on Night 1 to just 5.9 minutes on Night 2, and the difference between these is significant at the 5.1σ level considering the uncertainties on both measurements. The lags measured from the combined Night 1 + Night 2 light curves are very similar to the Night 1 lags, with $r_{\rm max}$ values nearly as high, indicating that the overall cross-correlation strength is dominated by the stronger variability in the Night 1 data. We take the combined Night 1 + 2 results as the final lag results for the following discussion.

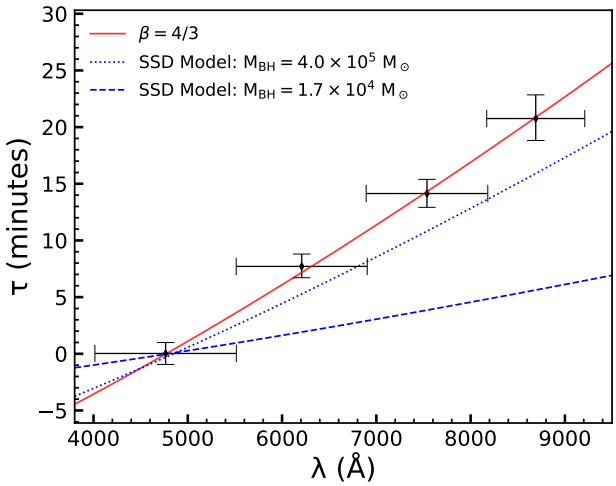

Figure 3.2: Lags as a function of wavelength in the rest frame of NGC 4395, from the combined Night 1 + Night 2 data. Horizontal error bars denote the width of each filter. The $\beta = 4/3$ power-law fit to the *riz* data points is shown as a red curve. Blue dashed and dotted curves represent SSD lag-wavelength models calculated for BH masses of 1.7×10^4 and 4×10^5 $M_\odot$, respectively.

3.6 Discussion

Figure 3.2 displays the inter-band lags corrected to the AGN rest frame (using $cz = 319$ km s^{-1}) as a function of rest-frame wavelength. To compare the data with disk reprocessing model predictions, we fit the *riz* data points with the function $\tau(\lambda) = \tau_0 \left[(\lambda/\lambda_0)^\beta - 1\right]$, where λ_0 is the central wavelength of the *g*-band filter shifted to the AGN rest frame ($\lambda_0 = 4765$ Å), τ_0 is a free parameter (e.g., Edelson et al., 2019), and we fix $\beta = 4/3$ corresponding to a standard thin accretion disk. By construction, the model has $\tau = 0$ at $\lambda = \lambda_0$, so we do not include the *g*-band data point in the fit. This simple model provides a good fit to the data, as shown in Figure 3.2, with $\chi^2_\nu = 0.17$ for two degrees of freedom. The low χ^2_ν value may result from the tendency of the FR/RSS method to overestimate lag uncertainties (Yu et al., 2019).

We compare the observed lag-wavelength trend with model predictions for thermal reprocessing by a Shakura & Sunyaev (1973a) disk (SSD) model following the method described by Fausnaugh et al. (2016) and Edelson et al. (2017). In this model, the radius corresponding

to peak emission at wavelength λ is given by

$$r(\lambda) = \left(X\frac{k\lambda}{hc}\right)^{4/3}\left[\left(\frac{GM_{\rm BH}}{8\pi\sigma}\right)\left(\frac{L_{\rm E}}{\eta c^2}\right)(3+\kappa)\dot{m}\right]^{1/3}, \tag{3.1}$$

where G is the gravitational constant, $M_{\rm BH}$ is the black hole mass, σ is the Stefan-Boltzmann constant, $L_{\rm E}$ is the Eddington luminosity, $\dot{m}$ is the Eddington ratio, η (set to 0.1) is the radiative efficiency, and κ (set to 1) represents the relative contribution between X-rays and viscosity in disk heating. The quantity X (set to 3.36) is a factor used in converting disk temperature to wavelength for a responsivity-weighted emitting radius (Tie & Kochanek, 2018). To calculate $\dot{m}$ we adopt the bolometric luminosity measurement of 5.3×10^{40} erg s^{-1} from Moran et al. (2005). Since the BH mass of NGC 4395 is highly uncertain, we calculate models for two values spanning the range of recent measurements: $M_{\rm BH} = 1.7 \times 10^4\ M_\odot$ from Hα reverberation mapping (Cho et al., 2021) and $4 \times 10^5\ M_\odot$ from spatially resolved gas dynamics (den Brok et al., 2015). In Figure 3.2 we show curves of the predicted lags relative to the g band, $\tau(\lambda) = [r(\lambda) - r(\lambda_0)]/c$, for these two $M_{\rm BH}$ values.

Intensive UV/optical continuum reverberation mapping programs have found continuum emission region sizes that are typically $\sim 2-3$ times larger than expected from disk reprocessing models (Cackett et al., 2021). While one possibility is that AGN accretion disks are larger than model predictions, recent work has focused on the contribution of diffuse continuum emission from the broad-line region (BLR) as an explanation for the longer-than-expected continuum lags and their wavelength dependence (e.g., Cackett et al., 2018; Korista & Goad, 2019; Chelouche et al., 2019; Netzer, 2022). For NGC 4395 we find that the observed continuum emission region is 3.6 or 1.2 times larger than the disk reprocessing model predictions for BH masses of 1.7×10^4 or $4\times10^5\ M_\odot$, respectively. These discrepancies would be $\sim 50\%$ greater if $X = 2.49$ was used; this value corresponds to a flux-weighted (rather than responsivity-weighted) emission radius and has been used in several other recent continuum reverberation studies (e.g., Edelson et al., 2019). These model calculations for our

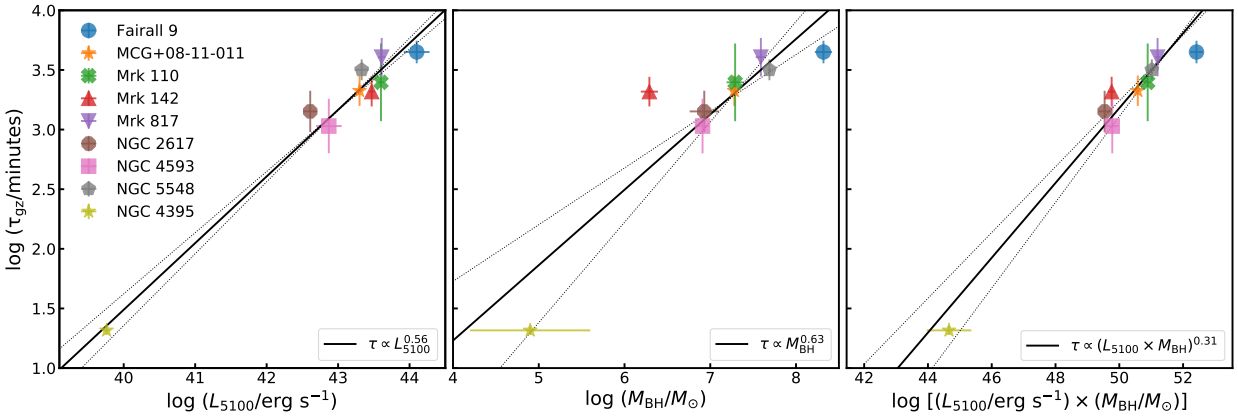

Figure 3.3: Rest-frame inter-band lag τ_{gz} as a function of AGN continuum luminosity at 5100 Å (*left*), BH mass (*middle*), and the product $L \times M_{BH}$ (*right*). The $g-z$ lags of eight local AGN are from literature sources as described in the text. The AGN continuum luminosities and black hole masses for the comparison sample are from Bentz & Katz (2015). The quantity L_{5100} refers to λL_λ at 5100 Å. For NGC 4395, the horizontal error bar on M_{BH} denotes the range spanning 1.7×10^4 to 4×10^5 $M_\odot$ corresponding to the mass measurements from Cho et al. (2021) and den Brok et al. (2015). The black solid and dotted lines in each panel denote the power-law model fit and its 1σ uncertainty range.

chosen fiducial values of M_{BH} imply that NGC 4395 may have a "disk size problem" similar to that found in more luminous Seyferts, and if M_{BH} is at the lower end of the published range then NGC 4395 would be consistent with the trend identified by Li et al. (2021) in which lower-luminosity AGN exhibit larger disk size discrepancies. However, the standard disk reprocessing scenario could still be compatible with the data considering the BH mass uncertainty range of $M_{BH} = 4^{+8}_{-3} \times 10^5$ $M_\odot$ (3σ uncertainties) found by den Brok et al. (2015). Alternatively, these results could be interpreted as favoring a BH mass at the upper end of the likely range, if the basic disk reprocessing model was assumed to apply.

To compare the NGC 4395 continuum lags with these of more massive AGN, we selected eight local AGN (redshifts $0.017 < z < 0.047$) having high-quality g through z-band data from intensive disk reverberation mapping campaigns: Fairall 9 (Hernández Santisteban et al., 2020), MCG+08−11−011 (Fausnaugh et al., 2018), Mrk 110 (Vincentelli et al., 2021), Mrk 142 (Cackett et al., 2020a), Mrk 817 (Kara et al., 2021), NGC 2617 (Fausnaugh et al., 2018), NGC 4593 (Cackett et al., 2018), and NGC 5548 (Fausnaugh et al., 2016). In these

papers, the g and z-band lags were measured relative to some other UV or optical band used as the driving light curve, but lags between g and z were not directly measured. In order to compare the measured $\tau_{\rm gz}$ of NGC 4395 with other AGN, we downloaded the light curve data from the original publications where available, and measured $\tau_{\rm gz}$ with the ICCF method as described previously.[2] We performed a 2nd-order polynomial detrending for Fairall 9 before lag measurement to remove the long-term variability trend, following Hernández Santisteban et al. (2020). For NGC 2617 and MCG+08−11−011 we used the best light-curve segments for lag measurement, following Fausnaugh et al. (2018). For Mrk 110 and Mrk 817, the light curve data are not available in the published works, and we derived an estimate of $\tau_{\rm gz}$ by taking the difference between the published z-band and g-band lags, using error propagation to estimate the uncertainty on $\tau_{\rm gz}$.

The adopted observed-frame $\tau_{\rm gz}$ lags are $3.25^{+0.79}_{-0.78}$ (Fairall 9), $1.5^{+0.51}_{-0.51}$ (MCG+08−11−011), $1.79^{+2.02}_{-1.07}$ (Mrk 110), $1.51^{+0.50}_{-0.49}$ (Mrk 142), $2.90^{+1.30}_{-1.34}$ (Mrk 817), $1.00^{+0.49}_{-0.49}$ (NGC 2617), $0.75^{+0.52}_{-0.46}$ (NGC 4593), and $2.24^{+0.50}_{-0.50}$ (NGC 5548) days. AGN continuum luminosities at 5100 Å and black hole masses for the comparison sample are available from the Bentz & Katz (2015) catalog. For NGC 4395, we adopt the host-corrected AGN continuum luminosity of $\lambda L_\lambda = (5.75 \pm 0.4) \times 10^{39}$ erg s^{-1} at 5100 Å from Cho et al. (2020). As before, we consider a BH mass range from 1.7×10^4 to 4×10^5 $M_\odot$ corresponding to recent measurements. We use the geometric mean of these values as the fiducial black hole mass with the uncertainty range spanning the range of these two values [$\log(M_{\rm BH}/M_\odot) = (4.9 \pm 0.7)$] in the following analysis.

Figure 3.3 displays the relationship of $\tau_{\rm gz}$ with AGN continuum luminosity at 5100 Å, and with $M_{\rm BH}$. The 20.4 minute lag in NGC 4395 extends the dynamic range of the comparison sample downward by a factor of ∼50, and $\tau_{\rm gz}$ is clearly correlated with both luminosity and

[2]For NGC 4593, the continuum light curves from Cackett et al. (2018) were measured from Hubble Space Telescope STIS spectroscopic data, and we used the published light curves at λ = 4745 and 8800 Å to approximate the g and z bands.

mass. The lag $\tau_{\rm gz}$ has a tighter relationship with L than with $M_{\rm BH}$, which could indicate that luminosity is a more fundamental driver of the continuum emission size, but larger uncertainties in the BH masses (particularly for NGC 4395) might also be responsible for the larger scatter in the $\tau_{\rm gz}$-$M_{\rm BH}$ relation. We performed linear fits to the relations between $\log(\tau_{\rm gz}/{\rm min})$ and $\log(L_{5100}/{\rm erg\ s^{-1}})$ and between $\log(\tau_{\rm gz}/{\rm min})$ and $\log(M_{\rm BH}/M_{\odot})$ with the code linmix (Kelly, 2007), which employs a hierarchical Bayesian model incorporating errors in both the luminosity and lag measurements.

For the $\tau_{\rm gz} - L$ relation we find $\log(\tau_{\rm gz}/{\rm min}) = \left(0.56^{+0.05}_{-0.04}\right)\log(L_{5100}/{\rm erg\ s^{-1}}) - \left(20.87^{+1.88}_{-1.96}\right)$, with a slope similar to the $r \propto L^{0.5}$ scaling of the BLR radius-luminosity relationship (Bentz et al., 2013; Dalla Bontà et al., 2020). This result is very similar to the recent finding by Netzer (2022) that the V-band continuum lags of luminous Seyferts (measured relative to the UV) follow a $\tau \propto L_{5100}^{0.5}$ trend. As argued by Netzer (2022), this observed lag-luminosity scaling suggests that diffuse continuum emission from the BLR (e.g, Korista & Goad, 2019) makes a substantial or even dominant contribution to the optical variability amplitude and continuum reverberation lags. The addition of NGC 4395 to the sample significantly extends the range of the $\tau - L$ relationship and demonstrates that the trend found by Netzer (2022) continues to apply at the lowest AGN luminosities. This provides further corroborating evidence for the scenario in which BLR continuum emission contributes significantly to optical variability, as also demonstrated by the presence of a distinct excess lag at wavelengths below the Balmer jump in several objects (e.g., Fausnaugh et al., 2018; Cackett et al., 2018; Edelson et al., 2019).

For the $\tau_{\rm gz} - M_{\rm BH}$ relationship we obtain $\log(\tau_{\rm gz}/{\rm min}) = \left(0.63^{+0.16}_{-0.21}\right)\log(M_{\rm BH}/M_{\odot}) - \left(1.30^{+1.53}_{-1.14}\right)$; the slope of this relationship is not as tightly constrained due to the large uncertainty in the NGC 4395 BH mass.

The disk model of Equation 3.1 predicts a scaling of $\tau \propto (L \times M_{\rm BH})^{1/3}$ at fixed λ. In the right panel of Figure 3.3 we plot the relation between $\tau_{\rm gz}$ and the product $(L_{5100} \times M_{\rm BH})$ along

with a power-law fit to the data with slope as a free parameter, again using $\log(M_{\rm BH}/M_\odot) = (4.9 \pm 0.7)$ to span the expected range in $M_{\rm BH}$. The best fit gives $\tau_{\rm gz} \propto (L \times M_{\rm BH})^{0.31\pm0.05}$, nearly identical to the disk reprocessing model prediction. However, this scaling can also be compatible with a scenario in which BLR diffuse continuum emission makes a large contribution to the optical variability, and where lag is primarily dependent on luminosity. Fitting a power law to the mass-luminosity relation of our sample yields $L_{5100} \propto M_{\rm BH}^{1.14}$. Combining the observed $\tau_{\rm gz} \propto L_{5100}^{0.56}$ relation with the mass-luminosity relation of the sample implies that the sample should follow $\tau_{\rm gz} \propto (L_{5100} \times M_{\rm BH})^{0.30}$, consistent with the observed $\tau_{\rm gz} \propto (L \times M_{\rm BH})^{0.31\pm0.05}$ scaling. In this way, a continuum lag-luminosity relation dominated by BLR reprocessing can produce a scaling of τ with $(L_{5100} \times M_{\rm BH})$ very similar to the disk reprocessing prediction. As a result, the τ vs. $(L \times M_{\rm BH})$ relation does not clearly discriminate between the disk and the BLR as the dominant location for continuum reprocessing in the optical spectrum, but observations of a larger sample spanning a broad range in Eddington ratio could potentially yield a useful test and possibly discriminate between disk reprocessing and other models for optical variability (e.g., Sun et al., 2020).

The difference in the measured lags between Night 1 and Night 2 indicates that the reprocessing geometry may undergo changes on very short timescales. The Night 2 data strongly depart from the expected lag-wavelength trend in that the z-band lag is shorter than the i-band lag, although the dominant reverberation behavior apparent in the combined Night 1+2 data follows the $\tau \propto \lambda^{4/3}$ model closely. Very few AGN have high-cadence continuum reverberation mapping data spanning timescales long enough to search for temporal changes in lags (one example is Mrk 110 which has shown evidence for a time-varying BLR contribution; Vincentelli et al., 2022). In light of this unusual behavior, it would be particularly useful to carry out monitoring of NGC 4395 over a longer time baseline, and over a broader range of wavelengths (ideally including X-ray and UV observations) to better explore temporal changes in lag behavior, and test whether variations in lag are correlated with any other observable properties. The dynamical timescale in the optically emitting region of the

accretion disk in NGC 4395 will be of order days, compared with years for luminous Seyferts, making it possible to conduct studies of disk variability in NGC 4395 during a single observing season that would require years to decades to span the corresponding timescales in more typical AGN.

3.7 Conclusions

We have measured optical continuum reverberation lags in the dwarf AGN NGC 4395, finding lags of just $\sim 8 - 20$ minutes for the *riz* bands relative to the g band. The trend of lag vs. wavelength is well matched by a $\tau \propto \lambda^{4/3}$ model, but the large uncertainty in BH mass precludes strong conclusions as to whether NGC 4395 has a "disk size problem" similar to that of high-luminosity AGN. The addition of NGC 4395 extends the continuum lag-luminosity scaling found by Netzer (2022) by two orders of magnitude in luminosity, and the derived slope of $\tau \propto L^{0.56}$ over this extended luminosity range further reinforces suggestions that diffuse BLR continuum emission contributes substantially to AGN optical continuum lags. Future continuum reverberation mapping of NGC 4395 over a broader wavelength range would be particularly valuable in order to search for evidence of diffuse continuum emission from the BLR, and to better understand short-timescale variations in reprocessing behavior.

Chapter 4

AGN STORM 2. XII. Ground-Based Optical Photometry and Lag Measurements of Mrk 817

4.1 Abstract

We present the ground-based imaging campaign and light curves of Markarian 817 as part of the multiwavelength monitoring program AGN STORM 2. Observations were carried out for approximately 420 days in BV and *ugriz* optical filters using 12 telescopes, with a median cadence of 0.4 days in the g band. Reverberation lags are measured using three methods (ICCF, JAVELIN, and PyROA) with the Swift UVW2 band used as the reference light curve. The ICCF lags range from 3.0 ± 0.8 days for the u band up to 7.9 ± 1.5 days for z, and are consistent with a $\tau \propto \lambda^{4/3}$ dependence, the relation expected for lamp-post reprocessing by a Shakura-Sunyaev disk. The lags exceed thin disk reprocessing predictions by factors of $2.7 - 4.9$, similar to the "disk size discrepancy" seen in other Seyfert galaxies. We divide

the campaign into three epochs with different levels of luminosity and obscuration ($\bar{N}_H$) and find that lags vary by as much as a factor of 2 between epochs. From the results of a flux-flux analysis, we show that the spectral energy distribution (SED) of Mrk 817 is bluer and brighter in the first third of the campaign, and find that the longest reverberation lags are obtained during this epoch. These results suggest that changes in the ionizing luminosity can produce large variations in continuum lag on short timescales by altering the diffuse continuum luminosity emitted by the broad-line region and/or the obscuring outflow.

4.2 Introduction

Although supermassive black holes account for only $\sim$0.1% of the bulge mass of their host galaxies, they are understood to play an outsize role in galaxy evolution through feedback effects that occur during episodes of accretion (Kormendy & Ho, 2013; Heckman & Best, 2014). Understanding the physical processes involved in gaseous accretion onto black holes in active galactic nuclei (AGN) and the launching of winds and outflows is essential in order to model their impact on the properties and distribution of gas in the host galaxy environment and on star formation rates. Due to the small sizes of AGN accretion flows, the most widely applicable method for studying their structure is reverberation mapping, which relies on temporal rather than angular resolution (Cackett et al., 2021). This method uses long-duration monitoring observations of AGN to resolve time delays between light curves of continuum radiation generated close to the black hole and reprocessed line or continuum emission originating from more distant locations in the accretion disk, the broad-line region (BLR), or the obscuring torus. Reverberation mapping of broad emission lines has been essential for determination of BLR sizes, measuring black hole masses in AGN, and setting the foundation for methods used to estimate black hole masses in high-redshift quasars to

trace the early growth of supermassive black holes (e.g., Wandel et al., 1999; Peterson et al., 2004; Onken et al., 2004; Vestergaard & Peterson, 2006).

Over the past decade, ultraviolet (UV) and optical continuum reverberation mapping has become widely employed as an important probe of accretion disk structure and reprocessing physics, primarily thanks to large allocations of time for AGN monitoring programs with the Neil Gehrels Swift Observatory and with ground-based robotic telescopes including those of Las Cumbres Observatory. Early conceptions of the origin of optical continuum reverberation lags in AGN (e.g., Collier et al., 1999; Sergeev et al., 2005; Cackett et al., 2007) were based on a model in which X-ray photons originating close to the black hole are absorbed by the accretion disk surface, and the absorbed energy is re-radiated with a thermal spectrum corresponding to the local disk temperature. The light-travel time between the central source and the disk reprocessing regions then gives rise to the observed reverberation time delays (τ), expected to show a $\tau(\lambda) \propto \lambda^{4/3}$ delay spectrum for a Shakura & Sunyaev (1973b) disk having a temperature profile $T(R) \propto R^{-3/4}$. This model motivated efforts to use optical continuum reverberation mapping to measure accretion disk radii and even to use disk lags to define a distance indicator as a way to determine the Hubble constant (Collier et al., 1999).

However, data from intensive multiwavelength continuum reverberation mapping campaigns have demonstrated clear inconsistencies with the basic lamp-post reprocessing model. In the six-month AGN STORM campaign on NGC 5548 carried out in 2014, observations from the Hubble Space Telescope (HST), Swift, and ground-based facilities revealed a UV/optical lag spectrum consistent with the predicted $\tau(\lambda) \propto \lambda^{4/3}$ dependence, but with a normalization approximately three times larger than expected for disk reprocessing given the assumed BH mass and accretion rate (Edelson et al., 2015; Fausnaugh et al., 2016). A similar "disk size discrepancy" has subsequently been seen in several other objects that have been monitored by Swift and ground-based telescopes (e.g., Edelson et al., 2019; Kara et al., 2023; Prince

et al., 2025) as well as for quasars monitored through long-duration survey programs (e.g., Jiang et al., 2017; Jha et al., 2022; Guo et al., 2022; Homayouni et al., 2022), implying that either accretion disks are typically a few times larger than predicted by standard models, or that processes other than thin-disk reprocessing are responsible for the lags.

Another fundamental challenge for the simple lamp-post reprocessing model stems from the fact that some monitoring programs have shown little or no correlation between short-timescale variations in X-ray and UV light curves (e.g., Edelson et al., 2019; Morales et al., 2019). This argues against reprocessing of coronal X-ray emission as the primary driver of short-timescale UV/optical flux variations in AGN.

These issues have motivated the development of a variety of models to explain the origin of optical variability and the longer-than-expected continuum lags, including models based on modifications to disk shape or reprocessing geometry (Gardner & Done, 2017; Starkey et al., 2022), changes to disk temperature profile due to winds (Sun et al., 2019), accounting for relativistic effects and allowing for a greater coronal height above the disk and boosting disk temperatures by a factor of order 2 to shift responses to shorter wavelengths (Kammoun et al., 2021), or considering the variability due to disk temperature fluctuations rather than reprocessing of coronal X-rays (e.g., Cai et al., 2018; Sun et al., 2020). To explain the weak correlations various studies have: modified existing models as in Panagiotou et al. (2022) where use of a dynamic corona in simulations helps explain the poor correlation, apply X-ray reprocessing to an inhomogeneous disk to show that turbulence in the disk may be responsible for the poor correlation (Ren et al., 2024), or through radiation magnetohydrodynamic (MHD) simulations which results in the same correlation (Secunda et al., 2024).

Work by Korista & Goad (2001), Lawther et al. (2018), and Korista & Goad (2019) highlighted the important contribution of nebular "diffuse continuum" (DC) emission to the UV/optical spectrum and to the continuum reverberation lags. The DC spectrum is composed of free-free and bound-free emission from photoionized gas in the BLR, and the larger

size of the BLR compared with the accretion disk implies that the DC emission will show lags longer than those originating from the disk itself. Key evidence for the DC contribution to the continuum lags comes from detection of an enhanced or excess lag in the U band. This feature was first seen in the AGN STORM campaign data for NGC 5548 (Edelson et al., 2015; Fausnaugh et al., 2016) and subsequently detected in Swift and ground-based monitoring data for several other AGN (Edelson et al., 2019; Hernández Santisteban et al., 2020; Cackett et al., 2020a; Vincentelli et al., 2022; Kara et al., 2023). HST STIS reverberation mapping data of NGC 4593 have provided the most detailed, spectrally resolved view of the enhanced lag in the U-band region (Cackett et al., 2018). This excess is attributed to the strong bump in the DC emission spectrum shortward of the Balmer jump, and photoionization models computed for NGC 5548 predict that DC emission can account for $\sim 20 - 40\%$ of the total continuum flux across the optical spectrum, with the largest contributions falling just shortward of the Balmer jump and the Paschen jump (Korista & Goad, 2019). The presence of DC emission offers a natural explanation for observed continuum lags being greater than expected from disk reprocessing alone, and recent studies have suggested that DC emission is sufficient to fully account for the observed lags (e.g., Chelouche et al., 2019; Netzer, 2022).

The AGN STORM 2 campaign targeted Mrk 817 for intensive multiwavelength monitoring over a 15-month span from late 2020 through early 2022. Like the earlier STORM campaign on NGC 5548 (De Rosa et al., 2015b), the STORM 2 campaign was centered on a large HST program (Program ID GO-16196) of high-cadence UV spectroscopic observations. The campaign also included daily observations with Swift, ground-based optical photometry and spectroscopy, and additional X-ray observations with XMM-Newton, NICER, and NuSTAR. The overall program design and science goals, along with early results from the first three months of observations, are described in Paper I (Kara et al., 2021). Although Mrk 817 was selected as the target for the STORM 2 program based on its historical lack of strong UV absorption lines, suggesting a clean line of sight to the central engine, the HST and X-ray

observations during the initial portion of the campaign revealed blueshifted UV absorption lines and a highly absorbed X-ray spectrum due to the emergence of an ionized outflow.

Reverberation mapping of the broad emission lines and UV/optical continuum were central goals of the STORM 2 program. Paper II (Homayouni et al., 2023) presented lag measurements for UV emission lines (Lyα, N Roman5, Si Roman4+O Roman4, C Roman4, and He Roman2). Paper V (Homayouni et al., 2024) carried out more detailed measurements for C Roman4, showing that both the responsivity and the lag of the C Roman4 line showed dramatic changes during different portions of the campaign, which were attributed to variations in the obscuration of the ionizing flux incident on the BLR. Paper IV (Cackett et al., 2023) presented continuum reverberation mapping results from the Swift component of the STORM 2 campaign. Key results included (1) a lack of correlation between the X-ray and UV light curves, (2) a lag spectrum consistent with the typical $\tau \propto \lambda^{4/3}$ dependence, and (3) detection of a temporary divergence between the far-UV and near-UV light curve shapes for a brief period early in the campaign, which coincided with an increase in the absorbing column density as seen in X-ray observations (Paper III; Partington et al., 2023). An investigation of frequency-resolved continuum lags was presented in Paper VII (Lewin et al., 2024). Paper VII found that changes in lag during the campaign appear to be correlated with changes in the X-ray obscuring column density $N_{\rm H}$, and proposed that the episodic launching of obscuring outflows could temporarily shield the BLR from the ionizing continuum, decreasing the DC luminosity and reducing the overall continuum lags. Paper X (Netzer et al., 2024) carried out photoionization modeling for BLR clouds, demonstrating that DC emission from the disk wind and from the BLR provides a good match to the lag spectrum across UV and optical wavelengths, implying that the accretion disk itself accounts for only a small portion of the observed lags.

In this paper, we present results from the ground-based imaging component of the STORM 2 campaign, which employed 12 telescopes to monitor Mrk 817 at high cadence in seven filter

Observatory	Location	Diameter (m)	# of Visits
LCOGT			
McDonald	Texas, USA	1.0	129, 81 (g)
Teide	La Palma, Spain	1.0	31, 52 (g)
Haleakala	Hawaii, USA	2.0	117 (g)
Wise	Negev, Israel	0.46	285 (g)
Liverpool (LT)	Canary Islands, Spain	2.0	70 (g)
Zowada	New Mexico, USA	0.51	254 (g)
West Mountain (WMO)	Utah, USA	0.91	43 (V)
Calar Alto (CAHA)	Andalucia, Spain	2.2	89 (V)
Yunnan - Lijiang Station	Yunnan Province, China	2.4	49 (V)
Asiago	Asiago, Italy	0.91	21 (V)

Table 4.1: The number of visits listed for each telescope denotes the number of nights in which observations were obtained in the specified filter band, after removal of bad epochs and outlier points from the light curves. Visit numbers are listed for the g band for telescopes that observed in g, or otherwise for the V band.

bands for continuum reverberation mapping. The optical light curves described in this work have previously been incorporated into other components of the STORM 2 data analysis, including an investigation of accretion disk fluctuations in Paper VI (Neustadt et al., 2024), the measurement of frequency-resolved continuum lags in Paper VII, and the comparison with BLR photoionization modeling in Paper X.

The paper is organized as follows. Section 4.3 details the data acquisition and facilities used, Section 4.4 explains the photometric measurements and intercalibration of the light curves, Section 4.5 describes the reverberation lag measurements, and Section 4.6.1 presents a flux-flux analysis and an application of the "bowl" disk reprocessing model. Discussion of the results and conclusions are presented in Sections 4.7 and 4.8. Following Paper I we adopt a redshift of $z = 0.031455$ from Strauss & Huchra (1988) for Mrk 817, and a black hole mass of of $M_{\rm BH} = 3.85 \times 10^7 M_\odot$ (Bentz & Katz, 2015) and Eddington ratio of $L/L_{\rm Edd} \sim 0.2$.

4.3 Data

4.3.1 Ground-based Observations

The ground-based campaign used multiple observatory facilities as listed in Table 4.1. Table 4.2 summarizes the camera properties of each telescope. In total 12 telescopes were used for the ground-based campaign of which five are part of the Las Cumbres Observatory network. Additional details for each observatory are given below. The STORM 2 ground-based campaign began in 2020 November and ended in 2022 April. The space-based campaign concluded earlier, in 2022 February, and the ground-based campaign was extended for a longer duration to monitor the optical response to UV variations occurring near the end of the Swift campaign. Intensive space and ground-based monitoring of Mrk 817 continued for two additional years after the conclusion of the STORM 2 campaign as part of an extended monitoring campaign that will be presented in future work.

The filters used for imaging included Johnson/Bessell B and V, Sloan Digital Sky Survey (SDSS) $u'g'r'i'z'$, and Pan-STARRS z_s. The SDSS z' and Pan-STARRS z_s lightcurves were combined since we found no significant difference in the light curve shape or lag. For brevity the SDSS and Pan-STARRS bands will be referred to as *ugriz* except when distinguishing between z' and z_s. Table 4.2 lists the specific filters used by each telescope.

Observations with the *Las Cumbres Observatory Global Telescope* network (LCOGT; Brown et al., 2013b) were obtained through the AGN key project "Intensive Disk Reverberation Mapping of Nearby Active Galactic Nuclei" (program LCO-2020B-003). Three of LCOGT's northern sites were used, including McDonald Observatory in Texas (two 1.0 m telescopes, V37 and V39), Teide Observatory in the Canary Islands (two 1.0 m telescopes, Z24 and Z31) and Haleakala Observatory in Maui (the 2.0 m Faulkes Telescope North; FTN F65). The McDonald site observed throughout the entire campaign. The Teide site began in

2021 July and continued through the remainder of the campaign, while the FTN 2.0 m observed from 2021 April until the end of the campaign. The FTN employed the Multicolor Simultaneous Camera for studying Atmospheres of Transiting exoplanets (MuSCAT3) multi-channel imager (Narita et al., 2020), which provided higher S/N images in the *griz* bands than other telescopes involved in the campaign. All images were delivered via the LCOGT archive system[1] where they are processed through the BANZAI pipeline which performs bad-pixel masking, bias subtraction, dark subtraction, flat fielding, and astrometric calibration (McCully et al., 2018).

The *Liverpool Telescope* (LT; Steele et al., 2004) is a robotic 2.0 m telescope that observed Mrk 817 in the *ugriz* bands between 2021 January and 2022 January. The images were processed by the standard LT reduction pipeline.

The *Dan Zowada Memorial Observatory* (Carr et al., 2022) uses a 20-inch robotic PlaneWave telescope that provided the campaign with high cadence imaging in the *ugriz* filters. However, we excluded the Zowada u-band data from our lightcurves since the S/N was substantially lower than the u-band data obtained at other sites. Zowada began observing in 2020 November and continued through the end of the campaign.

At the *Wise Observatory*, the Centurion 18-inch telescope (Brosch et al., 2008) provided a near-daily cadence for observations in the *griz* filters. However, the z band data was excluded from our final lightcurves due to its low S/N in comparison with other telescopes. Images were processed for bias and dark subtraction, and flatfielding using IRAF routines. Observing ran from 2020 November through 2022 April.

The *West Mountain Observatory* (WMO) BYU 0.9-m reflector observed Mrk 817 in the in the B and V filters. All images from WMO were processed using IRAF for overscan, bias subtraction, dark subtraction, flatfielding, and astrometric calibration. WMO observed

[1] `https://archive.lco.global`

Mrk 817 from the start of the campaign until 2021 December. Additional data were obtained in the Johnson-Cousins R-band filter, but the R-band data were not used in this work due to the substantial difference in passbands between Johnson-Cousins R and the SDSS r' filters used at the other participating facilities.

The *Calar Alto Observatory* (CAHA) 2.2 m telescope and the *Yunnan Observatory* (LJ) 2.4 m telescope observed Mrk 817 in the V band. Observations at these facilities ran from November 2020 through May 2022.

Imaging with the *Asiago Observatory* (AS) 1.22 m telescope in the *BVugri* bands occurred during 2021 October through December. Due to the relatively high latitude of the Asiago site at 45°52′, these observations were able to fill in the seasonal gap when most other sites were not able to observe Mrk 817.

Exposure times ranged from 45 s to 300 s depending on telescope and filter. At most sites two exposures were taken per filter at each nightly visit. After combining data from all telescopes, the median observing cadence for each filter is: 0.9 days in u (379 visits), 0.9 days in B (302 visits), 0.4 days in g (1019 visits), 0.9 days in V (468 visits), 0.4 days in r (1048 visits), 0.4 days in i (934 visits), and 0.7 days in z (724 visits). The visit numbers listed above correspond to the number of epochs in the final light curves after rejection of bad data and outlier data points resulting from poor weather or instrument problems.

Figure 4.1 illustrates the Swift and ground-based filter passbands in comparison to the spectral shape of Mrk 817, using an HST STIS UV/optical spectrum obtained during the STORM 2 campaign.[2] The STIS spectrum is composed of observations with the G140L, G230L, G430L, and G750L gratings that were obtained on 2022 January 2. (Analysis of the STIS data will be presented in future papers in this series.) The strong Hα emission line

[2]Based on observations made with the NASA/ESA Hubble Space Telescope, obtained at the Space Telescope Science Institute, which is operated by the Association of Universities for Research in Astronomy, Inc., under NASA contract NAS5-26555. These observations are associated with program #16196.

Label	Camera–CCD	Pixel Scale ($''$/pix)	FOV	Filters
LCOGT-V37	Sinistro	0.389	$26\farcm5 \times 26\farcm5$	$BVu'g'r'i'z_s$
LCOGT-V39	Sinistro	0.389	$26\farcm5 \times 26\farcm5$	$BVu'g'r'i'z_s$
LCOGT-Z31	Sinistro	0.389	$26\farcm5 \times 26\farcm5$	$BVu'g'r'i'z_s$
LCOGT-Z24	Sinistro	0.389	$26\farcm5 \times 26\farcm5$	$BVu'g'r'i'z_s$
LCOGT-F65	MuSCAT3	0.270	$9\farcm1 \times 9\farcm1$	$g'r'i'z_s$
Wise	QSI 683 (KAF-8300)	0.882	$48.9' \times 36.8'$	$g'r'i'z'$
WMO	FLI PL-3041	0.490	$25\farcm2 \times 25\farcm2$	BVR
LT	IO:OO	0.304	$10' \times 10'$	$u'g'r'i'z'$
ZOW	SBIG STL-1001e	0.882	$30' \times 30'$	$u'g'r'i'z_s$
CAHA	2Kx2K	0.530	$11' \times 11'$	V
LJ	E2V42-90	0.286	$10' \times 10'$	V
AS	ON-Semi KAF-16803	0.870	$59' \times 59'$	$Vu'r'i'$

Table 4.2: Camera properties

falls at the red end of the r filter passband, with a small part of the Hα flux contained in the i band, while the B, g, and V bands overlap the region containing Hβ and prominent Fe II blends. The u band includes a substantial contribution from the "small blue bump" consisting of Balmer continuum and Fe II emission.

4.3.2 Additional processing steps

The facility data reduction pipelines for each instrument included basic steps such as bias subtraction and flat-fielding, and in most cases also included adding World Coordinate System (WCS) information to the image headers. For a subset of the telescopes, we carried out additional processing steps as described below to prepare the data for photometric measurements.

Fringe correction: Most of the telescopes show some degree of fringing in the i and z-band images. This can be addressed by subtracting a fringe frame. However, we only carried

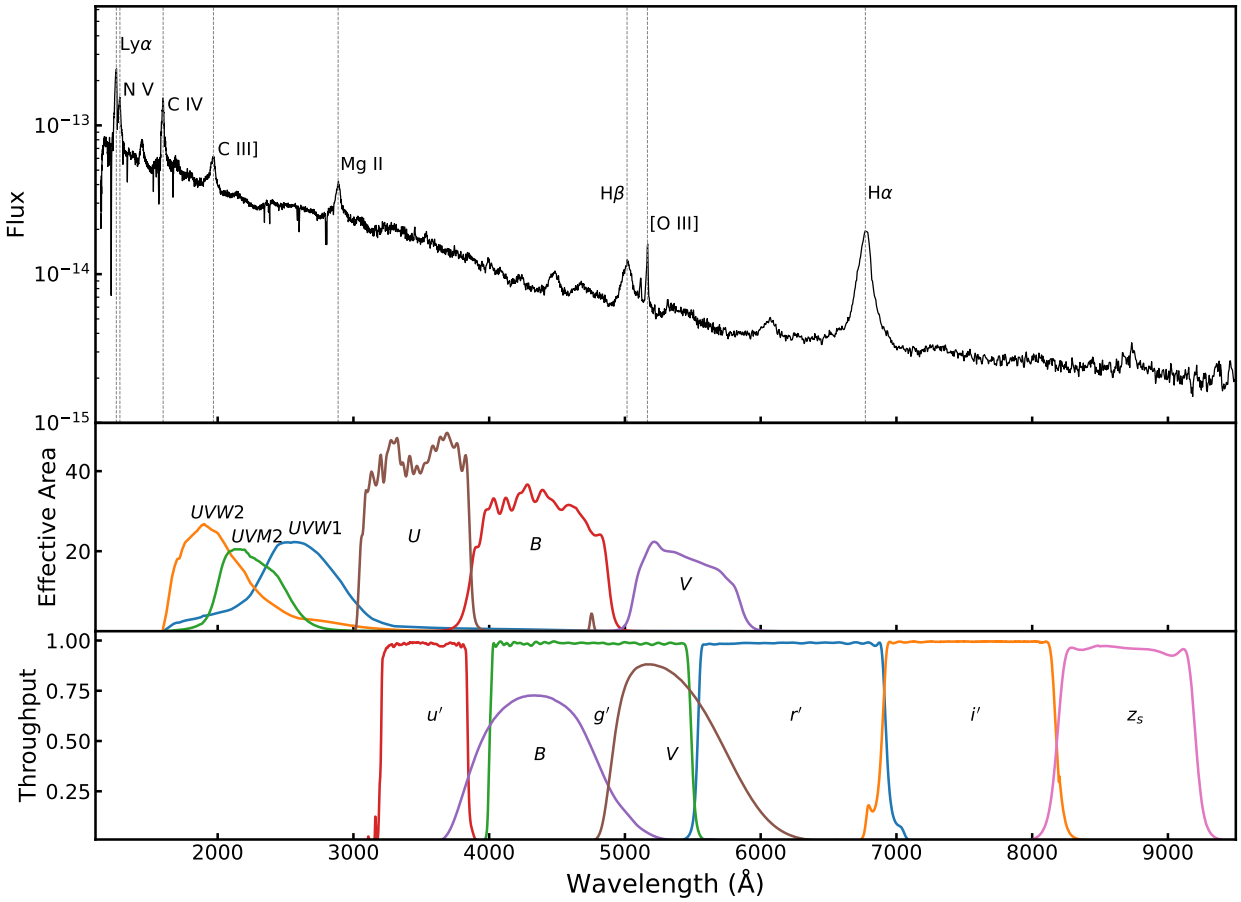

Figure 4.1: Top: HST STIS spectrum of Mrk 817 observed on 2022 January 2. Middle: Effective area curves for the Swift UVOT filter bands. Bottom: Transmission curves for the LCO filter set.

out fringe correction for the Zowada z-band data where the fringing was particularly severe. We created a fringe flat frame by combining 20 exposures aimed toward random blank sky fields and removing sources by clipping $>3\sigma$ outliers. A scaled version of the fringe flat was subtracted from each z-band image of Mrk 817, where the normalization of the fringe flat was determined by finding the scale factor that minimized the background sky rms in the fringe-subtracted frame. This effectively removed the fringe pattern and reduced the scatter in the Zowada z-band light curve.

Astrometric calibration: The instrument pipelines for Lijiang and Calar Alto did not include determination of an astrometric solution. For images from these facilities, we used `astrometry.net` (Lang et al., 2010) to add WCS information to the image headers.

4.4 Light Curve Measurements

Photometric reverberation mapping campaigns often include data from multiple telescopes that have different camera, detector, and filter properties resulting in inhomogeneous data sets that require extra care to produce well-calibrated light curves. We created an aperture photometry pipeline designed specifically for AGN photometric monitoring campaigns such as STORM 2. The method was based in part on an earlier IDL-based pipeline for AGN photometry described by Pei et al. (2014). Our pipeline is written in Python 3 and is based on Astropy routines (Astropy Collaboration et al., 2013, 2018a, 2022). It incorporates the PyCALI method of Li et al. (2014) to intercalibrate the light curves obtained from different telescopes. This pipeline has previously been used for the first results of the Mrk 817 STORM 2 campaign (Kara et al., 2021), as well as campaigns on NGC 4395 (Montano et al., 2022), Mrk 335 (Kara et al., 2023), and PG 1302-102 (Liu et al., 2024). Below we provide a detailed description of the method.

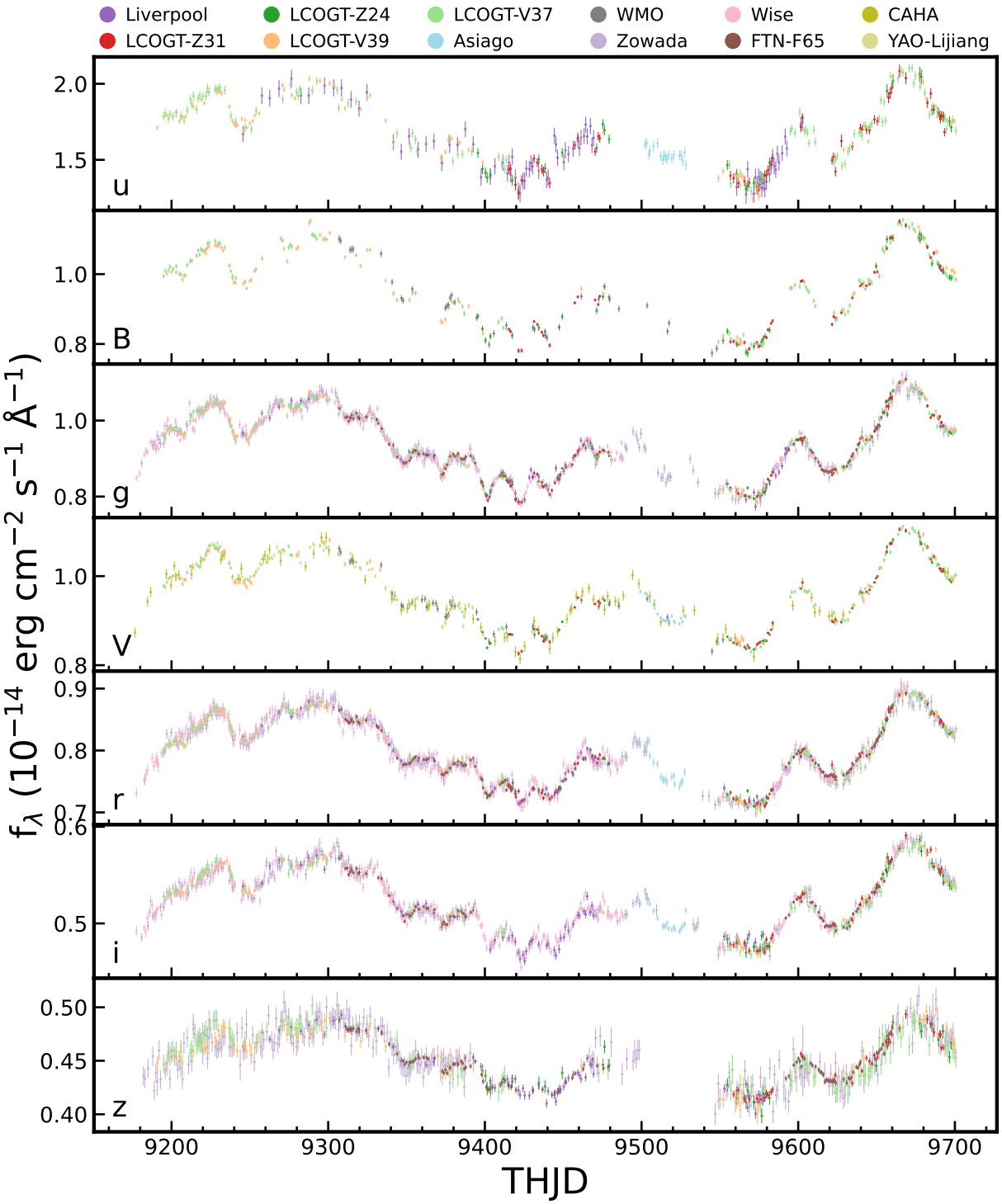

Figure 4.2: Mrk 817 light curves for the STORM 2 campaign including data from all telescopes, after averaging of multiple data points from the same visit, intercalibration, error expansion, and outlier rejection. Data points are color-coded by telescope as shown at the top of the plot.

The first step is ensuring a uniform system of time is applied to all of the image headers. We first calculate the Heliocentric Julian Date (HJD) and Modified Julian Date (MJD) for the midpoint of each exposure using the information in each image header. For the STORM 2 campaign we use HJD as our time standard and in this paper we list dates as truncated HJD (defined as THJD = HJD − 2450000). The date conversion is performed via the PyAstronomy package (Czesla et al., 2019).[3]

For a given AGN field, the code takes as an input a list of coordinates (right ascension and declination) for the AGN and for a set of comparison stars selected in the field. In each image, the AGN and comparison stars are identified by their coordinates using the Astropy WCS package, and their precise pixel coordinates are then determined by centroiding. To ensure that the centroid is determined accurately we perform two iterations of centroiding for each object, first with a 10″ square box and then with a 5″ square box to refine the centroid position. For the Mrk 817 field, we selected a set of 5 comparison stars, although for some cameras with smaller fields of view only 3 or 4 of the comparison stars were used.

For the photometric measurements we use the `aperture_photometry` function within the `photutils.aperture` package of AstroPy, employing the default `method='exact'` option to calculate fractional-pixel contributions at the edges of the photometric aperture. We adopt a standard aperture radius of 5″ and a background annulus spanning 15″–20″ for sky level estimation across all image sets. To determine the sky level within the background annulus we follow a method similar to that used by *DAOphot* (Stetson, 1987), in which the sky level is taken to be 3 times the median pixel value minus 2 times the mean value within the sky annulus, after clipping of outlier pixels. The derived sky value is then scaled by the number of pixels in the photometric aperture and subtracted from the aperture measurement. The photometric uncertainty is determined by the photon statistics and read noise within the

[3] `https://github.com/sczesla/PyAstronomy`

aperture. The 5″ photometric aperture radius is the same as that used for the STORM 2 Swift UVOT photometry (Cackett et al., 2023).

Due to transparency variations and airmass differences, the raw photometry from each night must be normalized to a consistent flux scale. For a given filter we carry out the normalization separately for each telescope and then merge the data from all of the telescopes at a later stage. The photometric measurements are normalized by determining a scale factor to apply to the measurements from each image. We calculate the scale factors via simultaneous fitting of all the scaled comparison star light curves assuming that the comparison stars are intrinsically non-variable. Using the comparison star photometry we calculate a scale factor s for each image through a χ^2 minimization, minimizing the following quantity:

$$\chi^2 = \sum_{i=1}^{K} \sum_{j=1}^{N} \frac{(s_j f_{ij} - \bar{f}_i)^2}{(s_j \sigma_{ij})^2} \tag{4.1}$$

where K is the number of comparison stars, N the number of images, s_j is the scale factor for image j, f_{ij} the count rate and σ_{ij} the uncertainty for star i in image j, and $\bar{f}_i$ is the mean count rate for star i across the time series. After determining the optimal scale factor for each image, the count rate and uncertainties for the AGN and comparison star are multiplied by that scale factor to obtain the scaled light curves.

To convert the scaled count rates to flux units we obtain comparison star magnitudes from the APASS catalog (Henden et al., 2018). These magnitudes are then converted to units of erg s^{-1} cm^{-2} $Å^{-1}$ using zeropoints from Fukugita et al. (1996) and Bessell et al. (1998). For each telescope and filter, we determine a conversion factor from count rate to f_λ by determining the conversion factor individually for each comparison star based on its mean count rate in the scaled light curve. The mean conversion factor for all comparison stars (after removal of any outliers) is then applied to the AGN light curve.

Multiple measurements from a given telescope taken within a window of < 0.25 day are considered to be a single "visit" and combined by weighted averaging to produce a single data point. The pipeline saves two versions of the AGN light curve, one including each individual photometric measurement and one with the nightly averaging applied. For the analysis and plots in this paper we use the nightly averaged light curves.

A common problem in AGN photometry based on data from multiple telescopes is that differences in wavelength-dependent throughput for different telescopes, combined with the color differences between the AGN and the comparison stars, can result in slight offsets in the overall flux scales of the AGN light curves after applying the above procedures. These offsets can be noticeable even among telescopes having the same camera and filter designs, such as those of the LCO 1 m network (e.g., Hernández Santisteban et al., 2020). Additionally, the measurement uncertainties at this stage are only based on photon-counting and detector noise statistics and do not account for other sources of systematic error such as seeing variations or flat-fielding errors. To address these issues we apply an intercalibration procedure to bring the flux scales from different telescopes into agreement and adjust the error bars to account for additional systematics.

For intercalibration we use PyCALI, a code that applies an additive shift and a multiplicative scale factor to align each telescope's light curve to a common flux scale (Li et al., 2014). PyCALI employs a damped random walk (DRW) to model the AGN's variability along with a Markov Chain Monte Carlo (MCMC) process to find the best parameters and uncertainties.

We implement two modifications compared with the typical application of PyCALI. The first is that we apply PyCALI to the data twice in order to obtain a better DRW model fit. We found that due to the small statistical errors on the photometric data points the DRW model fit from the first PyCALI run exhibited too much high-frequency structure as the model strained to fit the individual data points. After the first PyCALI run we then expanded the errors on the data points following the procedure described below and ran

Band	HJD−2450000	f_λ	$\sigma(f_\lambda)$	Telescope
g	9177.6342	0.8492	0.0079	Wise
g	9179.6347	0.8609	0.0101	Wise
g	9180.9856	0.8880	0.0117	Zowada
g	9182.3568	0.9091	0.0073	Wise
g	9183.6165	0.9204	0.0096	Wise
g	9184.6137	0.9167	0.0100	Wise
g	9186.6141	0.9442	0.0094	Wise
g	9187.6282	0.9429	0.0086	Wise
g	9188.0049	0.9336	0.0126	Zowada
g	9188.6245	0.9312	0.0079	Wise

Table 4.3: The listed HJD values give the midpoint time of each exposure. This table is published in its entirety in machine-readable format that includes all filters. A portion is shown here for guidance regarding its form and content. f_λ and $\sigma(f_\lambda)$ are in units of (10^{-15} erg cm^{-2} s^{-1} Å^{-1})

PyCALI again on the intercalibrated light curves. The second PyCALI run then produced a smoother DRW model fit that provided a better intercalibration of the light curves.

The second modification to the standard PyCALI procedures was to expand the errors on the data points through an additional error term added in quadrature. The additional error term is determined by finding the value that yields $\chi^2_{\rm dof} = 1$ with respect to the DRW model. This additional error term was determined individually for each telescope. After the first PyCALI run and error expansion we rejected data points that were $> 3\sigma$ outliers with respect to the DRW model fit. After the second PyCALI run the errors were adjusted again with the same procedure to obtain $\chi^2_{\rm dof} = 1$ for each telescope individually. By applying the error bar expansion separately to each telescope's data, this procedure preserves the high S/N of the best-quality light curves, such as those from the FTN 2 m telescope in the *griz* bands. In the final, error-expanded light curves, the median S/N is 52, 143, 126, 196, 110, 123, and 53, respectively, in the *uBgVriz* bands.

The final intercalibrated, uncertainty-expanded light curves are shown in Figure 4.2.

4.5 Lag Analysis and Results

4.5.1 Lag Measurements

We measure lags using three independent methods: ICCF (Gaskell & Peterson, 1987a; White & Peterson, 1994), JAVELIN (Zu et al., 2010), and PyROA (Donnan et al., 2021). Details for each measurement method are described below.

Our analysis of the continuum lags also incorporates the UV continuum light curves measured from the HST COS spectra as presented in Paper II (Homayouni et al., 2023) and the Swift UVOT bands from Paper IV (Cackett et al., 2023). For the HST and Swift UVOT lags we adopt the values from Paper IV. As a consistency check, we re-measured the lags for the HST and Swift bands with each method and found results in close agreement with those in Paper IV. All lags are measured with the Swift UVW2 light curve as the reference/driving light curve. We also tested measuring lags with the HST 1180 Å light curve as the reference band, but found that the Swift UVW2 band produced better results due to the higher temporal cadence of the Swift light curve.

4.5.1.1 ICCF

Reverberation lags are calculated for each filter band using the standard interpolated cross-correlation (ICCF) method, using the code PyCCF (Sun et al., 2018b). This method uses linear interpolation across gaps between data points to calculate the correlation between unevenly sampled time series, with lag uncertainties estimated by flux randomization and random subset sampling (FR/RSS). We use $N = 10000$ iterations with an interpolation sampling interval of 0.1 days, and a lag search range of -30 to 30 days. The adopted lag $\tau_{\rm cen}$ is the median of the CCF centroid distribution with 1σ uncertainties reported. For each iteration $\tau_{\rm cen}$ was calculated using points in the CCF above $0.8r_{\rm max}$ where $r_{\rm max}$ is the

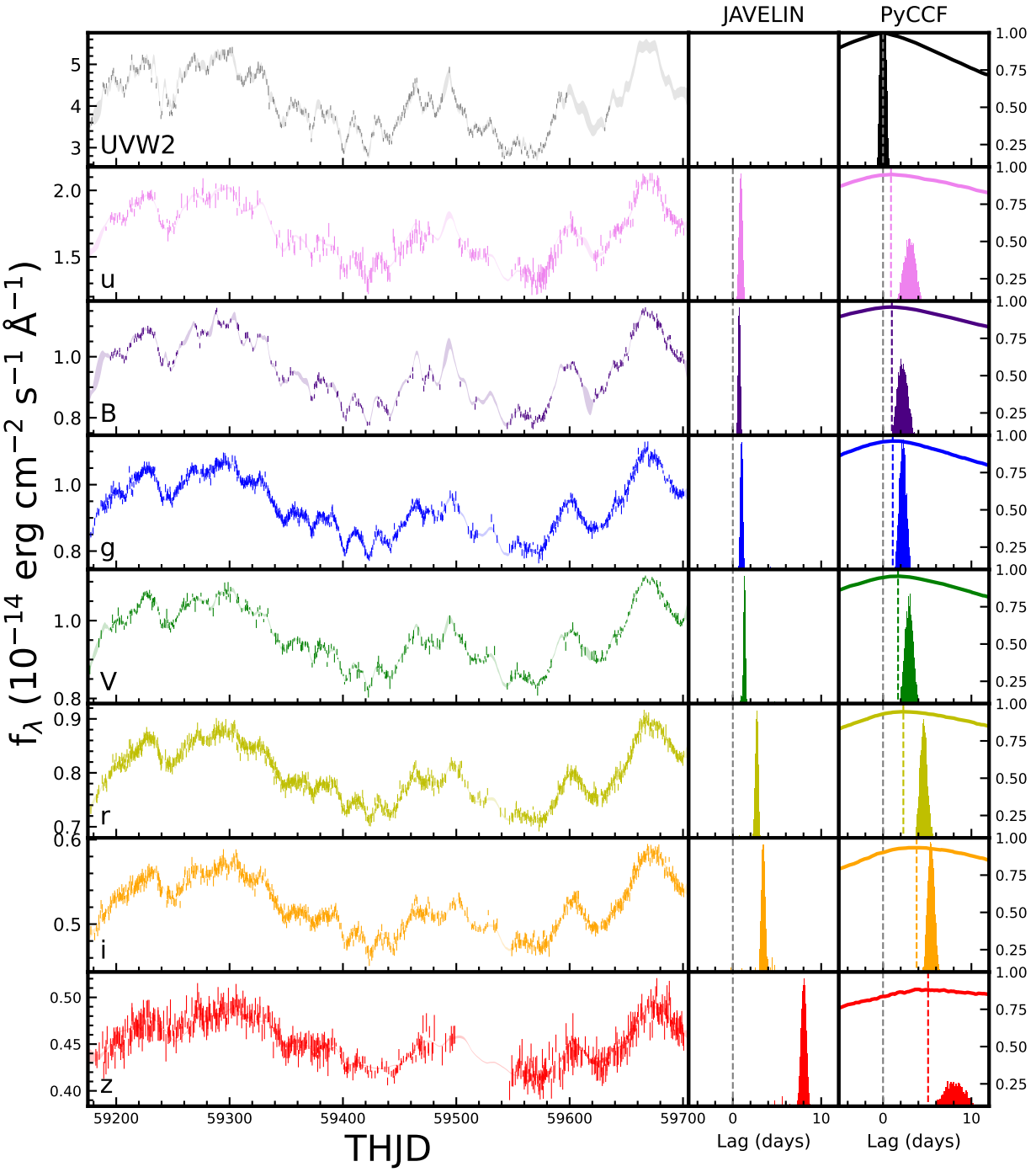

Figure 4.3: Left panels present the Mrk 817 light curves and JAVELIN DRW models (shaded curves) for all ground-based filters and the Swift UVW2 band that is used as the driving band for lag measurements. The Swift UVW2 DRW model is from JAVELIN fitting to the UVW2 and u bands. The right panels show the JAVELIN posterior distributions, the cross-correlation of each band with the UVW2 light curve, and CCF centroid distributions. The gray vertical dashed lines denote zero lag, and colored dashed lines indicate $\tau_{\rm peak}$.

peak in the CCF. The CCFs and CCF centroid distributions are illustrated in Figure 4.3. We also report $\tau_{\rm peak}$, the centroid of the distribution of CCF peak lags from the FR/RSS iterations. All the optical light curves show high correlation with the UVW2 light curve, with peak correlation coefficients ($r_{\rm max}$) of 0.94-0.96 for the u through i bands, and 0.88 for the z band which has lower S/N and a higher degree of host galaxy contamination than the shorter-wavelength bands.

4.5.1.2 JAVELIN

Just Another Vehicle for Estimating Lags In Nuclei (JAVELIN; Zu et al., 2011, 2013) estimates the time lag delays by modeling the light curves as a DRW and assuming that the driving and responding light curves are related by a top-hat transfer function. This process uses an MCMC method to determine posterior distributions for parameters including the lag and the DRW damping timescale. We fit pairs of light curves rather than fitting all light curves simultaneously (always using UVW2 as the driving band) as we found that the computational time was prohibitive when fitting more than two bands at once, due to the large number of data points in the light curves.

The JAVELIN DRW light curve models are shown in Figure 4.3 along with the posterior distributions of the lags.

4.5.1.3 PyROA

PyROA is a Python package that uses a Running Optimal Average (ROA) algorithm to model the light curves. The free parameters of the PyROA model include the light curve mean A_i, the light curve rms B_i, the width for the ROA function Δ, the time lag τ_i, and the extra error σ_i (also referred to extra variance). The extra error term in our fits always con-

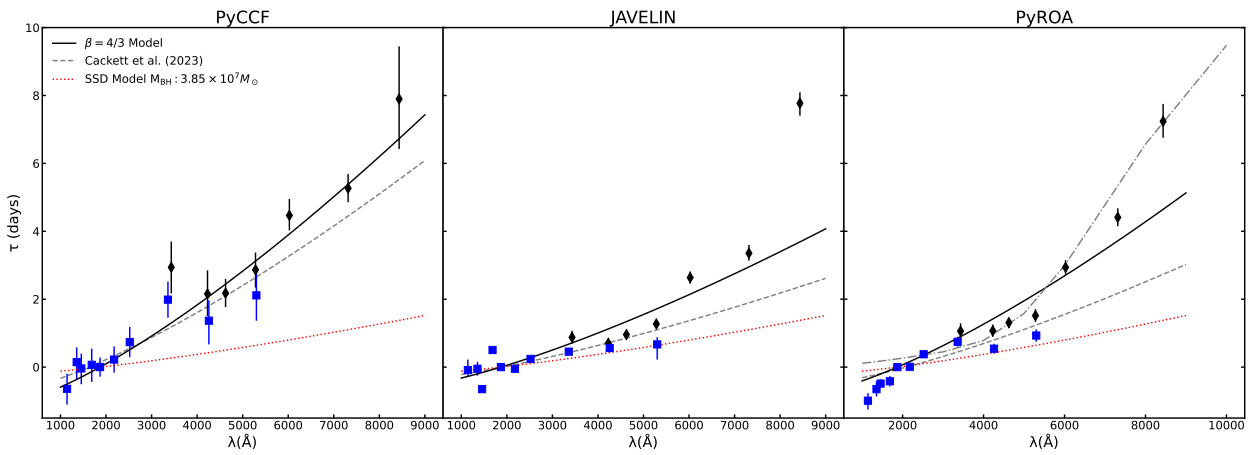

Figure 4.4: Mrk 817 lags measured using PyCCF, JAVELIN, and PyROA. Wavelengths and lags are shown in the rest frame. Blue squares are space-based measurements (HST and Swift; Cackett et al., 2023) and black diamonds are the lags for the ground-based bands. Black curves are the $\beta = 4/3$ power-law models (Equation 4.2) fitted to the data. Gray dashed lines represent fits to the HST and Swift data points as presented by Cackett et al. (2023). Inclusion of the ground-based lags leads to an increase in the normalization factor τ_0, primarily due to the longer lags in the *riz* bands. Red dotted curves correspond to the expected lag spectrum for lamp-post reprocessing by a Shakura-Sunyaev thin disk (Equation 4.3) for the assumed parameters of Mrk 817. The dash-dotted line in the rightmost panel is the best-fitting Bowl model as described in Section 4.6.3.

verged to the minimum allowed value due to the light curves already having the uncertainties adjusted. PyROA uses an MCMC method to find the best parameters and uncertainties.

Similar to JAVELIN, PyROA allows the option to fit all light curves simultaneously, but we found that the PyROA runs did not converge properly when applied to the HST, Swift and ground-based filter bands together. Instead we ran PyROA on light curve pairs using UVW2 and each ground-based band. For consistency we measured the HST and Swift lags simultaneously to compare to the results in Cackett et al. (2023) which agreed well within 1σ. The time delays reported are the median value of the posterior distributions with uncertainties from the 16th to 84th percentile that were estimated via the MCMC methods.

Band/Filter	$\lambda_{\rm cent}$ (Å)	$\tau_{\rm cen}$ (days)	$\tau_{\rm peak}$ (days)	$r_{\rm max}$	$\tau_{\rm JAV}$ (days)	$\tau_{\rm ROA}$ (days)
HST-COS 1180	1180	$-0.66^{+0.48}_{-0.46}$	$-0.68^{+0.24}_{-0.19}$	0.88	$-0.09^{+0.18}_{-0.32}$	$-1.02^{+0.27}_{-0.23}$
HST-COS 1398	1398	$0.15^{+0.51}_{-0.45}$	$-0.34^{+0.19}_{-0.19}$	0.90	$-0.05^{+0.21}_{-0.21}$	$-0.67^{+0.22}_{-0.24}$
HST-COS 1502	1502	$-0.04^{+0.48}_{-0.45}$	$-0.34^{+0.19}_{-0.19}$	0.95	$-0.67^{+0.08}_{-0.05}$	$-0.50^{+0.13}_{-0.13}$
HST-COS 1739	1739	$0.07^{+0.52}_{-0.49}$	$-0.24^{+0.34}_{-0.24}$	0.94	$-0.52^{+0.07}_{-0.07}$	$-0.43^{+0.16}_{-0.16}$
Swift UVW2	1928	$0.00^{+0.29}_{-0.29}$	$0.00^{+0.10}_{-0.10}$	1.00	$0.00^{+0.01}_{-0.01}$	$0.00^{+0.10}_{-0.10}$
Swift UVM2	2246	$0.23^{+0.40}_{-0.40}$	$-0.19^{+0.53}_{-0.15}$	0.99	$-0.05^{+0.08}_{-0.08}$	$0.01^{+0.08}_{-0.08}$
Swift UVW1	2600	$0.76^{+0.46}_{-0.46}$	$0.39^{+0.10}_{-0.15}$	0.98	$0.25^{+0.07}_{-0.07}$	$0.39^{+0.10}_{-0.10}$
Swift U	3465	$2.05^{+0.55}_{-0.55}$	$0.48^{+0.10}_{-0.15}$	0.97	$0.47^{+0.07}_{-0.07}$	$0.77^{+0.15}_{-0.15}$
Swift B	4392	$1.41^{+0.72}_{-0.62}$	$0.48^{+0.29}_{-0.19}$	0.95	$0.58^{+0.08}_{-0.08}$	$0.56^{+0.15}_{-0.15}$
Swift V	5468	$2.18^{+0.77}_{-0.72}$	$0.68^{+1.36}_{-0.34}$	0.94	$0.69^{+0.46}_{-0.22}$	$0.96^{+0.19}_{-0.19}$
u	3540	$2.94^{+0.77}_{-0.76}$	$0.90^{+1.73}_{-2.33}$	0.95	$0.88^{+0.19}_{-0.19}$	$1.06^{+0.24}_{-0.23}$
B	4361	$2.16^{+0.65}_{-0.69}$	$1.00^{+1.02}_{-1.62}$	0.96	$0.71^{+0.11}_{-0.11}$	$1.07^{+0.18}_{-0.18}$
g	4770	$2.18^{+0.41}_{-0.42}$	$1.10^{+0.55}_{-1.45}$	0.96	$0.96^{+0.13}_{-0.13}$	$1.31^{+0.15}_{-0.15}$
V	5448	$2.87^{+0.53}_{-0.51}$	$1.70^{+0.86}_{-1.86}$	0.96	$1.27^{+0.12}_{-0.10}$	$1.52^{+0.18}_{-0.19}$
r	6215	$4.47^{+0.44}_{-0.48}$	$2.30^{+1.61}_{-2.71}$	0.95	$2.64^{+0.18}_{-0.18}$	$2.94^{+0.21}_{-0.21}$
i	7545	$5.27^{+0.41}_{-0.43}$	$3.80^{+0.93}_{-2.23}$	0.94	$3.35^{+0.22}_{-0.24}$	$4.41^{+0.26}_{-0.27}$
z	8700	$7.90^{+1.47}_{-1.55}$	$5.10^{+1.25}_{-4.25}$	0.88	$7.71^{+0.36}_{-0.32}$	$7.24^{+0.48}_{-0.51}$

Table 4.4: Reverberation lags for the full STORM 2 campaign for Mrk 817, measured by the ICCF, Javelin, and PyROA methods. Central wavelengths are in the observed frame and lags are in the rest frame of Mrk 817. HST and Swift lags reported here are reproduced from Table 2 of Cackett et al. (2023).

4.5.2 Full Campaign Lags

The lags for the full campaign are reported in Table 4.4 for all three measurement methods and shown as lag-wavelength spectrum plots in Figure 4.4. For completeness, Table 4.4 also includes the lags for the HST and Swift bands presented in Paper IV. All methods show lags increasing with wavelength in agreement with previous STORM 2 results (Kara et al., 2021; Cackett et al., 2023) and consistent with most broad-band continuum RM studies for other AGN. Consistent with earlier results from Cackett et al. (2023), the PyCCF measurements exhibit a distinct excess lag in the U/u bands, but the JAVELIN and PyROA lags do not show consistent evidence for a u-band excess.

Comparing the lags obtained from the three methods, we find that PyCCF generally yields longer lags than JAVELIN or PyROA, as previously found by Cackett et al. (2023) for the HST and Swift bands. This is a likely consequence of using the CCF centroid (rather than the CCF peak) to quantify the lag, since the CCFs have asymmetric shapes with excess power at lags longer than the peak (Figure 4.3. The asymmetry in the CCFs can result from the shape of disk reprocessing transfer functions due to the radial temperature profile of the disk (Cackett et al., 2007), and DC and line emission from the BLR will contribute a tail extending to lags well beyond the peak. As found in Paper I from the first segment of the STORM 2 campaign, the Hβ lag in Mrk 817 is $\sim$23 days, significantly longer than the optical broad-band continuum lags found here.

In contrast, Javelin and PyROA lags are more directly sensitive to the peak of the lag distribution due to the assumption of a symmetrical transfer function, resulting in lags that are generally smaller than $\tau_{\rm cen}$ obtained from the ICCF method. We also find that PyCCF yields larger lag uncertainties than the other methods, as is typically the case in prior reverberation studies. Investigations of the uncertainties returned by lag measurement methods have found that the FR/RSS method tends to overestimate the lag errors (Yu

et al., 2019); Gaskell (2024) finds FR/RSS errors to be too large by a factor of 1.36. Javelin, on the other hand, may strongly underestimate the lag uncertainties in some cases due to the method's assumptions, including the assumption that the driving and responding light curves follow a DRW process and are related via a simple top-hat transfer function (Gaskell, 2024). The Mrk 817 light curves are seen to violate this assumption, particularly during the decorrelation episode that occurred in epoch 1 (Cackett et al., 2023).

The wavelength range covered by the Swift and ground-based filters overlaps across the UBV bands (see Figure 4.1). We find that the ground-based lags are consistently slightly longer than the corresponding Swift-based lags for each overlapping filter and for all three lag measurement methods. The mean differences in lag between the overlapping space and ground-based bands are $\Delta_\tau = 0.78$ days for lags measured with PyCCF, $\Delta_\tau = 0.37$ days with JAVELIN, and $\Delta_\tau = 0.45$ days with PyROA. These differences are within the 1σ uncertainties for PyCCF, and within 3σ for JAVELIN and PyROA (where both the lag differences and their uncertainties are smaller than for PyCCF). The reason for these differences is not clear, and may be due to the differences between the ground-based and Swift filter passbands and/or the different cadence of the ground-based light curves.

To evaluate the trend of lag with wavelength we fit an offset power-law model to the lag spectrum as done in many other works (e.g., Fausnaugh et al., 2016; Edelson et al., 2019). The model has the form

$$\tau = \tau_0[(\lambda/\lambda_0)^\beta - 1] \tag{4.2}$$

where τ is the rest-frame lag, $\lambda_0 = 1928/(1+z)$ Å is the reference wavelength (corresponding to the rest-frame wavelength at the center of the UVW2 band), β is fixed to 4/3 corresponding to a basic disk reprocessing model, and the free parameter τ_0 sets the normalization of the lag spectrum.

The fits to the lag spectra measured with each method yield $\tau_0 = 1.04 \pm 0.05$ days with $\chi^2/\mathrm{dof} = 1.03$ for PyCCF, $\tau_0 = 0.57 \pm 0.08$ days with $\chi^2/\mathrm{dof} = 23.9$ for JAVELIN, and $\tau_0 = 0.72 \pm 0.11$ days with $\chi^2/\mathrm{dof} = 28.3$ for PyROA. All χ^2/dof are reported for 15 degrees of freedom. While there are 17 continuum bands (including HST, Swift, and ground-based bands; see Table 4.4) and one free parameter in the fit, the model of Equation 4.2 is constructed to pass precisely through the UVW2 data point having zero lag, so the UVW2 point does not count toward the number of degrees of freedom in the fit.

For comparison, we have also included in Figure 4.4 the power-law model from Cackett et al. (2023) that was fitted to just the HST and Swift data points. Cackett et al. (2023) used a model of the form $\tau = \tau_0[(\lambda/\lambda_0)^\beta - y_0]$, with y_0 as a free parameter rather than fixed as in our Equation 4.2, so the fit is not forced to coincide with the UVW2 data point (but the fitted curves fall very close to the UVW2 point nevertheless). For each lag measurement method, we find that including the ground-based bands yields a larger normalization τ_0, due to the longer lags measured for the ground-based uBV bands compared with their Swift equivalents, and the significantly longer lags of the riz bands. Our τ_0 values are larger by factors of 1.25, 1.49, and 1.78 than the values obtained by Cackett et al. (2023) from fits to the space-based points, for PyCCF, JAVELIN, and PyROA, respectively.

To compare our results with predictions for lamp-post reprocessing by a thin disk, we adopt the model described by Fausnaugh et al. (2016). This model assumes a geometrically thin, optically thick accretion disk that is irradiated by an X-ray corona. The standard thin disk model has a temperature profile of $T(R) \propto R^{-3/4}$. Assuming a relationship between characteristic emitted wavelength λ and disk temperature of the form $\lambda = Xhc/kT$, while $R = c\tau$ (the time lags converted to light-travel distance) then yields the $\tau \propto \lambda^{4/3}$ lag-wavelength relation. Here, X is a factor that specifies the relation between $T(R)$ and λ for a given R, accounting for the fact that multiple radii contribute to the emission at any given wavelength. Specifically, we use $X = 2.49$ corresponding to a flux-weighted mean radius for

a disk that emits locally as a blackbody (see Equation 10 of Fausnaugh et al., 2016). The predicted value of τ_0 (Equation 12 from Fausnaugh et al., 2016) is then

$$\tau_0 = \frac{1}{c}\left(X\frac{k\lambda_0}{hc}\right)^{4/3}\left[\left(\frac{GM}{8\pi\sigma}\right)\left(\frac{L_{\rm Edd}}{\eta c^2}\right)(3+\kappa)\,\dot{m}_{\rm E}\right]^{1/3}. \tag{4.3}$$

We adopt $\eta = 0.1$ for the radiative efficiency, and $\kappa = 1$ for the ratio of external to internal (viscous) heating of the disk and an Eddington ratio of 0.2. These assumptions yield $\tau_0 =$ 0.213 days which is much smaller than the values obtained from fits to the observed lag spectrum, as illustrated in Figure 4.4. For PyCCF the lags are a factor of 4.9 times longer, for JAVELIN a factor of 2.7 times longer, and for PyROA a factor of 3.4 times longer than the disk reprocessing model prediction. These discrepancy factors are similar to values found for other AGN (e.g., Fausnaugh et al., 2016; Edelson et al., 2019), although it should be emphasized that the magnitude of the discrepancy depends on multiple uncertain factors including the assumed values of X, η, and Eddington ratio in Equation 4.3.

While in general PyCCF produces longer lags than the other methods, the z-band lags are consistent (within their 1σ uncertainties) for all three measurement methods, at 7.2-7.9 days. The PyCCF lag spectrum is reasonably well fit by the power-law model across all bands from the far-UV through z, but for JAVELIN and PyROA the z-band points are notable outliers above the model fits, and contribute significantly to the high χ^2 values. These long z-band lags in excess of the $\lambda^{4/3}$ model fits may be an indication of an additional contribution to the delays from hot dust emission, originating in the inner dusty torus, as discussed by Netzer et al. (2024). Modeling of near-infrared spectroscopic data from the STORM 2 campaign indicates that the dust responsible for the near-IR continuum in Mrk 817 has $T \approx 1400$ K (Landt et al., submitted). While thermal emission from dust at ~ 1400 K is expected to make only a small ($\sim$few percent) contribution to the total flux in the z band (e.g., Hönig, 2014), the dust emission variations will have a much longer lag than the disk and BLR emission

components, adding a long tail to the overall z-band response function that can have a significant impact on the broad-band lag. This possibility can be further explored in future work by applying methods such as MEMECHO (Horne et al., 2021) to examine the response function shape and search for evidence of multiple components in the lag distribution.

4.5.3 Lags of Short-Duration Epochs

Filter-Band				
	Epoch 1			
	$\tau_{\rm cen}$	$r_{\rm max}$	$\tau_{\rm JAV}$	$\tau_{\rm ROA}$
HST 1180	$-1.17^{+0.47}_{-0.43}$	0.80	$-1.33^{+0.24}_{-0.17}$	$-0.77^{+0.14}_{-0.14}$
HST 1398	$-0.67^{+0.46}_{-0.45}$	0.85	$-1.56^{+0.10}_{-0.13}$	$-0.60^{+0.16}_{-0.16}$
HST 1502	$-0.30^{+0.41}_{-0.39}$	0.93	$-0.20^{+0.13}_{-0.11}$	$-0.38^{+0.16}_{-0.15}$
HST 1739	$0.59^{+0.53}_{-0.48}$	0.91	$-0.72^{+0.20}_{-0.20}$	$-0.71^{+0.25}_{-0.25}$
Swift UVW2	$0.23^{+0.58}_{-0.64}$	0.97	$0.00^{+0.14}_{-0.15}$	$0.16^{+0.16}_{-0.16}$
Swift UVW1	$0.47^{+0.60}_{-0.72}$	0.95	$0.50^{+0.27}_{-0.27}$	$0.49^{+0.28}_{-0.28}$
Swift U	$1.31^{+0.69}_{-0.72}$	0.88	$1.92^{+0.45}_{-0.45}$	$1.53^{+0.46}_{-0.45}$
Swift B	$1.46^{+1.00}_{-1.12}$	0.83	$1.80^{+0.79}_{-0.87}$	$2.11^{+0.59}_{-0.58}$
Swift V	$2.84^{+1.12}_{-0.96}$	0.80	$3.54^{+0.67}_{-0.63}$	$3.81^{+0.60}_{-0.56}$
Ground u	$1.80^{+0.46}_{-0.67}$	0.85	$1.85^{+0.08}_{-0.11}$	$1.81^{+0.43}_{-0.45}$
Ground B	$1.66^{+0.74}_{-0.73}$	0.86	$1.65^{+0.71}_{-0.71}$	$1.62^{+0.39}_{-0.37}$
Ground g	$2.71^{+0.25}_{-0.25}$	0.87	$1.74^{+0.25}_{-0.25}$	$2.04^{+0.35}_{-0.36}$
Ground V	$2.97^{+0.68}_{-0.64}$	0.81	$3.46^{+0.70}_{-0.63}$	$2.56^{+0.39}_{-0.40}$
Ground r	$4.50^{+0.32}_{-0.33}$	0.78	$3.85^{+0.29}_{-0.31}$	$3.64^{+0.45}_{-0.45}$
Ground i	$5.52^{+0.38}_{-0.34}$	0.80	$5.20^{+0.36}_{-0.33}$	$4.98^{+0.43}_{-0.41}$
Ground z	$7.60^{+1.54}_{-1.37}$	0.64	$8.96^{+1.01}_{-1.02}$	$9.83^{+0.94}_{-0.97}$
	Epoch 2			

	$\tau_{\rm cen}$	$r_{\rm max}$	$\tau_{\rm JAV}$	$\tau_{\rm ROA}$
HST 1180	$-0.48^{+0.95}_{-0.95}$	0.68	$-0.46^{+0.96}_{-0.10}$	$-0.65^{+0.14}_{-0.14}$
HST 1398	$0.26^{+1.83}_{-1.09}$	0.70	$-0.44^{+0.08}_{-0.98}$	$-0.32^{+0.16}_{-0.16}$
HST 1502	$-0.38^{+0.90}_{-0.97}$	0.79	$-0.49^{+0.08}_{-0.09}$	$-0.46^{+0.16}_{-0.15}$
HST 1739	$-0.23^{+0.92}_{-0.98}$	0.82	$-0.20^{+0.47}_{-0.29}$	$-0.11^{+0.25}_{-0.25}$
Swift UVW2	$0.19^{+0.26}_{-0.48}$	0.96	$-0.05^{+0.20}_{-0.13}$	$-0.05^{+0.12}_{-0.11}$
Swift UVW1	$0.78^{+0.46}_{-0.94}$	0.93	$0.27^{+0.14}_{-0.14}$	$0.48^{+0.18}_{-0.17}$
Swift U	$0.77^{+0.47}_{-0.89}$	0.91	$0.23^{+0.20}_{-0.20}$	$0.47^{+0.21}_{-0.21}$
Swift B	$0.87^{+0.32}_{-0.89}$	0.85	$0.72^{+0.30}_{-0.30}$	$0.84^{+0.21}_{-0.21}$
Swift V	$0.99^{+0.71}_{-0.91}$	0.83	$0.84^{+0.47}_{-0.44}$	$0.80^{+0.27}_{-0.29}$
Ground u	$0.09^{+0.30}_{-0.48}$	0.91	$0.35^{+0.24}_{-0.49}$	$0.29^{+0.27}_{-0.28}$
Ground B	$0.62^{+0.26}_{-0.25}$	0.93	$0.79^{+0.26}_{-0.25}$	$1.01^{+0.23}_{-0.23}$
Ground g	$1.20^{+0.17}_{-0.16}$	0.96	$1.04^{+0.17}_{-0.16}$	$1.16^{+0.15}_{-0.16}$
Ground V	$1.44^{+0.38}_{-0.43}$	0.94	$0.97^{+0.38}_{-0.39}$	$1.58^{+0.20}_{-0.20}$
Ground r	$2.47^{+0.22}_{-0.25}$	0.93	$2.11^{+0.21}_{-0.23}$	$2.22^{+0.25}_{-0.25}$
Ground i	$3.41^{+0.20}_{-0.22}$	0.92	$3.09^{+0.19}_{-0.20}$	$3.21^{+0.24}_{-0.24}$
Ground z	$4.41^{+0.56}_{-0.64}$	0.89	$4.72^{+0.52}_{-0.61}$	$4.28^{+0.32}_{-0.33}$
	Epoch 3			
	$\tau_{\rm cen}$	$r_{\rm max}$	$\tau_{\rm JAV}$	$\tau_{\rm ROA}$
HST 1180	$-0.99^{+0.65}_{-0.87}$	0.92	$-0.73^{+0.08}_{-0.06}$	$-0.88^{+0.12}_{-0.12}$
HST 1398	$-0.29^{+0.66}_{-0.78}$	0.93	$-0.77^{+0.06}_{-0.06}$	$-0.57^{+0.11}_{-0.11}$
HST 1502	$-0.32^{+0.61}_{-0.70}$	0.94	$-0.77^{+0.06}_{-0.06}$	$-0.64^{+0.10}_{-0.11}$
HST 1739	$0.45^{+0.75}_{-0.79}$	0.94	$-0.08^{+0.22}_{-0.22}$	$-0.06^{+0.16}_{-0.16}$
Swift UVM2	$0.42^{+0.61}_{-0.59}$	0.98	$-0.04^{+0.15}_{-0.16}$	$-0.02^{+0.13}_{-0.12}$
Swift UVW1	$0.53^{+0.54}_{-0.52}$	0.98	$0.14^{+0.11}_{-0.11}$	$0.27^{+0.11}_{-0.10}$
Swift U	$1.90^{+0.53}_{-0.52}$	0.96	$0.35^{+0.16}_{-0.17}$	$0.46^{+0.16}_{-0.17}$

Swift B	$0.51^{+0.57}_{-0.52}$	0.96	$0.14^{+0.18}_{-0.19}$	$0.12^{+0.16}_{-0.16}$
Swift V	$1.52^{+0.72}_{-0.71}$	0.92	$0.26^{+0.37}_{-0.53}$	$0.26^{+0.22}_{-0.23}$
Ground u	$3.24^{+0.19}_{-0.55}$	0.91	$0.18^{+0.19}_{-0.49}$	$0.87^{+0.29}_{-0.29}$
Ground B	$0.52^{+0.19}_{-0.18}$	0.94	$0.15^{+0.19}_{-0.17}$	$0.27^{+0.22}_{-0.22}$
Ground g	$1.16^{+0.14}_{-0.15}$	0.95	$0.71^{+0.14}_{-0.14}$	$0.84^{+0.15}_{-0.14}$
Ground V	$2.74^{+0.36}_{-0.61}$	0.96	$0.22^{+0.34}_{-0.53}$	$1.27^{+0.16}_{-0.17}$
Ground r	$3.76^{+0.32}_{-0.30}$	0.94	$4.32^{+0.27}_{-0.28}$	$3.00^{+0.25}_{-0.26}$
Ground i	$4.58^{+0.32}_{-0.29}$	0.90	$4.28^{+0.28}_{-0.27}$	$4.03^{+0.32}_{-0.33}$
Ground z	$5.67^{+0.74}_{-0.73}$	0.80	$5.31^{+0.67}_{-0.71}$	$6.10^{+0.80}_{-0.72}$

Table 4.5: All epoch lags in AGN's rest-frame with the same methods as reported in previous tables. For pyCCF we report the centroid lag along side the maximum of the correlation coefficient.

The long duration of the STORM 2 campaign and the high S/N of the light curves provides an opportunity to measure the broad-band lags over shorter-duration subsets of the full monitoring campaign, and to test for changes in lag that might be correlated with variations in AGN luminosity or obscuration.

In Paper VII (Lewin et al., 2024), a frequency-resolved lag analysis was performed, and the campaign was split into three epochs of equal duration to examine changes in lag. The first and third epochs had higher time-averaged X-ray obscuration ($\bar{N}_{\rm H} = 12.6 \times 10^{-22}$ cm^{-2} and 12.9×10^{-22} cm^{-2}) in comparison with the second epoch ($\bar{N}_{\rm H} = 6.1 \times 10^{-22}$ cm^{-2}), based on X-ray measurements from Paper III (Partington et al., 2023). Lewin et al. (2024) found that the lags corresponding to low-frequency flux variations (at frequencies of $0.014 - 0.048$ day^{-1}) were longer during the first and third epochs, when obscuration was higher, and the amplitude of the lag spectrum (i.e., the inferred value of τ_0 for lags in this frequency range) dropped by nearly a factor of two during Epoch 2 compared with Epochs 1 and 3.

Here, we follow up on this investigation and measure time delays for the same three epochs, to test whether the standard methods for lag determination yield similar results for the variation in lags across the duration of the full campaign. We adopt THJD 9317 and 9457 as the boundaries between Epochs 1 and 2, and between Epochs 2 and 3, following Lewin et al. (2024).[4] For each epoch, we measured the lags of each band relative to UVW2 following the same procedures described in Section 4.5.1, using PyCCF, JAVELIN, and PyROA. The derived lags for each epoch, band, and method are listed in Table 4.6. A notable change across the three epochs is seen in the $r_{\rm max}$ values, where the optical bands show consistently lower correlations with the UVW2 light curve during Epoch 1 than during Epochs 2 and 3. These differences stem from the wavelength-dependent divergence in light curve shapes that temporarily occurred near the start of the campaign (during THJD $\approx 9220 - 9320$), as highlighted by Cackett et al. (2023) from the HST and Swift data.

The lag spectrum for each epoch was then fitted with the power-law model of Equation 4.2. The epoch lags are illustrated in Figure 4.5 and the τ_0 and $\chi^2_{\rm dof}$ values from each fit are listed in Table 4.6. For Epochs 1 and 2, we obtain systematically longer lags and larger τ_0 values than the low-frequency lags measured by Lewin et al. (2024) (see Figure 6 of Paper VII), while for Epoch 3, the mean of the τ_0 values from PyCCF, JAVELIN, and PyROA is consistent with the value of $\tau_0 = 0.66 \pm 0.5$ days obtained by Lewin et al. (2024) for low-frequency variations.

Our overall results for the lag variations show trends that differ somewhat from those found in Paper VII from the frequency-resolved analysis, in which the lags were found to be shorter during the period of lower obscuration and longer during periods of higher obscuration. The largest change is seen between Epochs 1 and 2, where we find a factor of $\sim$2 drop in τ_0 with all three lag measurement methods (from $\tau_0 = 1.12$ to 0.57 days, averaged over the three

[4]Lewin et al. chose these epoch boundaries in order to split the Swift light curves into segments of about 140 days each, and we select these same boundaries for consistency with their analysis. However, in our ground-based data the third epoch extends over a longer duration because of the later end date of the ground-based campaign relative to the Swift campaign.

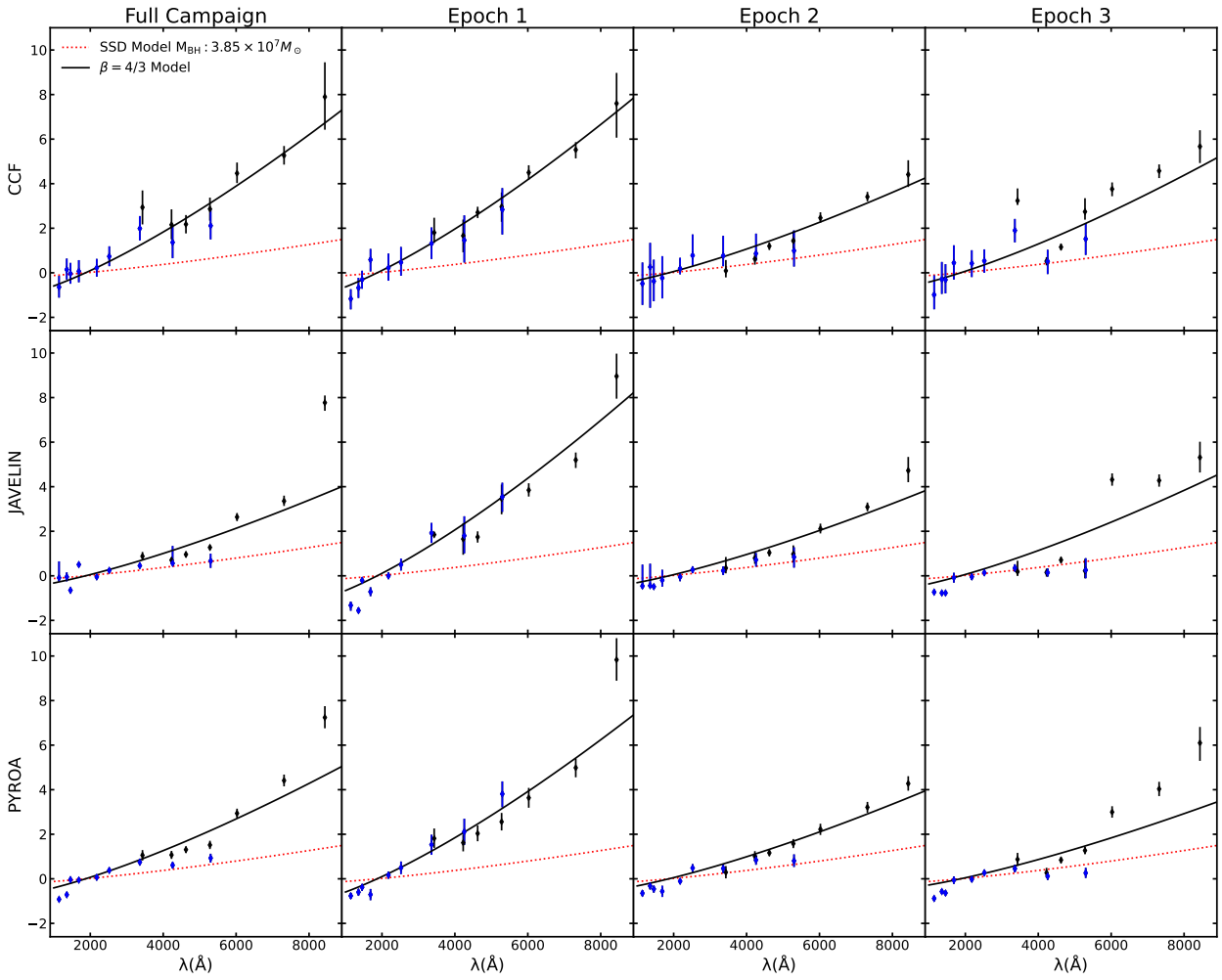

Figure 4.5: Lag-wavelength plots for the full campaign and for the three epochs, for each lag measurement method. Model curves are as described in Figure 4.4. Blue points are the space-based (HST+Swift) lag measurements, while black points are all ground-based.

Method	τ_0(Full Campaign)	χ^2/dof
PyCCF	1.04 ± 0.05	1.03
JAVELIN	0.57 ± 0.08	23.9
PyROA	0.72 ± 0.11	28.3
	τ_0(Epoch 1)	χ^2/dof
PyCCF	1.12 ± 0.02	0.58
JAVELIN	1.18 ± 0.09	12.15
PyROA	1.05 ± 0.07	2.24
	τ_0(Epoch 2)	χ^2/dof
PyCCF	0.61 ± 0.02	1.11
JAVELIN	0.55 ± 0.03	2.82
PyROA	0.56 ± 0.07	2.91
	τ_0(Epoch 3)	χ^2/dof
PyCCF	0.76 ± 0.07	7.67
JAVELIN	0.64 ± 0.14	31.3
PyROA	0.49 ± 0.09	14.25

Table 4.6: All τ_0 values are in units of days, and are obtained from fitting Equation 4.2 to the rest-frame lags as shown in Figure 4.5. The reduced χ^2 values are for 15 degrees of freedom.

measurement methods). However, we find only small changes in lag between Epochs 2 and 3, in contrast to the frequency-resolved results from Paper VII, where τ_0 was found to increase again nearly to the same level as in Epoch 1. Our PyCCF and JAVELIN measurements show small increases in τ_0 from Epoch 2 to Epoch 3, while the PyROA lags yield a slight decrease in τ_0 (although the ground-based lags are generally longer in Epoch 3 than Epoch,2).

All epochs exhibit a disk size discrepancy in comparison with the reprocessing model of Equation 4.3, with the largest discrepancies found during the first epoch. For the PyCCF measurements, the magnitude of the discrepancies for each epoch (i.e., the ratio of observed to predicted values of τ_0) are a factor of 5.3 for Epoch 1, 2.9 for Epoch 2, and 3.6 for Epoch 3. For JAVELIN the corresponding factors are 5.5, 2.6, and 3.0 for Epochs 1, 2, and 3, respectively, while for PyROA we obtain factors of 4.9, 2.6, and 2.3 for the three epochs.

As described earlier, in the JAVELIN and PyROA measurements for the full campaign duration, the z-band lag is an outlier falling well above the best-fit power-law model. The

epoch measurements show that these long z-band lags appear to be primarily driven by the behavior during Epoch 1, where the z-band lag reaches $\sim 8-10$ days. In Epochs 2 and 3 the z band lag still falls above the fitted power-law trend for each measurement method, but in Epoch 2 it is reduced by roughly half in comparison to Epoch 1.

4.6 Flux-Flux Analysis

4.6.1 Full Campaign

The flux-flux analysis method (Winkler et al., 1992; Hernández Santisteban et al., 2020) decomposes the observed light curves into variable and constant components, with the goal of recovering the spectral energy distribution (SED) of the time-variable AGN emission. Cackett et al. (2023) carried out a flux-flux analysis of the STORM 2 light curves from HST and Swift, finding that the rms variability spectrum follows a spectral shape of $f_\nu \propto \lambda^{-1/3}$ from the UV through V bands. Here, we extend this flux-flux analysis by adding the ground-based light curves and by examining the flux-flux SED components in the three epochs described in Section 4.5.3. To match the duration of the space-based light curves, we removed the final 35 days from the ground-based light curves for this analysis. The light curves are first corrected for Galactic reddening of $E(B-V) = 0.022$ mag and using the Cardelli et al. (1989) extinction law with $R_V = 3.1$.

Following the same methods described by Cackett et al. (2023), we fit the data with a dimensionless model light curve $X(t)$ that is shifted by an additive offset $A_\nu(\lambda)$ and scaled by $S_\nu(\lambda)$ to fit each band's light curve, where $S_\nu(\lambda)$ and $A_\nu(\lambda)$ are free parameters and $X(t)$ is constrained to have $\langle X \rangle = 0$ and $\langle X^2 \rangle = 1$. Then, the resulting light curve for wavelength

λ is

$$f_\nu(\lambda, t) = A_\nu(\lambda) + S_\nu(\lambda)X(t). \tag{4.4}$$

The fitted flux-flux light curve relations are shown in Figure 4.6. The best-fit scale factors $S_\nu(\lambda)$ give the rms variability amplitude for each wavelength band. To obtain the constant component of the SED, we find the value X_G where the lower error envelope on the flux-flux relation for the shortest-wavelength band (1180 Å) reaches zero flux. Then, for each band the value of f_ν at $X = X_G$ is taken to be the constant component flux for that band.

Figure 4.7 shows the variable and constant component SEDs derived for Mrk 817 (the left panel shows the SEDs derived for the full STORM 2 campaign duration). Our results for the space-based bands reproduce the earlier measurements shown in Paper IV. For the region of wavelength overlap between the Swift and ground-based bands (the UBV bands), we find reasonable agreement between the rms flux values for corresponding Swift and ground-based bands. Fitting a power law to the rms variability spectrum, we find a best-fit model of $f_\nu \propto \lambda^{-0.38}$, close to the characteristic $\lambda^{-1/3}$ spectrum of a standard accretion disk over the optical wavelength range.

4.6.2 Individual Epochs

To check whether there are detectable variations in the variable and constant SED components across the duration of the campaign, we applied the flux-flux analysis to the three individual epochs described in Section 4.5.3. The results are shown in Figure 4.7 for comparison with the full campaign measurements. The primary result is that the inferred variable and constant SED components during Epoch 1 differ substantially from their spectral shapes as measured over the full campaign and over the second and third epochs. During Epoch 1,

Filter Band	Mean f_ν	Bright f_ν	Faint f_ν	S_ν	A_ν
1180 Å	4.61	6.50 ± 0.07	2.47 ± 0.06	1.11 ± 0.01	0.08 ± 0.04
1398 Å	5.00	6.48 ± 0.06	2.47 ± 0.05	1.07 ± 0.01	0.66 ± 0.03
1502 Å	5.23	6.73 ± 0.06	2.56 ± 0.05	1.14 ± 0.01	0.60 ± 0.03
1739 Å	5.62	7.56 ± 0.25	2.65 ± 0.25	1.20 ± 0.04	0.76 ± 0.12
UVW2	6.04	5.98 ± 0.14	2.12 ± 0.09	1.00 ± 0.02	2.10 ± 0.05
UVM2	7.27	6.90 ± 0.24	2.32 ± 0.23	1.12 ± 0.03	2.86 ± 0.10
UVW1	7.59	6.31 ± 0.24	2.13 ± 0.17	1.01 ± 0.3	3.62 ± 0.08
U (Swift)	8.61	6.00 ± 0.25	1.73 ± 0.17	0.95 ± 0.03	4.89 ± 0.09
B (Swift)	7.73	4.08 ± 0.06	1.37 ± 0.09	0.86 ± 0.02	4.56 ± 0.07
V (Swift)	6.71	4.45 ± 0.14	1.48 ± 0.13	0.65 ± 0.01	4.13 ± 0.03
u	7.93	5.13 ± 0.29	1.45 ± 0.18	0.69 ± 0.03	5.21 ± 0.08
B	7.83	4.32 ± 0.21	1.11 ± 0.18	0.62 ± 0.01	5.30 ± 0.01
g	10.38	3.88 ± 0.07	1.22 ± 0.09	0.75 ± 0.01	7.38 ± 0.02
V	8.81	3.94 ± 0.26	1.21 ± 0.21	0.61 ± 0.03	6.41 ± 0.02
r	11.12	3.94 ± 0.12	1.20 ± 0.09	0.63 ± 0.01	8.60 ± 0.02
i	10.62	3.54 ± 0.11	0.90 ± 0.09	0.55 ± 0.01	8.39 ± 0.02
z	12.11	3.47 ± 0.35	0.70 ± 0.20	0.51 ± 0.02	10.02 ± 0.05

Table 4.7: Units for all columns except the filter bands are mJy. The last two columns are the additive shift A_ν (the constant component of the light curve) and the scaling value S_ν for the variable component. Bright and faint values are the maximum and minimum values of the light curve after subtraction of the constant component.

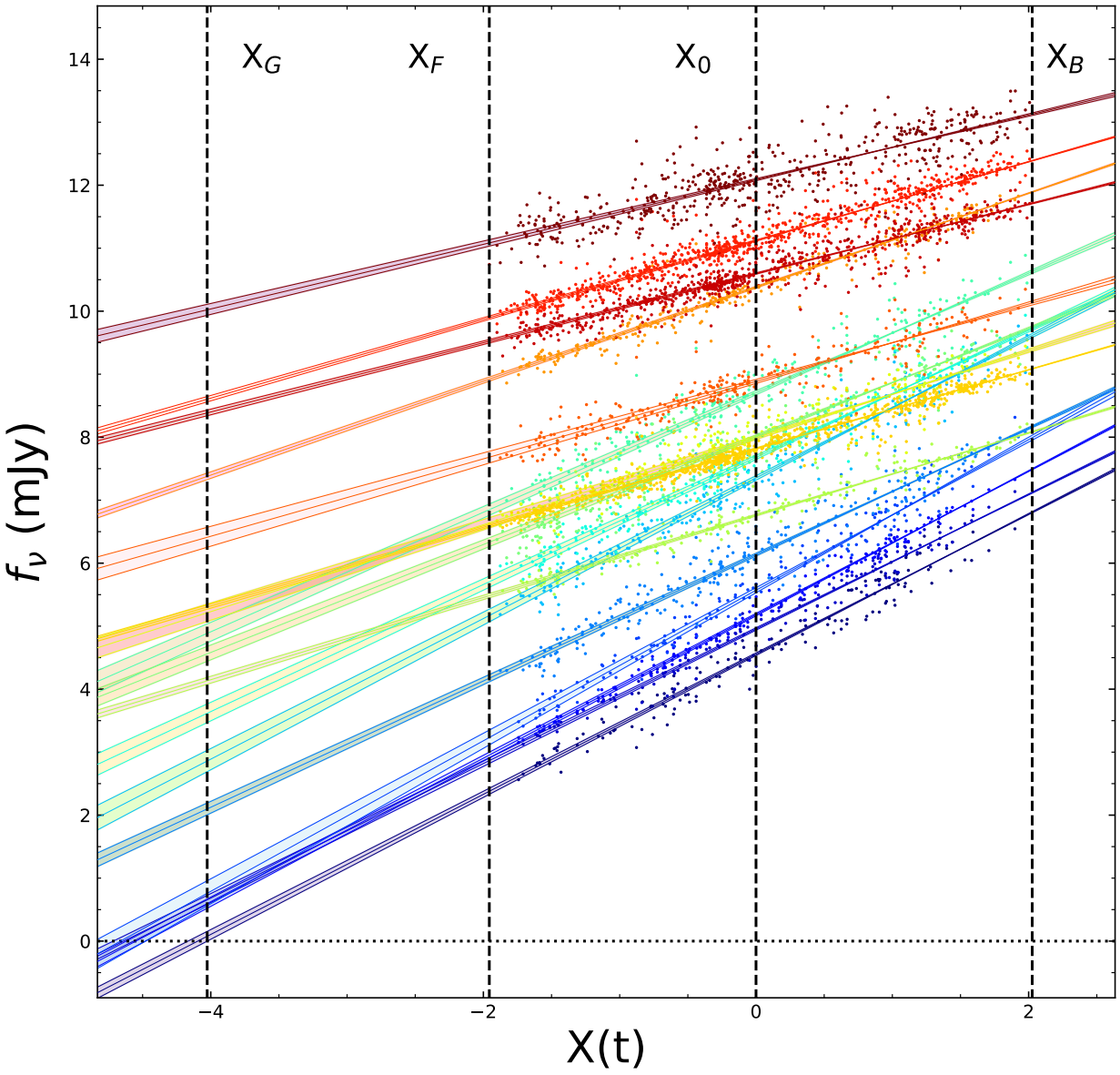

Figure 4.6: Flux-flux relations for the full campaign duration for each UV and optical band, with the 1180 Å band at the bottom (dark violet) and z at the top (dark red). The data for each band show the variability range of the light curves, and the lines show the fit of Equation 4.4 to each band along with its 1σ uncertainty range. The quantity X_G is the value of X that is used to establish the constant component flux for each band, as described in the text, and the slope of the fitted line for each band gives the variability amplitude parameter $S_\nu(\lambda)$ for that band. X_F and X_B are the faintest and brightest states of the light curves.

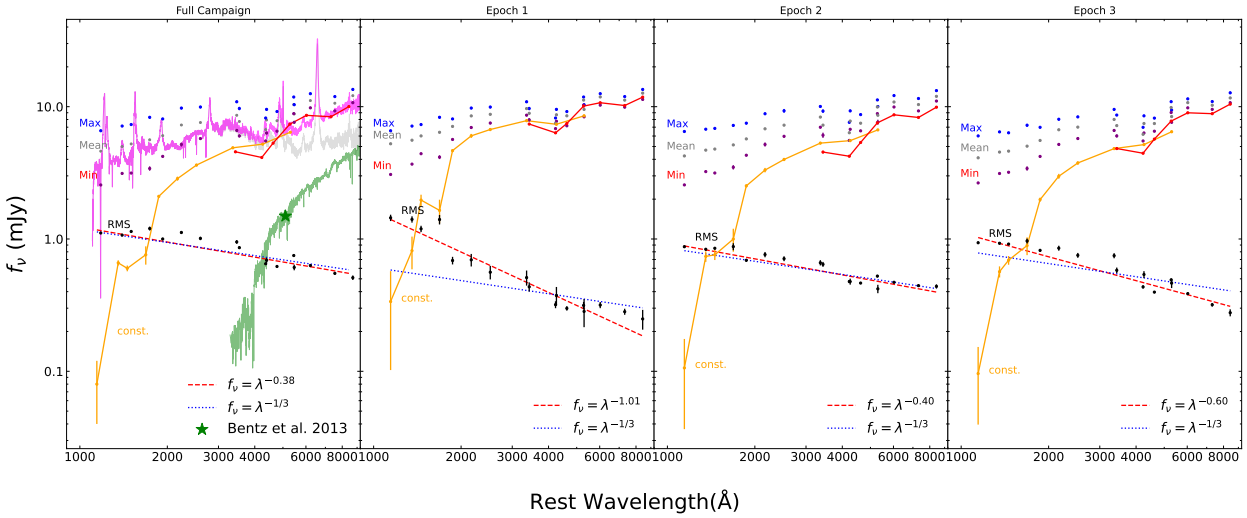

Figure 4.7: The SED components of Mrk 817 inferred from the flux-flux analysis for the full campaign (*left panel*) and for the three epochs. The rms spectrum is fitted with a $f_\nu \propto \lambda^{-1/3}$ model (the blue-dotted line) as expected for an accretion disk, and with a $f_\nu \propto \lambda^{\alpha}$ model with exponent α as a free parameter (the red-dashed line). Maximum, mean, and minimum values for the total flux in each band are shown at the top of the plot. The solid orange line represents the constant component inferred for the space-based bands, and the solid red line represents the the constant component for the ground-based bands. In the left panel, the green star represents the host galaxy flux at 5100 Å in a $5'' \times 12''$ rectangular aperture, from Bentz et al. (2013), and the green spectrum is a Bruzual & Charlot (2003) 11 Gyr model normalized to match the host galaxy flux at 5100 Å. The STIS spectrum of Mrk 817 is shown in light gray (the same spectrum as shown in Figure 4.1), and the sum of the STIS spectrum and the host galaxy template is shown in pink. Comparison of the flux-flux results with the AGN+host spectral model demonstrates that the flux-flux constant component is predominantly AGN light across the full spectral range.

the rms variability spectrum is best fit by a steeper $f_\nu \propto \lambda^{-1.01}$ power law, in contrast to the best-fitting power-law indices of -0.38 for the full campaign, and -0.40 and -0.60 for epochs 2 and 3. This appears to be a manifestation of the decoupling between the far-UV and near-UV variations that occurred during the early portion of the campaign. As illustrated in Figure 6 of Cackett et al. (2023), the 1180 Å and UVW2 light curves exhibit closely similar shapes over most of the STORM 2 campaign except during THJD $\approx 9220 - 9320$, when the 1180 Å light curve experienced a strong drop in flux followed by a recovery to its "normal" behavior tracking the UVW2 variations. This anomalous decline and subsequent recovery of the far-UV flux during Epoch 1 increased the variability amplitude of the far-UV bands relative to the near-UV, and these changes can be associated with the steeper slope of the flux-flux rms component's SED during Epoch,1.

We also find that the inferred constant SED component for Epoch 1 deviates strongly from the constant component measured for the full campaign and for the later epochs. In earlier work using the flux-flux technique, it is sometimes implicitly assumed that this so-called "constant" component primarily represents host-galaxy starlight, and the SED of this component is sometimes referred to as the "galaxy" contribution to the overall SED (e.g., Hernández Santisteban et al., 2020). Our results demonstrate that this inferred constant component can actually change substantially as the AGN varies, implying that it is dominated by slowly varying contributions of AGN light rather than by starlight. To illustrate these changes, Figure 4.8 presents the constant component SEDs for the three individual epochs and for the full campaign duration. While the Epoch 2 and 3 SEDs are quite similar to the full campaign SED, the constant component SED for Epoch 1 has a substantially higher flux across the spectrum, with the largest fractional change in the near-UV region.

As an additional check, we re-measured the constant component SED for each epoch based on the value of X_G obtained from the full-duration campaign, rather than using different X_G values for each epoch. The results showed that the constant component SED derived for

epoch 1 still differed significantly from those of epochs 2 and 3, similar to the results shown in Figure 4.8, demonstrating that the changes in the constant component SED are not just caused by epoch-to-epoch variations in X_G as derived from the 1180 Å band.

Previously, Cackett et al. (2023) noted that the near-UV emission in the constant component (from the flux-flux analysis of the full campaign duration) was too strong to be accounted for by host galaxy light alone, and suggested that it might arise from diffuse continuum or Fe II emission that varied more slowly than the ∼few-day reverberation timescale. We compared the flux-flux constant component strength with the host galaxy flux measured directly from HST imaging decompositions by Bentz et al. (2013). In a 5×12 arcsec^2 rectangular aperture (designed to coincide with the aperture used in an earlier spectroscopic reverberation mapping campaign, corresponding to 76% of the area of the $r = 5''$ circular photometric aperture used for the STORM 2 Swift and ground-based photometry), they measured a host galaxy flux density corresponding to 1.49 mJy at 5100 Å. This is a factor of 4.30 or 4.95 fainter than the Swift and ground-based V-band constant component fluxes determined from the flux-flux analysis, confirming that host galaxy starlight only contributes a small fraction of the flux-flux constant component spectrum. The host galaxy flux from Bentz et al. (2013) is shown in the left panel of Figure 4.7. We also show the spectrum of an 11 Gyr-old, Solar-metallicity stellar population from Bruzual & Charlot (2003), normalized to match the measured 5100 Å galaxy flux, to illustrate a simple spectral model for the host galaxy bulge in comparison with the flux-flux constant component.

Figure 4.7 also includes the HST STIS spectrum from 2022 January 2 (THJD 9581; the same spectrum shown in Figure 4.1), taken when Mrk 817 was close to its lowest flux during the STORM 2 campaign. We created a simple model for the combined AGN + host galaxy spectrum by adding the STIS spectrum and the normalized Bruzual & Charlot (2003) model spectrum, illustrated in pink in the left panel of Figure 4.7. At UV wavelengths the host galaxy contribution from the old stellar population is negligible. There may be some ad-

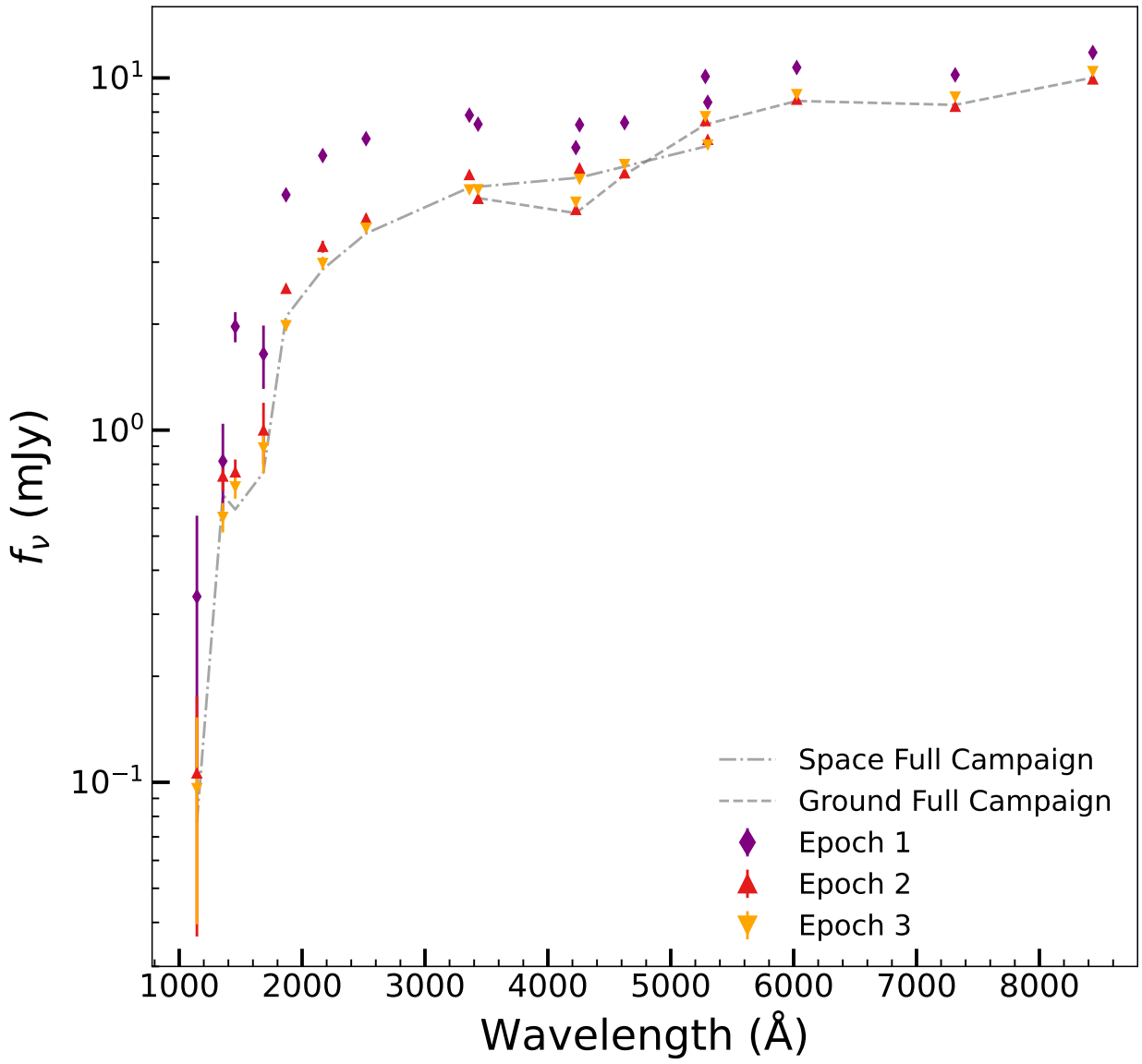

Figure 4.8: Comparison of the constant SED components inferred for the three epochs (individual points) and for the full campaign duration (dashed and dot-dashed curves, representing the ground-based and space-based bands, respectively). The Epoch 1 SED exhibits the largest difference from the full-campaign SED, with the strongest fractional variations at UV wavelengths.

ditional contribution to the host galaxy spectrum from a younger stellar population, but it is still likely to be very small in comparison with the AGN flux. The AGN+host model shows reasonably good agreement with the minimum-state SED obtained from the flux-flux analysis over most of the UV-optical spectral range. Comparison of this AGN+host model spectrum with the flux-flux constant component further confirms that the constant component is dominated by AGN light at UV and blue wavelengths, with the host galaxy contribution increasing at red wavelengths such that it accounts for $\sim 40\%$ of the constant component at the longest wavelengths.

Our results highlight a fundamental limitation in the flux-flux method: the relationship between light curve shapes in different bands is certainly much more complex than the simple scaling described by Equation 4.4, since at any wavelength there are multiple contributions to the variable flux that can vary on different timescales and with different lags. As a result, the flux-flux method does not separate AGN and host galaxy light as cleanly as has been assumed in some prior work. In future work on the flux-flux method, it would be worthwhile to explore whether the method can be extended to incorporate two (or more) time-variable components varying on different timescales, as a generalization of the model of Equation 4.4, in order to distinguish the SEDs of rapidly and slowly varying spectral components in the data and distinguish them from the genuinely constant host-galaxy contribution.

4.6.3 "Bowl" Model

The Bowl model (Starkey et al., 2022; Prince et al., 2025) retains blackbody reprocessing but replaces the zero-thickness disk geometry with a concave power-law disk thickness profile following a relation $H \propto R^{\beta}$ between disk height and radius. By tilting the outer disk reprocessing surface toward the central source of irradiation, the blackbody temperature is increased above the thin-disk profile $T \propto R^{-3/4}$. This shifts to shorter wavelengths the

reprocessed light from the outer-disk annuli, giving larger lags at each wavelength. The model parameters are constrained using MCMC methods to fit simultaneously the multi-band lag data and the AGN disk SED data at the faintest and brightest levels observed during the campaign. A preliminary Bowl model fit to the HST and Swift data was presented by Cackett et al. (2023), and here we describe a new fit incorporating the ground-based data to test whether this model can successfully match the observed SED shape and lag spectrum.

Figure 4.9 presents the results of fitting the Bowl model to the PyROA lags in Table 4.4, simultaneously with the faint and bright AGN disk SED data in Table 4.7 from the flux-flux analysis shown in Figure 4.6 and discussed in Section 4.6.1. Parameters held fixed include the luminosity distance $D_{\rm L} = 137\,{\rm Mpc}$, black hole mass $M = 4 \times 10^7\,{\rm M}_\odot$, disk inclination $i = 45°$, and inner disk radius $R_{\rm in} = R_g$. The MCMC fit drives the disk thickness power-law index β to large values, producing a flat disc with a steep outer rim. Fixing $\beta = 100$ picks out a typical representative of these geometries. Median parameters from 10^4 MCMC samples are reported on the plot. The seven primary fit parameters are 1) the disk rim radius $R_{\rm out} \sim 28$ light days, 2) the rim height $H/R \sim 0.3\%$, 3) the central irradiating lamp height $H_x \sim 4.4\,R_g$, 4) an upper limit on the accretion rate $\dot{M} < 0.02\,{\rm M}_\odot\,{\rm yr}^{-1}$, 5) the irradiation-driven temperature rise $\Delta T \approx 0.16\,{\rm dex}$, and rms uncertainties 6) $\sigma_0 \approx 15\%$ for the SED, and 7) $\sigma_\tau \approx 0.44\,{\rm d}$ for the lags. The noise model parameters σ_0 and σ_τ, added in quadrature with the SED and delay measurement uncertainties, serve to quantify the fit residuals. The MCMC samples indicate that these parameters are approximately independent, apart from a tight correlation between H_x and H/R.

The Bowl model fit reproduces the blue power-law slope of the AGN disk SED, the flux ratio between the faint and bright states, and the lags increasing with wavelength by about 8 days between 1000 and 9000 Å. The lags in this blackbody reprocessing model arise from a wavelength-dependent mix of prompt ($\tau < 1\,{\rm d}$) response from the flat disk, which dominates in the UV, and delayed response ($\tau \approx 30\,{\rm d}$) from the steep outer rim.

The fit is not entirely satisfactory, however, in several respects. First, the SED data are slightly bluer than the $F_\nu \propto \nu^{1/3}$ SED of the irradiated thin-disk model. The model SED also turns up on the red end due to reprocessing on the inward face of the steep rim. Finally, while in good accord with the optical lag data, the model lags are too flat across the UV, where HST lags are rising with wavelength. The Bowl model fit is strained by this tension between fitting red lags and avoiding a red upturn in the SED.

We note, however, that the Bowl model attempts to fit the full lag spectrum entirely as the result of blackbody reprocessing from the disk surface, with no contributions from line and nebular continuum emission from the BLR or dust emission from the torus. A more elaborate model incorporating one or both of these features could help to reduce this tension. For example, hot dust at the inner edge of the torus may be contributing to the lags in the reddest optical bands. A Bowl model with a second increase in thickness at that larger radius could be more successful. The first step in disc thickness could then move in from 30 to 10 light days, where a jump in thickness is expected as dust in the disk atmosphere evaporates. Here the wavelength dependence of H I bound-free plus free-free opacity should modulate the height of the steep rim and produce corresponding jumps in the lag spectrum. These elaborations (and others) are possible but beyond the scope of the current paper.

4.7 Discussion

4.7.1 Summary of Measurements

Earlier work in this series (Cackett et al., 2023) has presented reverberation lags and a flux-flux analysis for the HST and Swift continuum light curves of Mrk 817 measured during the STORM 2 campaign. In this paper, we have expanded on the earlier analysis by adding multiband ground-based photometric data to extend the wavelength coverage, and by carry-

ing out lag and flux-flux measurements over three separate epochs during the campaign (as defined earlier by Lewin et al., 2024) that were characterized by different levels of obscuration and luminosity.

Overall, we find that the optical light curves are highly correlated with the Swift UVW2 band, with $r_{\rm max} = 0.94 - 0.96$ for the for the u through i bands, and 0.88 for the z band. Cross-correlation functions for each band relative to UVW2 exhibit asymmetries toward longer lags beyond the CCF peak, likely indicative of extended transfer function structure that may result from multiple emission components contributing to the lags: diffuse continuum and emission lines from the BLR in addition to disk emission, and possibly dust emission from the inner torus at the longest wavelengths.

For measurements over the full campaign duration, our PyCCF lag measurements result in a lag spectrum that is well fitted by the typical $\tau \propto \lambda^{4/3}$ power-law model (Equation 4.2), and we find evidence of an excess lag in the u band, confirming the U-band excess seen earlier in the Swift data. Such excess lags in the U or u bands have been seen in numerous other AGN to date (e.g., Fausnaugh et al., 2016; Cackett et al., 2018, 2020a) and are attributed to the contribution of Balmer continuum emission from the BLR (Lawther et al., 2018; Korista & Goad, 2019). Measurements with JAVELIN and PyROA, in contrast, find somewhat shorter lags overall and little or no u-band excess (also consistent with the findings of Cackett et al., 2023), but the z-band lags are found to be outliers falling well above the best-fitting $\lambda^{4/3}$ models (Figure 4.4). The normalization τ_0 of the power-law fits to the lag spectra indicates a typical "disk size discrepancy" similar to results found for other AGN in intensive monitoring programs (see Cackett et al., 2021, for further discussion). Our derived values of τ_0 exceed the basic disk reprocessing prediction by factors of 2.7–4.9 for the three lag measurement methods. The τ_0 values found in this work are higher than those measured previously for the space-based STORM 2 data by Cackett et al. (2023), since the longer lags of the ground-based bands favor larger values of τ_0.

Figure 4.10 illustrates the changes in τ_0 across the three measurement epochs in comparison with the changes in the UVW2 flux and the X-ray absorbing column density $N_{\rm H}$ as measured from NICER data in Paper III (Partington et al., 2023). While our three lag measurement methods yield slightly different results for τ_0, they illustrate the same general trend in lags across the three epochs. The drop in τ_0 between Epochs 1 and 2 mirrors a decrease in both UV luminosity and in $N_{\rm H}$. Epoch 3 is characterized by nearly the same mean $N_{\rm H}$ as Epoch 1, and a mean luminosity similar to that in Epoch 2. We find that the epoch 3 lags are similar to the lags measured in Epoch 2, and still well below the longer Epoch 1 lags. This result differs somewhat from the findings of Lewin et al. (2024), as shown in Figure 4.10 (black points in the lower panel). In their frequency-resolved lag analysis, the lags in the lowest-frequency bin (corresponding to 20-70 day timescales) closely mirrored the changes in $N_{\rm H}$ across the three epochs since they found essentially equal lags during Epochs 1 and 3 (at $\tau_0 = 0.69 \pm 0.03$ and 0.66 ± 0.05 d, respectively) and a lower lag of $\tau_0 = 0.35 \pm 0.02$ during Epoch 2.

While we detect a typical u-band excess lag in the PyCCF measurements for the full campaign duration, JAVELIN and PyROA do not show this feature. This may be due to these two methods having less sensitivity to the long-lag tail in the transfer function, in comparison with the ICCF method that yields longer lags overall. A puzzling aspect of the results is that in the epoch-based measurements, the u-band excess is only present during epoch 3, an epoch characterized by relatively low UV and X-ray luminosity and elevated $N_{\rm H}$ (Partington et al., 2023; Cackett et al., 2023). It is surprising that the appearance of the u-band excess does not appear to correlate with the overall magnitude of the lags: if the DC emission is most dominant during Epoch 1, then a stronger u-band excess would be expected during that time. This behavior is different from that seen in Mrk 110, where the strength of the u-band excess lag across multiple monitoring epochs was seen to scale with X-ray luminosity (Vincentelli et al., 2022).

While these results extend the previous results of Paper IV, one difference is that Cackett et al. (2023) measured the HST/Swift continuum lags both before and after applying a detrending procedure to the light curves to remove low-frequency structure. In reverberation mapping, a low-order (linear or sometimes quadratic) detrending is often used in order to remove an overall increasing or decreasing trend in flux, so that cross-correlation analysis can better isolate the lags due to short-timescale variations (Welsh, 1999). In Mrk 817, the temporary divergence between the far-UV and near-UV light curve shapes during Epoch 1 is problematic for lag measurement methods such as JAVELIN and PyROA that fit the light curves under the assumption that the responding bands can be modeled as time-shifted and broadened versions of the driving continuum band. In order to obtain adequate fits to the light curves with these methods, Cackett et al. (2023) detrended the data by smoothing the light curves with a Gaussian kernel of width $\sigma = 20$ days and then subtracting the smoothed model from the data. This procedure amounts to a much higher-order correction than the linear detrending typically used in reverberation mapping. After this detrending, the lags for the Swift UBV bands and the derived values of τ_0 were shorter for all three lag measurement methods and close to the predictions for standard disk reprocessing. These results suggested that the longer-timescale (> 20 d) light curve variations produce contributions to the lags arising from nebular continuum and line emission in the BLR, while the shorter-timescale variations remaining in the detrended light curves are associated with lags arising on smaller spatial scales in the accretion disk.

Combining the HST, Swift, and ground-based light curves, Lewin et al. (2024) carried out a frequency-resolved lag analysis for Mrk 817. They were able to measure the lags independently across six frequency bins covering a range of 7×10^{-3} to 1.0 day^{-1}, finding a strong trend of decreasing lag as a function of frequency. Their results further support the conclusion that the lags corresponding to low-frequency variations are associated with reprocessing on the spatial scale of the BLR, while the lags occurring in response to high-frequency variations ($> .05$ d^{-1}) are associated with reprocessing at the scale of the disk. Since the work

of Lewin et al. (2024) provides a much more detailed view of the frequency-resolved lag behavior in the STORM 2 campaign in comparison with the detrending method of Cackett et al. (2023), we do not include detrended measurements as part of this work.

4.7.2 SED Variations and Impact of Disk Winds

The excellent data quality obtained during the STORM 2 program enabled the detection of significant temporal changes in continuum lag over shorter timescales than have been probed in most other campaigns, although recently there has been growing evidence for significant changes in continuum lags across timescales of years from long-duration monitoring datasets (Zhou et al., 2025; Su et al., 2025). The factor of 2 decrease in lag from epoch 1 to epoch 2 is much larger than what would be expected based solely on the $\tau \propto L^{0.5}$ scaling that has been found for samples of AGN having continuum reverberation mapping measurements (Netzer, 2022; Guo et al., 2022), since the mean fluxes in the 1180 Å and UVW2 bands each decreased by only ∼20% from epoch 1 to 2. If the optical continuum lags in Mrk 817 are dominated by DC emission from the BLR, then variations in the ionizing flux incident on the BLR are likely to be responsible for the changing lags, and recent work has considered the possible effects of time-variable wind obscuration (Lewin et al., 2024) or intrinsic changes in the disk's ionizing luminosity (Netzer, 2025) on the lags.

Based on the variations in mean obscuring column density $\bar{N}_{\rm H}$ across the three epochs, Lewin et al. (2024) proposed a scenario to explain the lag variations that connects changes in lag to time-varying obscuration between the BLR and the ionizing continuum source. In this model, the optical light curves contain two components: a disk reprocessing component producing short lags, and a diffuse continuum component from the BLR giving longer lags. Periods of low $N_{\rm H}$ (i.e., Epoch 2 of the STORM 2 campaign) correspond to times when an episodic, clumpy disk wind has just launched from the disk surface and has not yet intersected the

observer's line of sight to the X-ray emitting region. The clumpy wind partially shields the BLR from the ionizing continuum, reducing the strength of the BLR continuum contribution so that the overall continuum lags are similar to those of the disk reprocessing component alone. As the clumpy wind rises further above the disk surface, it intercepts our line of sight toward the AGN central engine, resulting in elevated $N_{\rm H}$, as seen during epochs 1 and 3. During this phase the larger scale height of the clumpy wind lifts the shielding of the BLR from the ionizing continuum, and the fully illuminated BLR then produces a strong diffuse continuum signal resulting in longer lags overall. This model is broadly similar to the scenario proposed by Homayouni et al. (2024) to explain temporal changes in the C IV emission-line lag over the duration of the campaign.

Photoionization modeling carried out by Netzer et al. (2024) considered the line and continuum emission from the BLR and additionally from rising wind itself. They demonstrated that the shortened lags during epoch 2 can be matched by models incorporating a combination of emission from the wind and the partly obscured BLR, plus a contribution of thermal dust emission originating from the inner torus that contributes to the i and z bands (e.g., Hönig, 2014). However, in contrast with the results of Lewin et al. (2024), we find nearly identical lags for Epochs 2 and 3, for all three measurement methods, despite the strong increase in $N_{\rm H}$ during Epoch 3. Thus our results appear to disfavor the changing-obscuration model as the primary explanation for the variations in lag across the three epochs.

Recently, Netzer (2025) (N25) presented a different approach to explain the time-variable lags seen in the STORM 2 campaign and their relationship to the observed changes in $N_{\rm H}$. Netzer et al. (2024) and N25 used HST spectra to demonstrate that the SED shape of Mrk 817 changed during the STORM 2 campaign, exhibiting "bluer-when-brighter" behavior. N25 proposed that these SED changes result from disk winds episodically depleting gas from the accretion disk and changing its emitted spectrum, as discussed earlier by Slone & Netzer (2012). Based on the X-ray observations presented by Partington et al. (2023) and Zaidouni

et al. (2024), N25 estimated the mass outflow rate of the disk wind in Mrk 817 to be ~ 0.1 $M_\odot$ yr^{-1}, a significant fraction of the accretion rate through the outer accretion disk. The lowered accretion rate at small radii ($< 100R_g$) then decreases the inner disk temperature, softening the disk's UV spectral shape and reducing the ionizing luminosity by as much as a factor of ~ 4 for the adopted disk and wind parameters. In the aftermath of a wind-launching episode, the ionizing photon flux incident on the BLR would then be strongly diminished, lowering the intensity of the diffuse continuum emission and reducing the observed continuum lags to values closer to the expected contribution from disk reprocessing. This mechanism operates without the need to invoke shadowing of the BLR by wind material to explain the decrease in lags from Epoch 1 to Epoch 2.

Our flux-flux analysis provides another way to examine SED changes in Mrk 817 and their connection with the continuum lags. For the full-duration campaign, and during each of the three epochs, comparison of the maximum-flux and minimum-flux SEDs as shown in Figure 4.7 clearly demonstrates a bluer-when-brighter trend across the UV and optical. Some portion of this trend at optical wavelengths must be due to the constant host galaxy contribution, but in the HST-resolved component of the host galaxy contribution is too small to affect the SED shape significantly in the UV. If we are to assume the variability is only contributed to by a disk then we would expect the flux ratio to be constant, however in 4.7 for the flux-ratios that is not shown.

Since the mean luminosity varies across the three epochs, as shown in Figure 4.10, we also compare the mean SED shapes of the three epochs to see how they relate to the changing luminosity. Figure 4.11 shows the mean SED obtained from the flux-flux fits, for the full campaign and for the three individual epochs. We also show the SEDs after subtracting off the estimated host galaxy contribution based on the Bentz et al. (2013) host-galaxy flux at 5100 Å and assuming the Bruzual & Charlot (2003) 11 Gyr model for the host spectrum, as illustrated in Figure 4.7. The lower panel of Figure 4.11 shows the ratio of the Epoch 1

SED to the SEDs from Epochs 2 and 3, when the AGN was in a fainter state on average compared with Epoch 1. These SED ratios rise toward UV wavelengths, confirming that the epoch-averaged SEDs do follow a bluer-when-brighter trend, and that the trend is intrinsic to the AGN and not just the result of host galaxy contamination at longer wavelengths.

Overall, these results are consistent with the suggestion by Netzer (2025) that changes in continuum lag across the three measurement epochs are the result of changes in the luminosity of the ionizing SED, which alter the ratio of diffuse continuum to disk emission ($L_{\rm diffuse}/L_{\rm disk}$). Since Lewin et al. (2024) measured lags that were higher in epochs 1 and 3, and lower in epoch 2, Netzer (2025) associated epochs 1 and 3 with the high-luminosity phase (corresponding to larger BLR nebular continuum contributions to the lags), and epoch 2 with the low-luminosity phase. Our results suggest a slightly different interpretation: the light curves indicate that the AGN was actually in the low state in Epoch 3, and we find lower lags in both Epochs 2 and 3 as well as a redder SED shape in comparison with epoch 1. This does not alter the conclusions of Netzer (2025), but simply clarifies that Epoch 3 (along with Epoch 2) corresponds to the lower-luminosity state with shorter lags.

Netzer (2025) identified the elevated $N_{\rm H}$ during Epoch 1 with the onset of the wind that subsequently caused the softening of the SED shape and the reduction in lags observed during Epoch 2. Our measurements show that this change in SED shape persisted through Epoch 3, during which the next period of elevated obscuration occurred. If the reappearance of elevated $N_{\rm H}$ during Epoch 3 corresponded to a new wind-launching event similar to the one that occurred during Epoch 1, then we might predict a further luminosity decrease and softening of the SED to occur at a later time, after the end of the STORM 2 monitoring period (during the extended campaign). The extended campaign data show, however, that the AGN luminosity actually increased after the STORM 2 monitoring period ended (Edelson et al., in preparation), so the possible connection between outflow events and subsequent SED changes is not entirely clear. A longer monitoring campaign could provide firmer tests for a causal

link by examining whether wind-launching events are generally followed by SED changes in the manner proposed by Netzer (2025). Fortunately, the Mrk 817 extended campaign dataset will more than double the total monitoring duration for Mrk 817, and will aid in searching for connections between luminosity, SED shape, obscuration, and reverberation lags over a longer time baseline to better understand the mechanisms underlying these temporal changes in continuum lags.

The extended campaign dataset will also make it possible to search for further episodes of anomalous behavior such as the period around THJD $\approx 9220 - 9320$. During this event, the far-UV flux was temporarily depressed in comparison with the shape of the near-UV and optical light curves, as shown in Paper IV. This decorrelation event coincided roughly with the period of elevated X-ray absorption during Epoch 1. This behavior could result from enhanced UV extinction due to a dusty outflow (e.g., Czerny et al., 2017) temporarily obscuring a portion of the accretion disk. Identifying additional events through multiwavelength monitoring will aid in understanding the mechanism underlying such changes in the UV/optical SED.

Future work to model the transfer function for these continuum light curves, using techniques such as MEMEcho (e.g., Horne et al., 2021) can help to clarify the origin of the continuum lags. The exceptional quality of the STORM 2 dataset, and the additional temporal coverage provided by the extended campaign, will make it possible to search for time-dependent and wavelength-dependent structure in the continuum transfer function corresponding to the expected contributions of disk, BLR, and dust torus emission, giving a more comprehensive view of the reprocessing geometry in Mrk 817.

4.8 Conclusions

We have presented the measurements and results for the STORM 2 ground-based photometric campaign of Mrk 817. The primary data products of this work are the intercalibrated light curves in the BV and *ugriz* bands incorporating data from 12 telescopes. In combination with light curves measured from HST and Swift observations, this is among the best-quality high-cadence continuum monitoring datasets obtained to date for any AGN. We have measured time delays using PyCCF, JAVELIN and PyROA relative to the Swift UVW2 (1928 Å) light curve. Our primary conclusions are as follows.

- The lags increase with wavelength up to a maximum of ~ 8 days for the z band. The lag spectrum exhibits a typical "disk size discrepancy" in which the lags are $\sim 2.7-4.9$ times longer than basic disk reprocessing predictions, similar to results for several other AGN in earlier literature. The PyCCF measurements for the full campaign duration show an excess lag in the U and u bands, likely due to Balmer continuum variability, but this feature is weak or absent in the JAVELIN and PyROA measurements, and in the PyCCF epoch-based measurements it only appears during the third epoch.

- Dividing the 14-month campaign into three epochs following the earlier work of Lewin et al. (2024), we find a large drop in reverberation lags from Epoch 1 to Epoch 2, corresponding to a factor of $\sim$2 decrease in the normalization τ_0 of the lag spectrum. This change in lag accompanies a decrease in both UV luminosity and mean obscuration ($\bar{N}_{\rm H}$) from Epoch 1 to Epoch 2. The lags during the third epoch are consistent with those during epoch 2 although the mean obscuring column density during Epoch 3 returned to nearly the same elevated value that it reached in Epoch 1. Thus, our results do not indicate as direct of a connection between lag and $\bar{N}_{\rm H}$ as was found by Lewin et al. (2024).

- We carried out a flux-flux analysis (Figure 4.6), finding changes in the derived shape of the variable and constant-component SEDs in different epochs of the campaign (Figure 4.7). The constant component derived from the flux-flux technique is typically presumed to represent the contribution of host galaxy starlight to the SED, but we show that its flux changes across the three measurement epochs, and that the host galaxy accounts for only a small fraction of the flux in this component. These results show that the constant component must be dominated by constant or slowly varying contributions of AGN light rather than host-galaxy starlight. The flux-flux results also show that the SED exhibits bluer-when-brighter behavior, consistent with earlier findings based on HST spectroscopic observations (Netzer et al., 2024; Netzer, 2025).

- We fit the data with the bowl-shaped disk reprocessing model of Starkey et al. (2022). While this model can roughly reproduce the shape of the lag spectrum and the variable SED shape inferred from the flux-flux analysis, the model strains to fit the long-wavelength SED in detail, and the fit requires a rather extreme and sudden change in the thickness of the outer disk rather than a smooth variation of disk thickness with radius. These issues can be further examined in future work by combining the bowl reprocessing model with additional contributions of variable continuum emission from the BLR and dusty torus.

- The observed changes in continuum lag during the campaign appear to track a decrease in luminosity and softening of the SED between Epoch 1 and 2. These changes are compatible with the model presented by Netzer (2025), in which the onset of a disk wind lowers the accretion rate through the inner region of the accretion disk and reduces the disk's ionizing photon luminosity. The luminosity of the nebular continuum and broad emission lines drop in response to this change in ionizing luminosity, reducing the broad-band lags overall. However, the available evidence does not definitively show that the disk wind observed during Epoch 1 is responsible for the later changes in the

SED and the continuum lags. Conclusive evidence for a causal link would require more such events to be detected in future monitoring of Mrk 817 and/or other AGN.

Future work on continuum reverberation in Mrk 817 will make use of data from the extended campaign. This program obtained Swift and ground-based monitoring for an additional two years after the end of the STORM 2 HST observing program, supported by additional HST COS UV spectroscopy and X-ray observations at a lower cadence. The combined 3.2-year dataset will be unprecedented in terms of monitoring duration and cadence. This will enable more detailed investigations of topics studied in the STORM 2 campaign including frequency-resolved lag behavior (Lewin et al., 2024), disk temperature fluctuations (Neustadt et al., 2024), and temporal variations in continuum lag and their relationship to changes in AGN luminosity, SED shape, and disk winds.

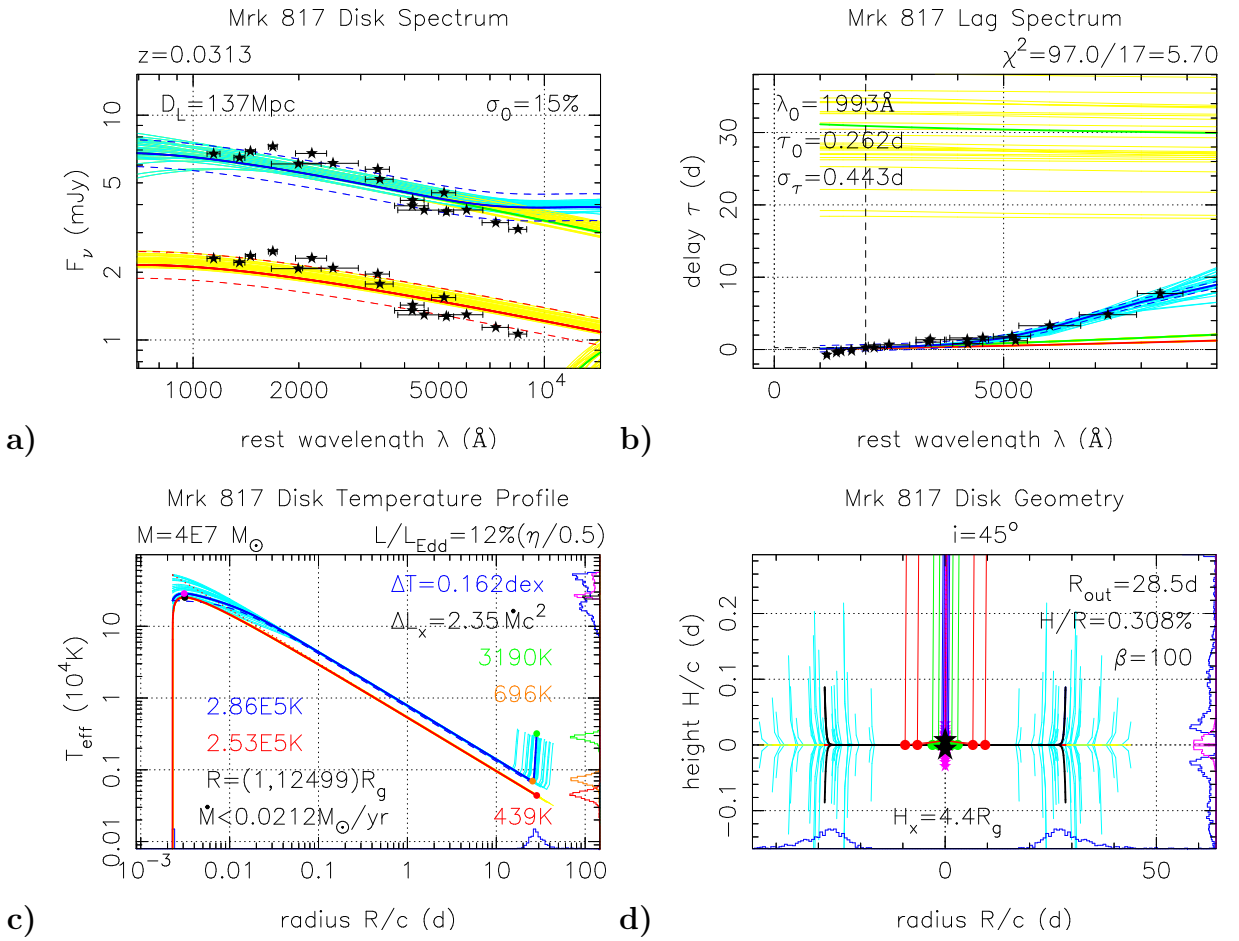

Figure 4.9: Results of fitting the Bowl model simultaneously to the full-campaign faint and bright AGN disc SEDs (top left) and the PyROA lags (top right). The disk geometry (lower right) has a steep outer rim, resulting in the temperature profile (lower left) falling as $T \propto R^{-3/4}$ and then rising on the outer rim. Red and blue curves correspond to the faint and bright state of the irradiated disk. Green curves in the top panels show the SED and lag spectrum separately for the disk inside and rim outside the minimum temperature. A random selection of 30 MCMC samples (yellow and cyan) indicate uncertainties. Median parameters from 10^4 MCMC samples are indicated on the plots. In the lower panels, histograms on the edges of the plot windows show posterior distributions of fiducial temperatures, radii, and heights.

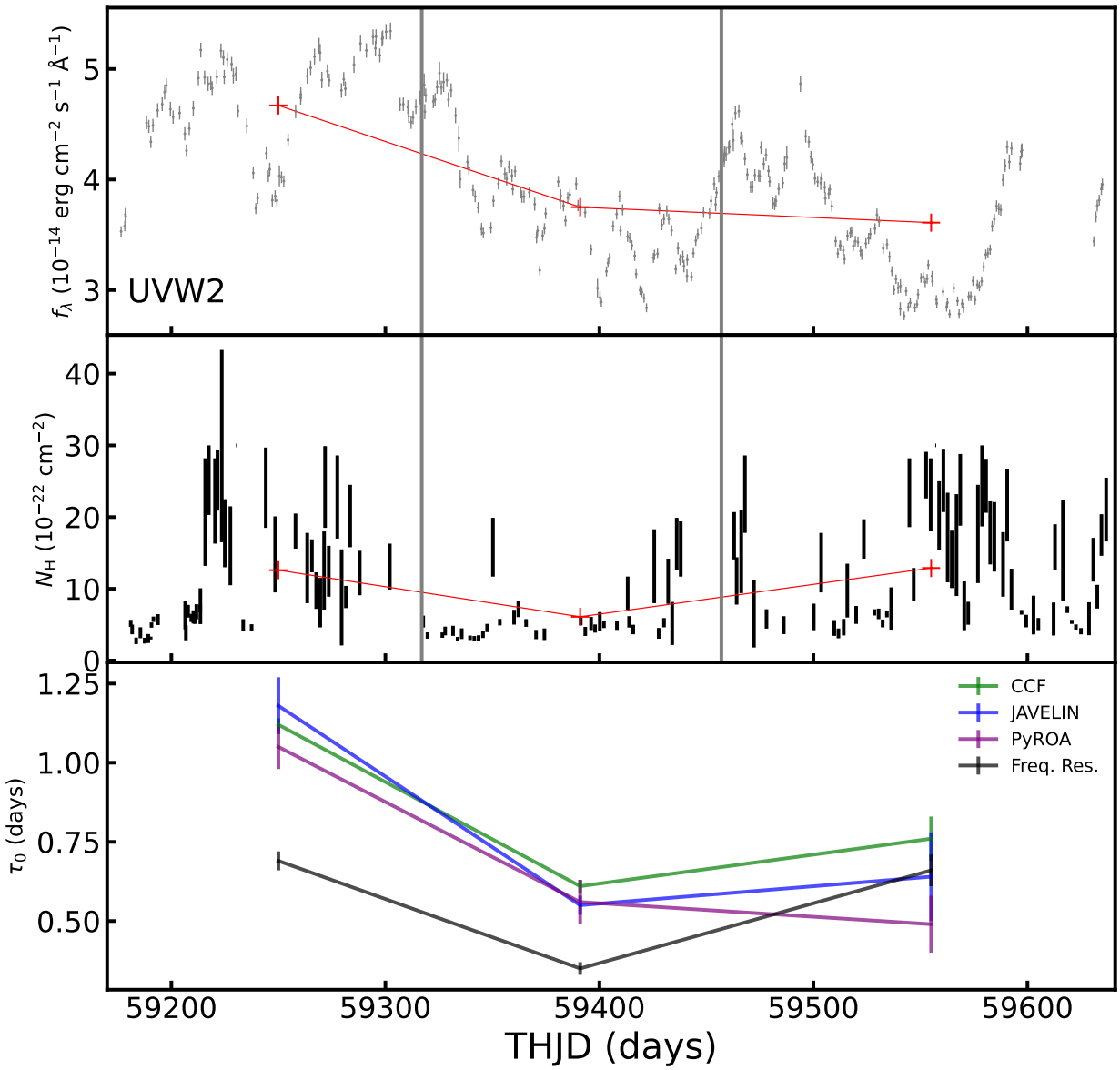

Figure 4.10: The Swift UVW2 light curve (top), X-ray absorbing column density $N_{\rm H}$ from Partington et al. (2023) (middle), and lag spectrum normalization factor τ_0 for each of the three epochs during the campaign (bottom). In the upper and middle panels, red points show the mean values of UVW2 flux and $N_{\rm H}$ for each epoch. In the lower panel, in addition to the τ_0 values measured in this work, we also show the τ_0 values from the frequency-resolved lag analysis of Paper VII (Lewin et al., 2024), for the frequency range 0.014-0.048 day^{-1}.

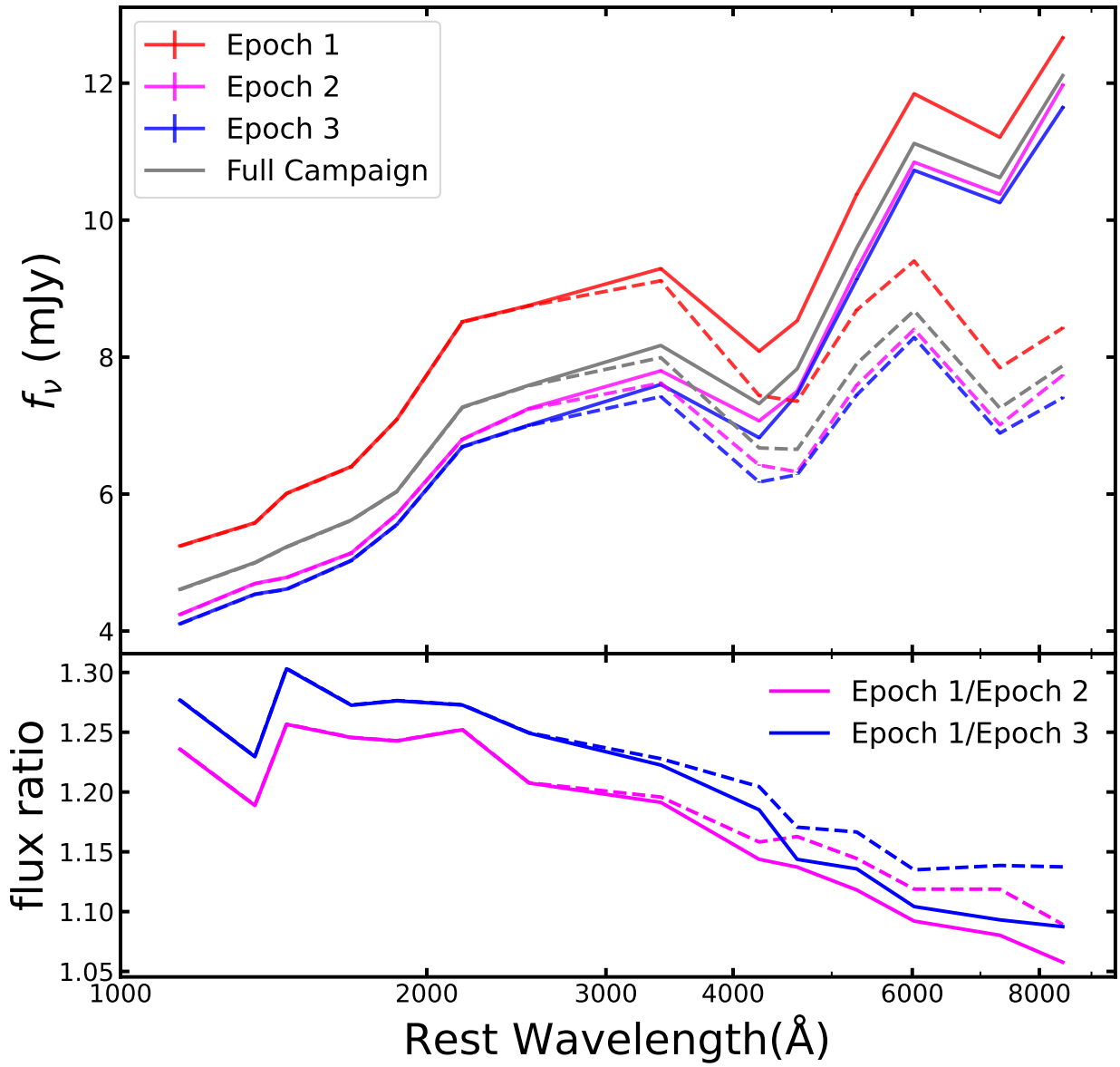

Figure 4.11: *Upper panel:* Mean SEDs from the flux-flux analysis for the three epochs. Solid curves show the mean SED of each epoch, and dashed curves show the SED after subtraction of the old stellar population host-galaxy model as illustrated in Figure 4.7. *Lower panel:* The ratio of the epoch 1 SED to the SEDs of epochs 2 and 3. Solid and dashed curves represent the SED ratios obtained before and after subtraction of the host-galaxy model. The overall slopes of the flux-ratio curves demonstrate that the mean SED has the bluest shape during epoch 1, corresponding to the epoch of highest luminosity. In both panels we show an average of the Swift U and ground-based u-band SED points in each curve rather than plotting the ground and space-based points separately, and the same is done for the B and V bands.

Chapter 5

Continuum Reverberation Mapping of Mrk 335 and PG 1302-102

5.1 The State of Reverberation Mapping

With a photometry pipeline for reverberation mapping, collaboration is possible and even requested at times. This chapter will focus on those efforts of collaborative efforts that produced co-authored works where I contributed through light curve production, which was then used for time lag measurements. The time lag measurements shown in these works are done with the same or similar methods outlined in previous chapters. This chapter will go over the successful and published projects. There are objects that do have preliminary light curves created by me but will not be included in this work due to failed observing campaigns, or lack of improvement from other methods. The objects include: Ark 120, IRC 4329A, Mrk 1239, and 3C 273.

Reverberation mapping is a rapidly developing field as the advancements in remote and automated observing have become more accessible. A highly relevant organization is the

Las Cumbres Global Observatory Network (LCOGT) which has observatories or partnerships that allow for observing in nearly every continent. With access to networks such as LCOGT, continuum reverberation mapping is highly feasible. Surveys are also to be included in this effort, i.e., the SDSS-RM project with less intensive observing or the Zwicky Transient Facility (ZTF). Regardless of the network/method used, a large number of objects have had BLR RM and/or disk continuum RM performed. Notable objects for continuum RM include: NGC 5548, NGC 4395, NGC 4593, NGC 4151, Mrk 335, Mrk 509, Mrk 142, Mrk 817, Mrk 110, Fairall 9, and more objects are consistently being published (Fausnaugh et al., 2016; Montano et al., 2022; Cackett et al., 2018; Edelson et al., 2017; Kara et al., 2023; Edelson et al., 2019; Kara et al., 2021; Hernández Santisteban et al., 2020; Cackett et al., 2020b; Vincentelli et al., 2021). For BLR RM, the list is even longer: over 100 objects have been "mapped". BLR RM has been so successful that databases are now available with mass estimates of the objects gained from Hβ time lags (Bentz & Katz, 2015).[1]

The following sections will focus on two individual objects, Markarian 335, and PG 1302. My contribution to these projects was in the light curve production and delivery for use of lag-measurements.

5.2 Mrk 335

5.2.1 Introduction

The multi-wavelength aspect of reverberation mapping is critical to understanding the processes of the inner AGN. For Markarian 335, a Narrow-line Seyfert 1 galaxy ($z = 0.025785$), which historically has had reverberation mapping projects previously performed this project is the first disk continuum RM project for it and adds to the handful of objects that have

[1] `http://www.astro.gsu.edu/AGNmass/`

had continuum RM completed. This project was a 100-day high cadence observing campaign that includes the use of the Neil Gehrels Swift Observatory, the Neutron Star Interior Composition ExploreR (NICER) and multiple ground-based observatories to cover the X-ray, UV and optical.

Key results of this project include measuring UV to optical time lags that display the semi-ubiquitous disk discrepancy issue on the order of $6-11$ times larger disk size than expected from a thin disk model and a low correlation of the X-ray to optical with a dramatic increase in flux in the optical that was followed by the X-ray. The disk size discrepancy scaling is one of the largest reported yet. Explanations given are possibly due to an increase in the AGN's mass accretion rate, however this is opposite to the expected lamp-post reprocessing picture that one initially assigns to continuum RM. Alternative explanations will be explored in the later subsections. Plots reproduced in the following sections are done so with the permission of the author, see Kara et al. (2023) for the publication.

5.2.2 Data - Contributions

The imaging data described here will primarily focus on the ground-based facilities as that is what I worked on, however the project as a whole required space based facilities such as Swift, NICER, and XMM-Newton. Swift observed with its UV filters using a $5''$ aperture and in the X-ray. NICER covered the X-ray similar to Swift however due to the incredibly low X-ray state Mrk 335 was in only the soft X-ray band was used. XMM-Newton provided a high resolution X-ray spectrum near the end of the observing campaign.

The ground-based optical imaging observations were obtained through multiple facilities. These facilities include the Las Cumbres Observatory network, the 2.0 m Liverpool Telescope, the San Pedro Martir (SPM) Observatory with the 1.5 m telescope, the 18 inch telescope at

the Wise Observatory and the 20 inch telescope at the Zowada Observatory (Brown et al., 2013a; Steele et al., 2004; Butler et al., 2012; Brosch et al., 2008; Carr et al., 2022).

All telescopes imaged in the *griz* filters with the exception of the SPM that did not have z imaging. The z light curve is a combination of the PanSTARRS z_s and SDSS z' filters. In previous chapters this practice is done and has no significant effect on lag measurements or light curves. Imaging in the u' and Johnson BV bands was taken, however the data quality from the u' filter was poor while the BV filters lacked comparable time coverage to the other *griz* filters.

Photometry was performed as outlined in Chapter 2 with a $5''$ aperture for the objective photometry and an annulus ring of $15''-20''$ to estimate the sky background. The light curves were then flux-calibrated using the seven comparison stars' magnitudes from the APASS catalog (Henden et al., 2018) to convert them to flux-wavelength cgs units. The imaging provided had multiple observations per night and were weight-averaged per telescope so each night has one data point. The last step was to intercalibrate the light curves with PyCALI, this work was published before I had implemented the uncertainty expansion method that was outlined in chapter 2. Any expansion on the uncertainties was done through PyCALI's default settings.

The light curves as seen in Figure 5.1 from Kara et al. (2023) display the full multi-wavelength effort of the project, while the right-side panels show the cross-correlation function (CCF) results. My contributions to this project are the *griz* light curve panels. Also shown in Figure 5.1 are the Swift space telescope light curves in the UV and X-ray, and the NICER space telescope (aboard the International Space Station) soft X-ray light curve. The light curves are available for public access as machine-readable tables which may be accessed through the publication site (see Table 2 of Kara et al. (2023)). Ground-based observing began before the Swift observing campaign and after however they are not shown in their entirety in Figure 5.1.

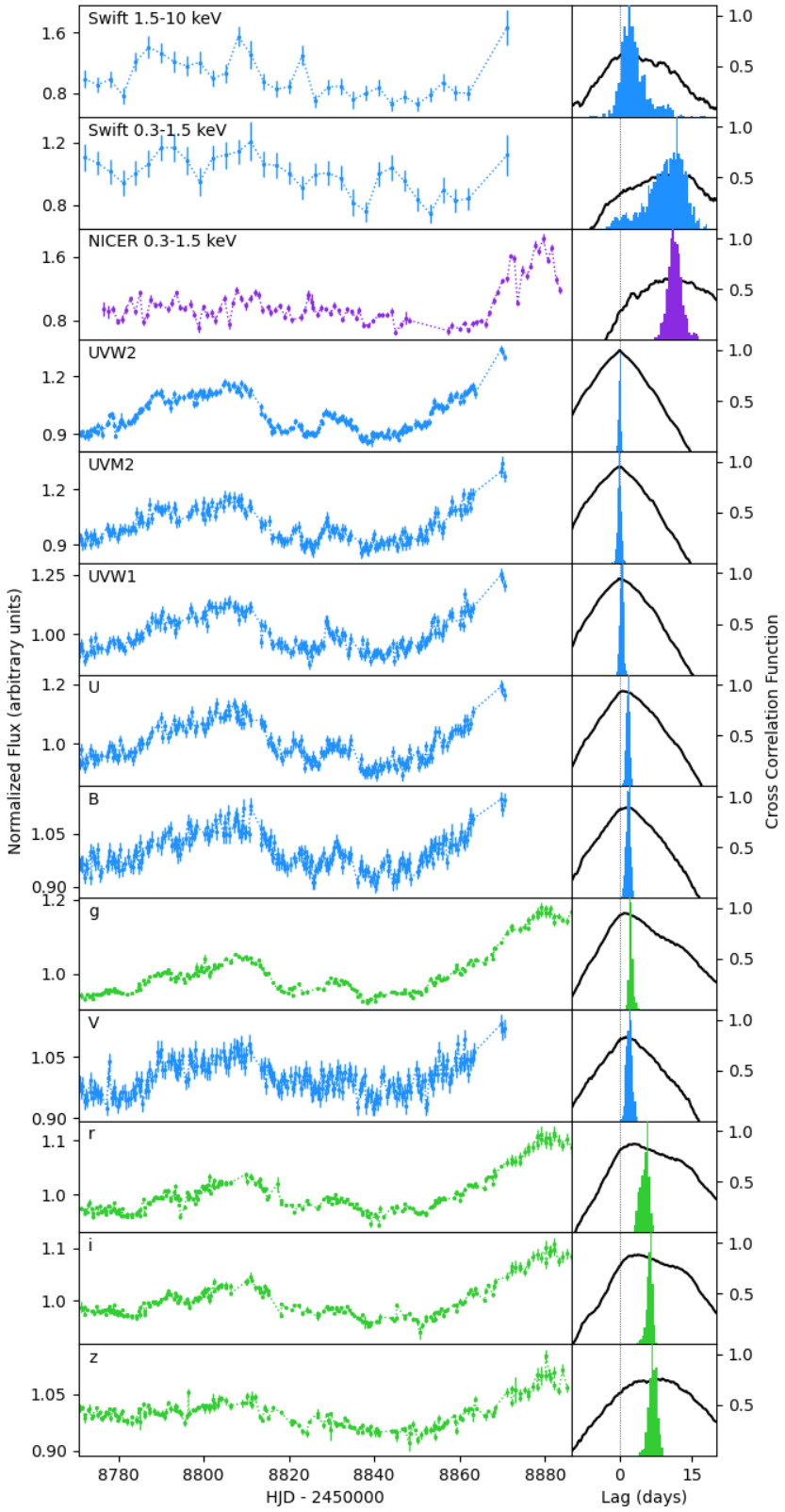

Figure 5.1: Full 100-day campaign light curves for Mrk 335 spanning the X-ray, UV and optical wavelengths. Ground-based optical wavelengths included were generated from previously mentioned photometry pipeline of chapter 2. The blue light curves represent the Swift filter-bands, green represent the ground-based facilities, and purple the NICER soft X-ray band. This figure is posted with permission from the author Dr. Erin Kara.

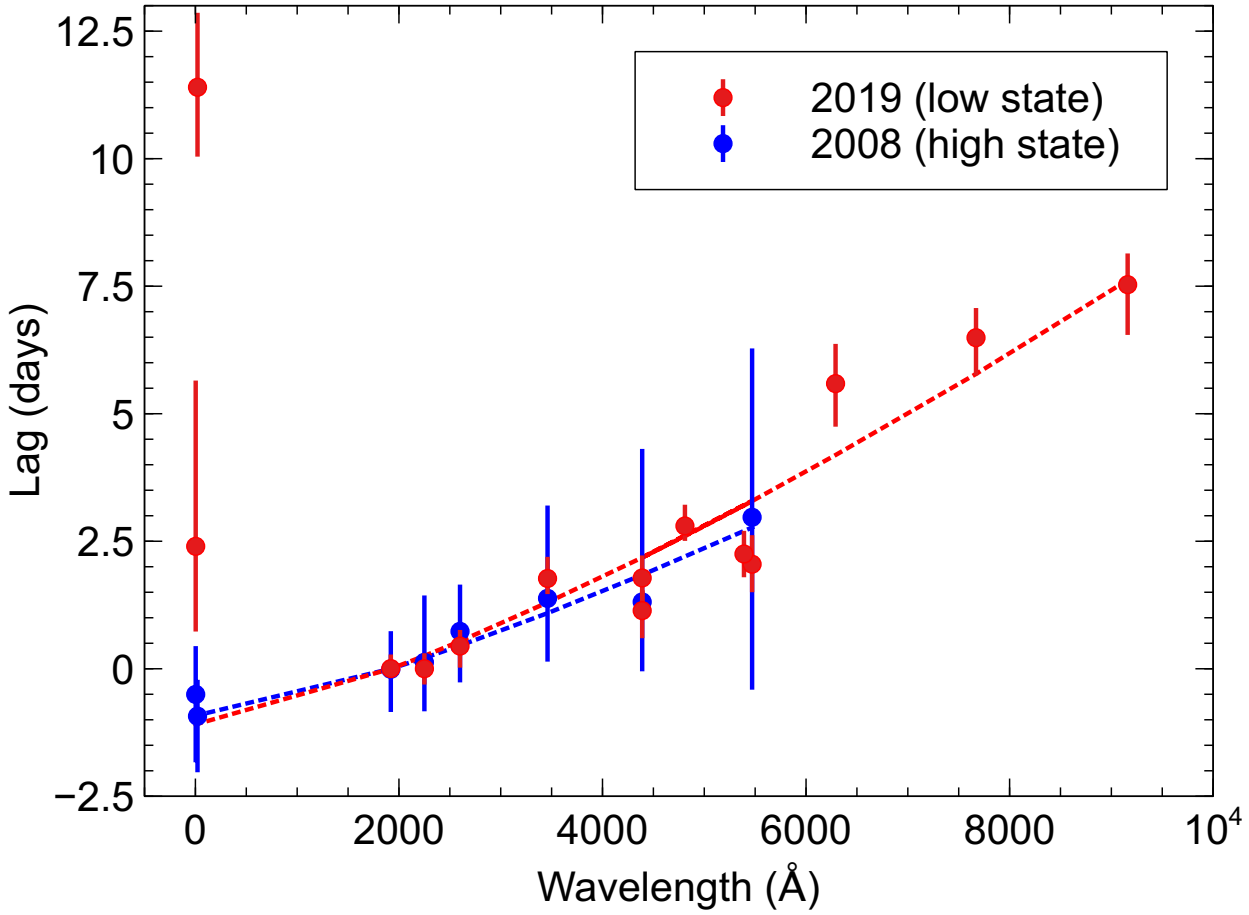

Figure 5.2: Lag spectrum of Mrk 355 measured using the ICCF method comparing previously recorded lag-spectrum. The ten-year difference in measurements while lacking the longer optical wavelengths show little change in the overall fit of a $\tau \propto \lambda^{4/3}$ curve. The notable difference is in the X-ray lags for the two states of X-ray activity, however the recent lags do not agree with power law fit or the lamp-post reprocessing picture. This figure is posted with permission from the author Dr. Erin Kara.

5.2.3 IDRM of Mrk 335

The lag measurements done for this project are done with PyCCF, the standard first method of lag measuring for many RM projects. Currently there are only a large handful of AGN that have intensive disk reverberation mapping, where a multi-wavelength effort is carried out to measure continuum lags. The more wavelength coverage and higher cadence IDRM projects reach the better we are able to discern what is happening in the less than centi-parsec (corona+accretion disk+BLR) region of the AGN. Mrk 335 is a well-studied AGN with a historically large amount of X-ray activity making it an interesting candidate for IDRM as one of the major issues with current RM paradigm is the lack of strong correlation between the observed X-rays to the UV or optical. This issue is still seen, for example in Figure 5.2 where a lag-spectrum from archival data are compared to those of this study. The overall UV-optical lags fit the power-law well, but the X-rays depart from that trend. The low and high state are for the X-ray states, but even with differing X-ray states the UV-optical lags stay consistent almost a decade later. This work by Kara et al. (2023) does highlight our current limitations in measurements, the greatest being in the X-ray domain, however that may be more to do with the restriction of X-ray observations only covering a certain line of sight. As for the X-ray lag shown shown in Figure 5.2, that is driven by the X-ray flare at the end of the campaign which was determined by exclusion of the flare from the light curves resulting in low-confidence (low correlation) lag measurements.

To recount some key points of this project are: The UV-optical lags are consistent with that of a thin accretion disk model with extended lags longer than any other IDRM object so far, despite the extended lags the "BLR contamination" in the expected bands $u-$ and $r-$ are not excessive in comparison to other AGN, there is no clear correlation between the X-ray and UV-optical despite there being a flare at the end of the 100-day campaign, the flare first showed up in the UV-optical rather than the X-ray opposite to the lamp-post picture

which may indicate accretion disk instability fluctuations propagating inward or an extended coronal height.

The work on Mrk 335 was furthered by a frequency-resolved analysis, a powerful tool that takes advantage of the high-cadence observations (Lewin et al., 2023). The lag-measurement tools like ICCF, and JAVELIN do not take into account time scales which is imperative to understand the processes happening on short timescales. There are methods to remove longer time scales processes via linear or higher-order subtraction of the light curves, this method is referred to as de-trending and while worth trying out comes with its own issues when high-order detrending is applied (Welsh, 1999). With a frequency-resolved analysis the different time scale processes are preserved and can be separated based on Gaussian-process (GP) modeling. The results of this are surprising as the frequency-resolved method clearly shows for shorter frequency bins the lags fit incredibly closely to a thin disk model. The longer frequency bins then depart from the thin disk fit as the bin would align with longer time scale processes such as diffuse continuum emission from the broad-line region.

5.3 PG 1302-102

PG 1302-102 is a quasar ($z = 0.2784$) binary black hole candidate which is a departure from my usual study of Seyfert 1 AGNs. Regardless of the higher than usual redshift this object was still chosen for reverberation mapping, because of the binary candidacy. Discussion will be focused on the results from Liu et al. (2024) and of my contribution to the project.

5.3.1 Black Hole Binaries and Reverberation Mapping

Black hole binaries (BHB) are non-standard in the reverberation mapping field, however the general technique of RM may be applied to it. BHB's are two black holes in a paired

orbit, one is typically larger than the other (the primary) while the secondary is smaller with varying mass ratios, for the case of PG 1302-102 it is implied to have a mass ratio of $q \approx 0.1$. PG 1302-102 has a high mass estimate of $10^{9.4}$ which is high on the super massive BH regime, the smaller of the duo should then have a mass of $\approx 10^9$ (Graham et al., 2015). For reverberation mappings application towards BHB's it is assumed that secondary BH has a much higher accretion rate than the primary. The higher accretion rate translate to the secondary having an accretion disk and that the primary produces negligible contributions to the overall emission. The secondary in this case is referred to as a mini-disk, and since continuum RM works on accretion disks the proposed scenario of the binary could be tested via lag-measurements. Assuming a size of the mini-disk then would allow one to estimate what a lag should come out.

5.3.2 Data - Contributions

Rick Edelson, a member of the STORM 2 team, asked about running my photometry program for PG 1302-102 due to noticed inconsistencies with Swift UBV light curves in comparison the LCO uBV light curves. This does seem to be an issue overall in reverberation mapping when comparing lag-measurements between space and ground-based facilities. In chapter 4 this is briefly touched upon, where all the Swift overlapping bands (UBV) are lower (not over 1σ though) than the ground-based lags for all methods used, however the amount they differ shows no pattern or clear reason to where the discrepancy comes from.

The light curves I created are in Figure 5.3 and in the end were not used in the publication cited earlier. Instead it was used to insure the fidelity of the light curves intercalibrated by PyROA. PyROA has a number of features, the main function being to measure time lags, but among the other functions is intercalibration. We found that the intercalibrations are within agreement and that the light curves suffer due to the weak variability of the AGN

during the observations. Further comparisons were made by measuring time lags through ICCF and the results showed slight improvement in some areas, but no overall. The largest failure of this case was the u filter, which is not shown in Figure 5.3 as it had a large excess amount of scatter that did not improve even when using more comparison stars.

For the light curve production I applied the same methods and routines for other objects such as Mrk 335, and Mrk 817. There are a few differences from other light curves produced within this body of work. Firstly the number of comparison stars used, only 1 was used, similar to the NGC 4395 work in Chapter 3. Testing was done with more comparison stars later on, however the light curves were not improved with this addition. The second difference is the intercalibration where PyCALI was run twice, first to create a damped random walk model to use for outlier rejection. At that time the uncertainty adjustment was not yet fully implemented into my routines. The full light curves shown in Figure 5.3 show twelve LCO one meter telescopes intercalibrated for the seven optical filter bands $uBVgriz$. Like previous projects the $ugri$ filters are SDSS, with a single Pan-STARRS z and Johnson B,V filters. The observations were a part of an LCO key-project that ran for multiple years however the data shown here is from the second observing period that aligned with Swift space telescope observations (not shown here).

5.3.3 Lag-Measurements and Disk Estimates

The measurements discussed here will a be short summarization of the results from Liu et al. (2024). For the methods of ICCF and PyROA the lags were shown to increase with wavelength with the optical bands showing higher fidelity to a $\lambda^{4/3}$ fit. The estimated disk size best-fits a Wien's law scenario (a blackbody) in comparison to a flux-weighted or mini-disk scenario. Both the flux-weighted and mini-disk theoretical estimates are well below the measured τ_0 value. These results then suggest that the mini-disk scenario cannot be

confirmed. PG 1302-102 has a high BH mass estimate range spanning near a magnitude $M_{\rm BH} = 10^{8.3}\,M_{\odot}$ to $10^{9.4}\,M_{\odot}$ which may contribute to the inability to confirm the mini-disk scenario coupled with disk-sizes being overestimated repeatedly in studies. Another plausible scenario is that a thin accretion disk may not be applicable in this situation and a different model of accretion disk would be needed.

5.4 Conclusion

The continuum reverberation mapping of Mrk 335 and PG 1302-102 demonstrates the range of reverberation mappings application and the photometry pipeline. For Mrk 335 continuum RM has added a valuable study to the handful of local AGN that have complete multi-wavelength high-cadence mapping completed. The results of the project opens up avenues for more studies on the lag-measurements as was shown with the continuation of the project in Lewin et al. (2023). PG 1302-102 is an interesting case to use RM on, while quasar RM is not uncommon at all the use to attempt to prove binary candidacy is. These use cases of RM are critical in helping the RM community understand the strength and versatility of RM. A strong community effort is made to share the results and light curves of these studies. For each project presented in this dissertation the light curves are available for access to the public through the publishing sites. This effort has been historically done in reverberation mapping and many archival data sets exist largely untouched/unused. For example the Las Cumbres network has their own archive with images open to public accesss, and the Zwicky Transient Facility continually deliver new data releases for free. The field of RM is continuing to grow and the data available is abundant. The largest challenge for scientist now is primarily attaining funding and students to take on these projects.

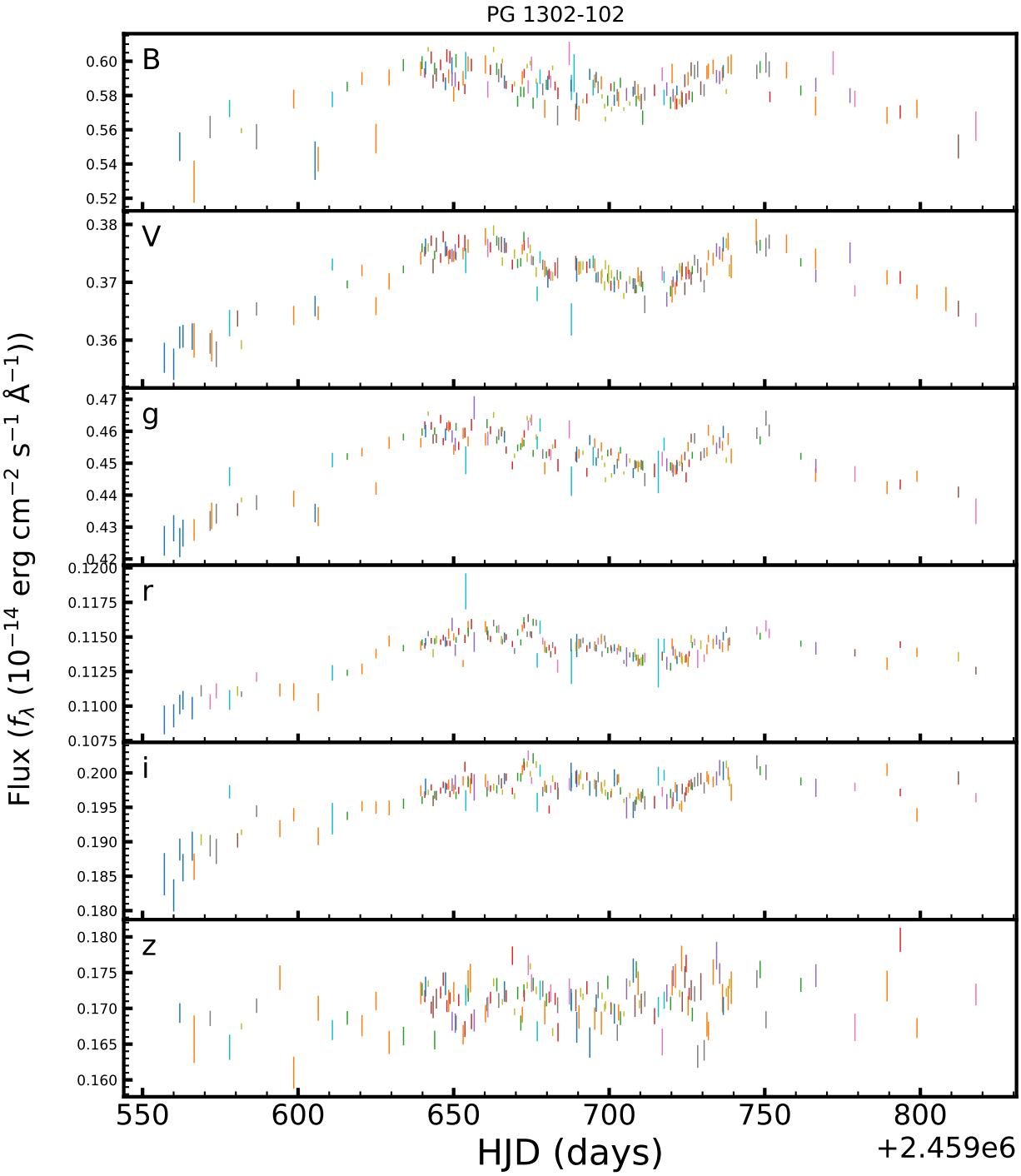

Figure 5.3: PG 1302-102 light curves for the full duration, multiple telescopes are shown as different colors. All telescopes imaging are from the Las Cumbres Observatory Global Network.

Chapter 6

Mrk 817 Extended Campaign

6.1 Introduction

As the STORM 2 campaign on Mrk 817 completed, it was continued in an extended campaign with observations from the Swift space telescope and ground-based observations. The ground-based observations were extended for approximately 2 more years and this chapter will outline the work that has gone into the reduction of those observations to create the longest high cadence light curves of an AGN so far. In the future, this extension should lead to a work similar to that of Chapter 4 with complete lag measurements, flux-flux analysis and through other researchers, a frequency-resolved analysis. This chapter will focus on the ground-based optical extended campaign, there are extensions to other wavelength regimes such as X-ray observations with NICER, UV spectroscopic observations with HST, and a Swift observing campaign covering the UV and X-ray.

Figure 6.1: Markarian 817 is located in the constellation Draco approximately 430 million light years away from us. This is a color rendition of HST WFC filters F438W (B), F555W (V), F680N (H-alpha + [N II]), and F814W (I). Image credit belongs to NASA, ESA, and the Hubble SM4 ERO team. `https://science.nasa.gov/asset/hubble/markarian-817/`

6.2 Data and Reduction

The images used for the extended campaign are primarily from LCO following the end of the STORM 2 campaign. The extended campaign contains ∼2 more years of observing right after the end of the STORM 2 campaign and follows the same cadence (in the LCO network). The Dan Zowada Memorial Observatory also continued in the extended observations of Mrk 817 and has delivered data for right after the STORM 2 campaign ended, which finished observing in May 2024. Other observations will be included in a later publication that will also include Swift Space Telescope observations to cover the far-UV.

Images are taken from the LCO archival website [1] from the key project titled "From Disc to Dust: Intensive Broadband Reverberation Mapping of Nearby Active Galactic Nuclei" submitted by Juan Hernandez Santisteban and found in the archive as KEY2023-001. Imaging is taken with the 1 meter telescope network with $BVugriz$ filters. Additionally, multiple batches of Zowada data has been delivered for the $griz$ filters.

The photometric process is the same as outlined in Chapter 4. That includes using a 5″ objective aperture and a 10″ to 15″ annulus ring for sky-background estimation. We maintain the same comparison stars used in Chapter 4 from the STORM 2 campaign. Normalization is performed for the full data set with no noticeable deviations from the STORM 2 campaign. The Zowada data in comparison to the LCO data has a lower overall S/N. The later half of the extended Zowada data suffers from worse data quality and is present in the normalization process. If the data is not satisfactory enough to provide reliable measurements then it will be taken out through outlier rejection due to low S/N. The rejection effects are noticeable in the i and z which are traditionally noisier.

Flux calibration is applied with the same magnitudes from STORM 2 and data points are then weight-averaged to combine observations taken the same night per telescope. The

[1] `archive.lco.global`

intercalibration process is the same as done for the STORM 2 project, with the small change of MCMC iterations increased to 15000 from 10000. An important note of difference with the intercalibration process is that the shifting and scaling factors that best-fit for the original STORM 2 campaign will be different for the extended campaign. This happens, because we have more than double the data to intercalibrate and the variability of Mrk 817 so far has been strong over the time of the extended campaign.

Previously in Chapter 4 the intercalibration process[2] with pyCALI (Li et al., 2014) was only referenced and briefly outlined. Here we will properly describe the intercalibration process for clarity. PyCALI is done with a reference light curve and the light curves are defined as $F_\lambda(\lambda) = \phi \cdot F_\lambda(\lambda) - G$, where ϕ is a multiplicative factor and G is an additive shifting factor. For the reference light curve $\phi = 1$ and $G = 0$. It is important to note this by default will not shift or scale the reference light curve at all. This explanation is also the scalar representation of the process, computationally it is done with matrix representations and transformed as $f_{obs} = \Phi^{-1}(y + G) + bn + \epsilon$, where y is a vector representing our flux measurements, n is a vector of the uncertainties/errors, ϵ are unknown/systematic errors, b is an $m \times m$ diagonal matrix for error scaling. The intercalibrated light curves are then represented as $f_{cali} = \Phi(f_{obs} + bn + \epsilon) - G$. The outputs are the intercalibrated light curves, a reconstruction model light curve using the DRW posteriors parameters, the estimated intercalibration parameters from the posterior distributions generated, and a posterior sample (DRW model parameters, shift and scale factors, error scaling factors).

Returning to the reference light curve, the best practice for disk continuum RM is a light curve with it's central wavelength closest to the lower end of the UV. In these preliminary results we are using the g band as it is the best quality light curve we have and currently do not have access to the extended Swift UVW2 light curve.

[2] `https://pycali.readthedocs.io/en/latest/`

The last step after the light curves are intercalibrated is to adjust their uncertainties by using a damped random walk (DRW) model. We use the generated DRW model from pyCALI. We generate the model twice, because the first model may come out with high-frequency structure due to it trying to fit to each point (this was stated in Chapter 2 when describing the intercalibration process and shown in Figure 2.6). The second run is performed on intercalibrated data (the first runs output), this way pyCALI does not need to strain to intercalibrate the light curves and only generates a smooth DRW model. We use the smooth DRW model to further reject outliers and adjust the uncertainties of the light curves. The uncertainty adjustment is done by a reduced χ^2 fit to the DRW model, where we expand or shrink the uncertainties to achieve a reduced $\chi^2 = 1$ **per telescope**. We adjust the uncertainties per telescope in order to conserve the structure of the higher quality light curves while also providing a robust uncertainty for light curves that do not have as high S/N.

6.3 Preliminary Lag Measurements

Time lag measurements have only been taken with PyCCF due to it having the shortest computational time. With $\sim$2 more years of data, processing time will increase greatly especially for programs like JAVELIN and PyROA. The PyCCF parameters used are: a lag range of -80 to 80 days, an interpolation time step of 0.1 days, and the number of monte carlo iterations nsim= 10000. We have increased the lag range time as PyCCF runs with the same lag range as the original STORM 2 campaign resulted in a large amount of failed iterations for the CCPD and CCCD. Additionally increasing the lag search range is necessary as the observing window of the object increases as well. A failed iteration in the distributions is based on $r_{\max} <= 0.2$ and for successful measurements the number of failed

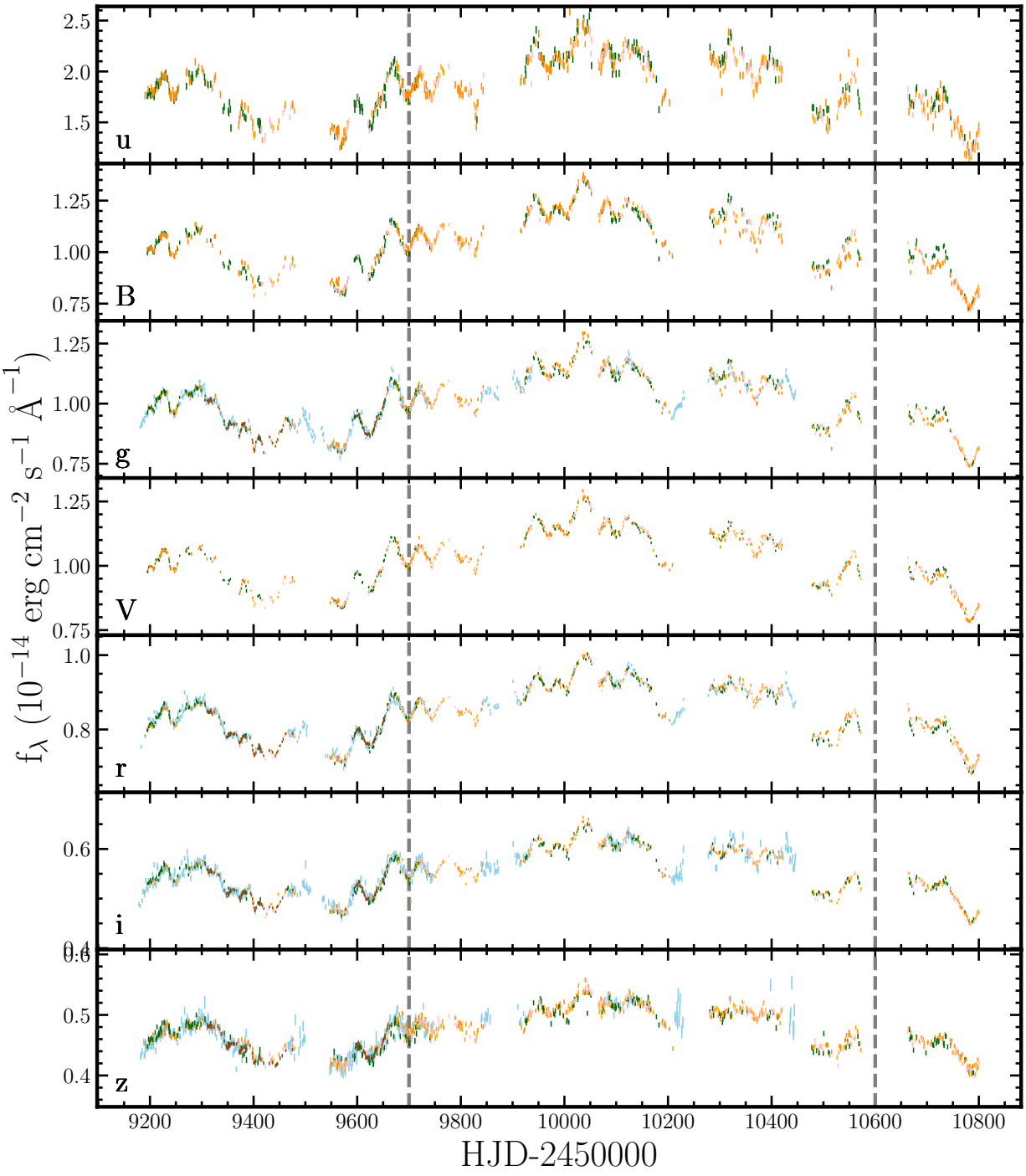

Figure 6.2: Mrk 817's extended campaign light curves presented with horizontal lines to mark the end of the STORM 2 campaign (left-most dashed line) and the end of the extended campaign (right-most dashed line). Observing of Mrk 817 is still continuing through and LCO key-project. The colors represent individual telescopes, where all but the light blue data points are from LCO. The light blue points are from Zowada imaging.

Filter	$\tau_{\rm cen}$	$r_{\rm max}$
u	$0.72^{+0.84}_{-0.84}$	0.97
B	$-0.99^{+1.37}_{-0.98}$	0.99
g	$0.00^{+0.10}_{-0.10}$	1.00
V	$-0.43^{+1.25}_{-1.00}$	0.99
r	$5.65^{+0.75}_{-0.75}$	0.98
i	$5.05^{+0.94}_{-0.99}$	0.98
z	$11.39^{+1.26}_{-1.37}$	0.94

Table 6.1: Lag-measurements for the solely the extended campaign. Lags are in the observed frame and use the g filter-band as the reference.

iterations is ~ 0. With the increased search range we accomplished 0 failed iterations for all optical filter bands.

The largest surprise out of these preliminary measurements is the increase in the z-band lag. In Figure 6.3 the lags are displayed in a lag-wavelength spectrum and are compared to the original STORM 2 campaign. It is apparent that the z-band lag is nearly doubled with only the extended campaign data. To test this result we performed PyCCF runs on large segments of the light curves, the inclusion of the STORM 2 with the extended and another that splits the extended campaign. The results of these runs showed that excluding the original campaign gives a slightly extended lag in comparison, however only using the latter half of the extended campaign results in the over double time lag. Further testing is still required to determine the reason why the lags are so overextended in the extended campaign however that will not be completed until the Swift data is available.

6.4 Discussion

The extended campaign of Mrk 817 more than doubles the amount of data while maintaining the high cadence. With a longer baseline to measure lags our measurements then are an average of the lags over this extended period. The lag-spectrum shown in Figure 6.3 displays the measured lags for the original STORM 2 campaign underneath the extended campaign

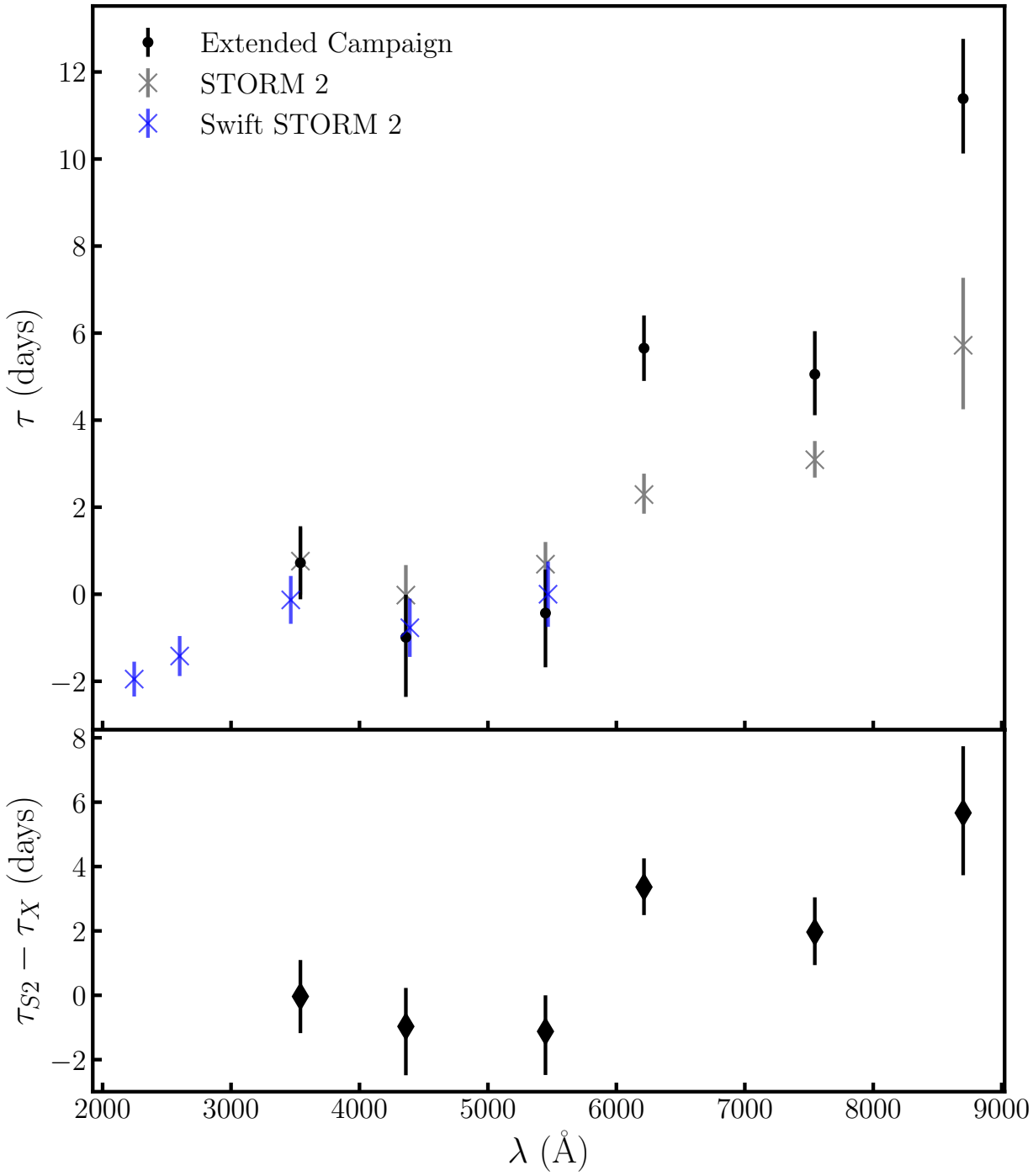

Figure 6.3: Mrk 817's lag-spectrum for the extended campaign (top) along with the original STORM2 lags. The bottom panel shows the difference between the lags of the extended and original campaign.

and there is a large difference in the longer optical wavelengths while maintaining similar lags in the shorter wavelengths. Most notable is the near zero change for the u band light curve which we may assume is the closest to the driving continuum. For the lag-measurements shown in this section the g-band light curve is being used as the "reference" light curve as it has the best quality and highest number of data points which directly affects cross-correlation measurements. An increase in the riz optical bands may indicate more dust emission, Hönig (2014) showed that dust emission like the DCE can contribute to extending lags and physically the expected response expected would be on a longer timescale. The small changes in the uBV lags however are difficult to explain. In Chapter 4 in the epoch analysis there was evidence for enhanced DCE through the u/U lags in the third epoch, but this was only present in the pyCCF lags.

These measurements are only between the ground-based filter bands. The full analysis would use the Swift UVW2 light curve as the driving light curve. JAVELIN or pyROA measurements may prove inconclusive unless the Swift UVW2 light curve is used. The correlation coefficient values $r_{\max}$ are over 0.98 for all filter-bands except the z band which has an $r_{\max}$ of 0.95.

6.5 Conclusion

Mrk 817's extended campaign has maintained a high-cadence with LCO and Zowada data. The extended campaign section of the light curves consistently rise in flux, higher than the STORM 2 light curves, and maintains that for roughly half the duration while after the completion of Swift observing the flux has decreased further than the original campaign. Currently we cannot comment on the variability in the ultraviolet wavelengths as that information is not yet available, however with the obvious visual variability being repeated in the following filter-bands would suggest the far-UV may display the same behavior. This

does not discount the possibility of there being another de-correlation event between the UV which will have a marked affect in lag measurements and flux-flux analysis.

Continued work for the extended campaign will include repeating the analysis performed in Chapter 4 for the STORM 2 campaign. That would include the addition of Swift space telescope data to produce a complete lag-spectrum of Mrk 817 for the full duration of STORM 2 and the extended campaign. The flux-flux analysis will also be repeated while constraining the light curves to the duration of the Swift light curves (as they are not as long as the ground-based light curves). An epoch-based analysis will be performed again possibly with a different set of parameters to decide what constitutes an "epoch", e.g. using spectral information from HST or X-ray data.

To continue this work in the future we suggest to take a larger collaborative publication that would include the ground-based and space-based light curves together rather than separate papers. This is with consideration that the STORM 2 publications be used as primary references for the methods used.

Chapter 7

Conclusions

7.1 Summary

The intensive multi-wavelength observing campaigns completed in this dissertation present the merit and strength of modern day reverberation mappings ability to characterize the inner-regions of AGN. Reverberation mapping has an incredible utility to many types of AGN as was shown here, from intermediate mass black holes to high-redshift quasars. The accessibility of robotic observing and the combination of multiple facilities allows researchers to conduct reverberation mapping studies to help us understand the radiative processes in AGN. Below is a short summarization of the results of the reverberation mapping projects shown in this dissertation

- NGC 4395: I generated continuum light curves in the *griz* filter-bands using the Las Cumbres Observatory Global Network and measured inter-band time lags using the g-band as the reference. The lags ranged from $7.72^{+1.01}_{-1.09}$ minutes, $14.16^{+1.22}_{-1.25}$ minutes, $20.78^{+1.94}_{-2.09}$ minutes for the riz filters using both half nights of observing. The increasing lags with wavelength fit to a $\tau \propto \lambda^{4/3}$ curve, but deviate from the standard thin disk

model displaying the common disk size discrepancy issue. In terms of reverberation mapping relations NGC 4395 provides an incredibly value data point as the nearest measurement is over two magnitudes in separation of mass. This work is one of the first reverberation mapping studies to measure inter-band continuum lags.

- Mrk 817: The ground-based optical continuum reverberation mapping for STORM 2 includes the full observing campaign that I reduced into intercalibrated light curves for the $BVugriz$ filters. Lag measurements were taken with multiple methods and with ICCF the u band lag measured 3.0 ± 0.8 days and 7.9 ± 1.5 days for z. The lags in all methods are consistent with the $\tau \propto \lambda^{4/3}$ as expected for lamp-post reprocessing, however the estimated disk sizes are between $2.7 - 4.9$ times larger than a thin disk model. Since the data quality of the light curves in this campaign was high we opted to split the campaign into three epochs following a previous STORM 2 work based on the average $N_{\rm H}$ value separating them based on a low-high-low comparison. We found that the lags vary between epoch up to a factor of 2 which agrees with the assessment of Lewin et al. (2024) and presents a challenge to our current understanding of the reprocessing picture. A flux-flux analysis is performed for the full duration light curves and epochs extending the results of Cackett et al. (2023) to include the optical light curves. The SEDs from the flux-flux results show a bluer-when-brighter trend shown through the different epochs. The brightest and bluest epoch also has the longest lags which strongly suggest that changes in the SED are driving the changes in the lags. The light curves generated from this project are the best-quality high-cadence continuum dataset produced at the time for any AGN and will accessible to other groups through the future publication.

- Mrk 335: The IDRM project led by Dr. Erin Kara (MIT) was one of the first successful collaborations outside of STORM 2 that I participated in. For this work I produced $BVugriz$ light curves, with the exclusion of the BVu in the publication due to poor

quality. This project was a short 100-day campaign, yet was still covered a wide range of wavelengths from X-ray, UV to optical. The results of this campaign showed time lags measurements being consistent with the lamp-post reprocessing power law of $\tau \propto \lambda^{4/3}$, but the disk sizes $6 - 11$ times larger than the thin disk model which is one of the largest disk size discrepancies out there. Despite multiple X-ray light curves there was a still a lack of strong correlation between the X-ray and UV. Mrk 335 was in a historically low X-ray state which showed no affect on the time-lags and when compared to lags from a decade before in a high X-ray state the lags remained relatively the same.

- PG 1302-102: The quasar reverberation mapping project by Liu et al. (2024) explored a novel application of reverberation mapping. PG-1302 is a binary black hole candidate and was tested through a mini-disk scenario that could be confirmed through reverberation mapping. I produced light curves for the optical $uBVgriz$ filters to ensure the fidelity of the data as there was a prominent difference in quality when comparing the Swift UBV light curves to the ground-based uBV. It was found that due to the low-quality of the observations further improvements could not be made. The lag-measurements were shown to be consistent with the $\tau \propto \lambda^{4/3}$ reprocessing picture, however it also displays a disk size discrepancy. The mini-disk scenario in this case failed to confirm the binary as the lags prescribed to a mini-disk were well-below the measurements and a flux-weighted response. This does not disqualify the object as a binary candidate as there are a number of issues in reverberation mapping that may occlude such a finding.

Figure 7.1: A first light image of the Vera Rubin observatory showing only a fraction of its full field of view. The observatory is set to generate an astounding amount of data on the order of terabytes per day and petabytes per catalog! Credit: NSF–DOE Vera C. Rubin Observatory. Image source.

7.2 Future Work

The ongoing effort in reverberation mapping has strong momentum and for projects like STORM 2 a lot of work is yet to be done. This section will go over concrete examples of research in progress, or to be done, and research farther in the future. The first examples of future work will be on the projects I am a part of and the latter will be projects/collaborations by other groups within the field.

- STORM 2: The STORM 2 collaboration includes multiple facilities and universities so the data reduction will be completed by the respective parties. The infrared analysis of STORM has been recently submitted and is going through revision, while the ground-based spectroscopic team is working on a pre-submission draft. Also to be submitted will be a work focusing on modeling the transfer functions of the full STORM 2 observational dataset that would include the broad-band UV/optical filters and several emission lines. Other works are continually being worked that are not officially a part of the STORM 2 publication series, but are made by members of the team. Such works include the modeling of the inter-band continuum lags through disk wind, broad-line region and continuum photo-ionization (Netzer, 2025).

- The Mrk 817 extended campaign includes over two more years of observing with ground-based facilities, Swift observatory and HST. While not all of the original facilities from STORM 2 are being implemented the preliminary results show us more changes in the optical inter-band lags. Continued work into the extended campaign will include the full suite of analysis that was performed in chapter 4 and the addition of Swift light curves to create a full lag-spectrum.

- LCO Key-projects have been a pivotal component of continuum reverberation mapping and will continue to be for the near future. This is clearly evident through the projects presented in this dissertation as every single one uses data from LCO and in each case

the LCO light curves are always the highest quality. LCO key-projects have included reverberation mapping since 2017 and has been renewed until 2026. Even if an object is not specific to the reverberation mapping key-project, it may be in the LCO archive where the data may be used for a RM project once publicly available.

- The Vera Rubin Observatory recently released first light images and showed an incredible survey field of view. Figure 7.1 shows a small fraction of the true FOV and in further analysis in these images a number of new objects have been discovered. As the range of redshift will pushed further the number of quasars to have RM will increase by the hundreds considering the Large Survery of Space Time (LSST) has its own AGN division that will do just that (Kovačević et al., 2022).

- While my work focuses on continuum reverberation mapping the efforts of quasar and BLR reverberation mapping are not to be forgotten. Primarily survey reverberation mapping provides the community with light curves from AGN with varying masses, luminosity, accretion rate and so on. Such projects have been in progress for over a decade now such as the SDSS-RM project, the ZTF survey, the Super Eddington accreting massive black holes (SEAMBH) project, or LAMP. Survey projects are continually being supported or created and provide an invaluable data set to the community. AGNs are incredibly variable, not in just their emission, but in properties so these projects are crucial to creating a unified theory of AGN.

7.3 Conclusion

The utility of reverberation mapping as a technique has evolved over the past few decades. As observational technology advanced reverberation mapping was enabled for a vast amount of objects. With the advent of broad-line region reverberation mapping mass estimates and BLR spatial extents were measurable with observing campaigns. The BLR mapping projects

had great success and now boasts over hundreds of AGN with BLR spatial measurements enough to create the relation between $R_{\rm BLR} - L_{\rm cont}$ which shows a tight correlation between the two properties. Such relations are further extended with mass estimates or continuum lag measurements. The future of the field is promising with BLR projects continuing or simply being added to continuum RM which helps characterize AGN fully. With the population of AGNs to observe growing in the next decades reverberation mapping will grow along with it and so will our understanding of active galactic nuclei.

Bibliography

Astropy Collaboration, Robitaille, T. P., Tollerud, E. J., et al. 2013, aap, 558, A33, doi: 10.1051/0004-6361/201322068

Astropy Collaboration, Price-Whelan, A. M., Sipőcz, B. M., et al. 2018a, aj, 156, 123, doi: 10.3847/1538-3881/aabc4f

—. 2018b, aj, 156, 123, doi: 10.3847/1538-3881/aabc4f

Astropy Collaboration, Price-Whelan, A. M., Lim, P. L., et al. 2022, The Astrophysical Journal, 935, 167, doi: 10.3847/1538-4357/ac7c74

Bahcall, J. N., Kozlovsky, B.-Z., & Salpeter, E. E. 1972, The Astrophysical Journal, 171, 467, doi: 10.1086/151300

Bentz, M. C., & Katz, S. 2015, The Publications of the Astronomical Society of the Pacific, 127, 67, doi: 10.1086/679601

Bentz, M. C., Walsh, J. L., Barth, A. J., et al. 2008, The Astrophysical Journal Letters, 689, L21, doi: 10.1086/595719

—. 2009, The Astrophysical Journal, 705, 199, doi: 10.1088/0004-637X/705/1/199

Bentz, M. C., Denney, K. D., Grier, C. J., et al. 2013, The Astrophysical Journal, 767, 149, doi: 10.1088/0004-637X/767/2/149

Berkley, A. J., Kazanas, D., & Ozik, J. 2000, The Astrophysical Journal, 535, 712, doi: 10.1086/308880

Bessell, M. S., Castelli, F., & Plez, B. 1998, aap, 333, 231

Blandford, R. D., & McKee, C. F. 1982, The Astrophysical Journal, 255, 419, doi: 10.1086/159843

Brosch, N., Polishook, D., Shporer, A., et al. 2008, apss, 314, 163, doi: 10.1007/s10509-008-9752-4

Brown, T. M., Baliber, N., Bianco, F. B., et al. 2013a, The Publications of the Astronomical Society of the Pacific, 125, 1031, doi: 10.1086/673168

—. 2013b, The Publications of the Astronomical Society of the Pacific, 125, 1031, doi: 10.1086/673168

Bruzual, G., & Charlot, S. 2003, mnras, 344, 1000, doi: 10.1046/j.1365-8711.2003.06897.x

Burke, C. J., Shen, Y., Chen, Y.-C., et al. 2020, The Astrophysical Journal, 899, 136, doi: 10.3847/1538-4357/aba3ce

Butler, N., Klein, C., Fox, O., et al. 2012, in Society of Photo-Optical Instrumentation Engineers (SPIE) Conference Series, Vol. 8446, Ground-based and Airborne Instrumentation for Astronomy IV, ed. I. S. McLean, S. K. Ramsay, & H. Takami, 844610, doi: 10.1117/12.926471

Cackett, E. M., Bentz, M. C., & Kara, E. 2021, iScience, 24, 102557, doi: 10.1016/j.isci.2021.102557

Cackett, E. M., Chiang, C.-Y., McHardy, I., et al. 2018, The Astrophysical Journal, 857, 53, doi: 10.3847/1538-4357/aab4f7

Cackett, E. M., Horne, K., & Winkler, H. 2007, mnras, 380, 669, doi: 10.1111/j.1365-2966.2007.12098.x

Cackett, E. M., Zoghbi, A., & Ulrich, O. 2022, The Astrophysical Journal, 925, 29, doi: 10.3847/1538-4357/ac3913

Cackett, E. M., Gelbord, J., Li, Y.-R., et al. 2020a, The Astrophysical Journal, 896, 1, doi: 10.3847/1538-4357/ab91b5

—. 2020b, The Astrophysical Journal, 896, 1, doi: 10.3847/1538-4357/ab91b5

Cackett, E. M., Gelbord, J., Barth, A. J., et al. 2023, The Astrophysical Journal, 958, 195, doi: 10.3847/1538-4357/acfdac

Cai, Z.-Y., Wang, J.-X., Zhu, F.-F., et al. 2018, The Astrophysical Journal, 855, 117, doi: 10.3847/1538-4357/aab091

Cardelli, J. A., Clayton, G. C., & Mathis, J. S. 1989, The Astrophysical Journal, 345, 245, doi: 10.1086/167900

Carr, R., Cinabro, D., Cackett, E., Moutard, D., & Carroll, R. 2022, Publications of the Astronomical Society of the Pacific, 134, 045002, doi: 10.1088/1538-3873/ac5b87

Carson, D. J., Barth, A. J., Seth, A. C., et al. 2015, aj, 149, 170, doi: 10.1088/0004-6256/149/5/170

Chelouche, D., Pozo Nuñez, F., & Kaspi, S. 2019, Nature Astronomy, 3, 251, doi: 10.1038/s41550-018-0659-x

Cho, H., Woo, J.-H., Hodges-Kluck, E., et al. 2020, The Astrophysical Journal, 892, 93, doi: 10.3847/1538-4357/ab7a98

Cho, H., Woo, J.-H., Treu, T., et al. 2021, The Astrophysical Journal, 921, 98, doi: 10.3847/1538-4357/ac1e92

Clavel, J., Reichert, G. A., Alloin, D., et al. 1991, The Astrophysical Journal, 366, 64, doi: 10.1086/169540

Collier, S., Horne, K., Wanders, I., & Peterson, B. M. 1999, mnras, 302, L24, doi: 10.1046/j.1365-8711.1999.02250.x

Collier, S. J., Horne, K., Kaspi, S., et al. 1998, The Astrophysical Journal, 500, 162, doi: 10.1086/305720

Czerny, B., Li, Y.-R., Hryniewicz, K., et al. 2017, The Astrophysical Journal, 846, 154, doi: 10.3847/1538-4357/aa8810

Czesla, S., Schröter, S., Schneider, C. P., et al. 2019, PyA: Python astronomy-related packages. http://ascl.net/1906.010

Dalla Bontà, E., Peterson, B. M., Bentz, M. C., et al. 2020, The Astrophysical Journal, 903, 112, doi: 10.3847/1538-4357/abbc1c

De Rosa, G., Peterson, B. M., Ely, J., et al. 2015a, The Astrophysical Journal, 806, 128, doi: 10.1088/0004-637X/806/1/128

—. 2015b, The Astrophysical Journal, 806, 128, doi: 10.1088/0004-637X/806/1/128

den Brok, M., Seth, A. C., Barth, A. J., et al. 2015, The Astrophysical Journal, 809, 101, doi: 10.1088/0004-637X/809/1/101

Desroches, L.-B., Filippenko, A. V., Kaspi, S., et al. 2006, The Astrophysical Journal, 650, 88, doi: 10.1086/507263

Dietrich, M., Kollatschny, W., Peterson, B. M., et al. 1993, The Astrophysical Journal, 408, 416, doi: 10.1086/172599

Donnan, F. R., Horne, K., & Hernández Santisteban, J. V. 2021, Monthly Notices of the Royal Astronomical Society, 508, 5449, doi: 10.1093/mnras/stab2832

Edelson, R., Gelbord, J. M., Horne, K., et al. 2015, The Astrophysical Journal, 806, 129, doi: 10.1088/0004-637X/806/1/129

Edelson, R., Gelbord, J. M., Horne, K., et al. 2015, The Astrophysical Journal, 806, 129, doi: 10.1088/0004-637X/806/1/129

Edelson, R., Gelbord, J., Cackett, E., et al. 2017, The Astrophysical Journal, 840, 41, doi: 10.3847/1538-4357/aa6890

—. 2019, The Astrophysical Journal, 870, 123, doi: 10.3847/1538-4357/aaf3b4

Edri, H., Rafter, S. E., Chelouche, D., Kaspi, S., & Behar, E. 2012, The Astrophysical Journal, 756, 73, doi: 10.1088/0004-637X/756/1/73

Event Horizon Telescope Collaboration, Akiyama, K., Alberdi, A., et al. 2019a, The Astrophysical Journal Letters, 875, L1, doi: 10.3847/2041-8213/ab0ec7

—. 2019b, The Astrophysical Journal Letters, 875, L4, doi: 10.3847/2041-8213/ab0e85

Fausnaugh, M. M., Denney, K. D., Barth, A. J., et al. 2016, The Astrophysical Journal, 821, 56, doi: 10.3847/0004-637X/821/1/56

Fausnaugh, M. M., Denney, K. D., Barth, A. J., et al. 2016, The Astrophysical Journal, 821, 56, doi: 10.3847/0004-637X/821/1/56

Fausnaugh, M. M., Denney, K. D., Barth, A. J., et al. 2016, The Astrophysical Journal, 821, 56, doi: 10.3847/0004-637X/821/1/56

Fausnaugh, M. M., Starkey, D. A., Horne, K., et al. 2018, The Astrophysical Journal, 854, 107, doi: 10.3847/1538-4357/aaaa2b

Filippenko, A. V., & Ho, L. C. 2003, The Astrophysical Journal Letters, 588, L13, doi: 10.1086/375361

Filippenko, A. V., & Sargent, W. L. W. 1989, The Astrophysical Journal Letters, 342, L11, doi: 10.1086/185472

Fukugita, M., Ichikawa, T., Gunn, J. E., et al. 1996, aj, 111, 1748, doi: 10.1086/117915

Gardner, E., & Done, C. 2017, mnras, 470, 3591, doi: 10.1093/mnras/stx946

Gaskell, C. M. 2024, Astronomical and Astrophysical Transactions, 34, 221, doi: 10.48550/arXiv.2501.12757

Gaskell, C. M., & Peterson, B. M. 1987a, apjs, 65, 1, doi: 10.1086/191216

—. 1987b, apjs, 65, 1, doi: 10.1086/191216

Goad, M. R., Korista, K. T., De Rosa, G., et al. 2016, The Astrophysical Journal, 824, 11, doi: 10.3847/0004-637X/824/1/11

Graham, M. J., Djorgovski, S. G., Stern, D., et al. 2015, nat, 518, 74, doi: 10.1038/nature14143

Greene, J. E., Strader, J., & Ho, L. C. 2020, araa, 58, 257, doi: 10.1146/annurev-astro-032620-021835

Guo, H., Barth, A. J., & Wang, S. 2022, The Astrophysical Journal, 940, 20, doi: 10.3847/1538-4357/ac96ec

Heckman, T. M., & Best, P. N. 2014, araa, 52, 589, doi: 10.1146/annurev-astro-081913-035722

Henden, A. A., Levine, S., Terrell, D., et al. 2018, in American Astronomical Society Meeting Abstracts, Vol. 232, American Astronomical Society Meeting Abstracts #232, 223.06

Hernández Santisteban, J. V., Edelson, R., Horne, K., et al. 2020, Monthly Notices of the Royal Astronomical Society, 498, 5399, doi: 10.1093/mnras/staa2365

Homayouni, Y., Sturm, M. R., Trump, J. R., et al. 2022, The Astrophysical Journal, 926, 225, doi: 10.3847/1538-4357/ac478b

Homayouni, Y., Rosa, G. D., Plesha, R., et al. 2023, The Astrophysical Journal, 948, 85, doi: 10.3847/1538-4357/acc45a

Homayouni, Y., Kriss, G. A., De Rosa, G., et al. 2024, The Astrophysical Journal, 963, 123, doi: 10.3847/1538-4357/ad1be4

Horne, K., De Rosa, G., Peterson, B. M., et al. 2021, The Astrophysical Journal, 907, 76, doi: 10.3847/1538-4357/abce60

Hönig, S. F. 2014, The Astrophysical Journal Letters, 784, L4, doi: 10.1088/2041-8205/784/1/L4

Jha, V. K., Joshi, R., Chand, H., et al. 2022, mnras, 511, 3005, doi: 10.1093/mnras/stac109

Jiang, Y.-F., Green, P. J., Greene, J. E., et al. 2017, The Astrophysical Journal, 836, 186, doi: 10.3847/1538-4357/aa5b91

Kammoun, E. S., Dovčiak, M., Papadakis, I. E., Caballero-García, M. D., & Karas, V. 2021, The Astrophysical Journal, 907, 20, doi: 10.3847/1538-4357/abcb93

Kammoun, E. S., Papadakis, I. E., & Dovčiak, M. 2019, The Astrophysical Journal Letters, 879, L24, doi: 10.3847/2041-8213/ab2a72

Kara, E., Mehdipour, M., Kriss, G. A., et al. 2021, The Astrophysical Journal, 922, 151, doi: 10.3847/1538-4357/ac2159

Kara, E., Barth, A. J., Cackett, E. M., et al. 2023, The Astrophysical Journal, 947, 62, doi: 10.3847/1538-4357/acbcd3

Kaspi, S., Maoz, D., Netzer, H., et al. 2005, The Astrophysical Journal, 629, 61, doi: 10.1086/431275

Kelly, B. C. 2007, The Astrophysical Journal, 665, 1489, doi: 10.1086/519947

Korista, K. T., & Goad, M. R. 2001, The Astrophysical Journal, 553, 695, doi: 10.1086/320964

Korista, K. T., & Goad, M. R. 2019, Monthly Notices of the Royal Astronomical Society, 489, 5284, doi: 10.1093/mnras/stz2330

Korista, K. T., & Goad, M. R. 2019, mnras, 489, 5284, doi: 10.1093/mnras/stz2330

Kormendy, J., & Ho, L. C. 2013, araa, 51, 511, doi: 10.1146/annurev-astro-082708-101811

Kovačević, A. B., Radović, V., Ilić, D., et al. 2022, apjs, 262, 49, doi: 10.3847/1538-4365/ac88ce

Kraemer, S. B., Ho, L. C., Crenshaw, D. M., Shields, J. C., & Filippenko, A. V. 1999, The Astrophysical Journal, 520, 564, doi: 10.1086/307486

Lang, D., Hogg, D. W., Mierle, K., Blanton, M., & Roweis, S. 2010, aj, 139, 1782, doi: 10.1088/0004-6256/139/5/1782

Lang, D., Hogg, D. W., Mierle, K., Blanton, M., & Roweis, S. 2010, The Astronomical Journal, 139, 1782, doi: 10.1088/0004-6256/139/5/1782

Lawther, D., Goad, M. R., Korista, K. T., Ulrich, O., & Vestergaard, M. 2018, Monthly Notices of the Royal Astronomical Society, 481, 533, doi: 10.1093/mnras/sty2242

Lesser, M. 2015, The Publications of the Astronomical Society of the Pacific, 127, 1097, doi: 10.1086/684054

Lewin, C., Kara, E., Cackett, E. M., et al. 2023, The Astrophysical Journal, 954, 33, doi: 10.3847/1538-4357/ace77b

Lewin, C., Kara, E., Barth, A. J., et al. 2024, The Astrophysical Journal, 974, 271, doi: 10.3847/1538-4357/ad6b08

Li, T., Sun, M., Xu, X., et al. 2021, The Astrophysical Journal Letters, 912, L29, doi: 10.3847/2041-8213/abf9aa

Li, Y.-R., Wang, J.-M., Hu, C., Du, P., & Bai, J.-M. 2014, The Astrophysical Journal Letters, 786, L6, doi: 10.1088/2041-8205/786/1/L6

Li, Y.-R., Shangguan, J., Wang, J.-M., et al. 2025, The Astrophysical Journal, 988, 42, doi: 10.3847/1538-4357/addf40

Lira, P., Lawrence, A., O'Brien, P., et al. 1999, mnras, 305, 109, doi: 10.1046/j.1365-8711.1999.02388.x

Liu, T., Edelson, R., Santisteban, J. V. H., et al. 2024, Astrophys. J., 964, 167, doi: 10.3847/1538-4357/ad23e2

MacLeod, C. L., Ivezić, Z., Kochanek, C. S., et al. 2010, The Astrophysical Journal, 721, 1014, doi: 10.1088/0004-637X/721/2/1014

McCully, C., Turner, M., Volgenau, N., et al. 2018, LCOGT/banzai: Initial Release, 0.9.4, Zenodo

McHardy, I. M., Connolly, S. D., Peterson, B. M., et al. 2016, Astronomische Nachrichten, 337, 500, doi: 10.1002/asna.201612337

Montano, J. W., Guo, H., Barth, A. J., et al. 2022, The Astrophysical Journal Letters, 934, L37, doi: 10.3847/2041-8213/ac7e54

Morales, A. M., Miller, J. M., Cackett, E. M., Reynolds, M. T., & Zoghbi, A. 2019, The Astrophysical Journal, 870, 54, doi: 10.3847/1538-4357/aaeff9

Moran, E. C., Eracleous, M., Leighly, K. M., et al. 2005, aj, 129, 2108, doi: 10.1086/429522

Morgan, C. W., Hyer, G. E., Bonvin, V., et al. 2018, The Astrophysical Journal, 869, 106, doi: 10.3847/1538-4357/aaed3e

Morgan, C. W., Kochanek, C. S., Morgan, N. D., & Falco, E. E. 2010, The Astrophysical Journal, 712, 1129, doi: 10.1088/0004-637X/712/2/1129

Narita, N., Fukui, A., Yamamuro, T., et al. 2020, in Society of Photo-Optical Instrumentation Engineers (SPIE) Conference Series, Vol. 11447, Society of Photo-Optical Instrumentation Engineers (SPIE) Conference Series, 114475K, doi: 10.1117/12.2559947

Narita, N., Fukui, A., Yamamuro, T., et al. 2020, in Ground-based and Airborne Instrumentation for Astronomy VIII, ed. C. J. Evans, J. J. Bryant, & K. Motohara, Vol. 11447, International Society for Optics and Photonics (SPIE), 1199 – 1205, doi: 10.1117/12.2559947

Netzer, H. 2022, mnras, 509, 2637, doi: 10.1093/mnras/stab3133

—. 2025, mnras, 539, 3242, doi: 10.1093/mnras/staf671

Netzer, H., Goad, M. R., Barth, A. J., et al. 2024, The Astrophysical Journal, 976, 59, doi: 10.3847/1538-4357/ad8160

Neustadt, J. M. M., Kochanek, C. S., Montano, J., et al. 2024, The Astrophysical Journal, 961, 219, doi: 10.3847/1538-4357/ad1386

Oke, J. B. 1965, The Astrophysical Journal, 141, 6, doi: 10.1086/148086

Onken, C. A., Ferrarese, L., Merritt, D., et al. 2004, The Astrophysical Journal, 615, 645, doi: 10.1086/424655

Panagiotou, C., Kara, E., & Dovčiak, M. 2022, The Astrophysical Journal, 941, 57, doi: 10.3847/1538-4357/aca2a4

Partington, E. R., Cackett, E. M., Kara, E., et al. 2023, The Astrophysical Journal, 947, 2, doi: 10.3847/1538-4357/acbf44

Pei, L., Barth, A. J., Aldering, G. S., et al. 2014, The Astrophysical Journal, 795, 38, doi: 10.1088/0004-637X/795/1/38

Peterson, B. M. 1997, An Introduction to Active Galactic Nuclei (Cambridge, New York Cambridge University Press)

Peterson, B. M., & Horne, K. 2004, Astronomische Nachrichten, 325, 248, doi: 10.1002/asna.200310207

Peterson, B. M., Wanders, I., Horne, K., et al. 1998a, The Publications of the Astronomical Society of the Pacific, 110, 660, doi: 10.1086/316177

—. 1998b, The Publications of the Astronomical Society of the Pacific, 110, 660, doi: 10.1086/316177

Peterson, B. M., Balonek, T. J., Barker, E. S., et al. 1991, The Astrophysical Journal, 368, 119, doi: 10.1086/169675

Peterson, B. M., Alloin, D., Axon, D., et al. 1992, The Astrophysical Journal, 392, 470, doi: 10.1086/171447

Peterson, B. M., Berlind, P., Bertram, R., et al. 1994, The Astrophysical Journal, 425, 622, doi: 10.1086/174009

—. 2002, The Astrophysical Journal, 581, 197, doi: 10.1086/344197

Peterson, B. M., Ferrarese, L., Gilbert, K. M., et al. 2004, The Astrophysical Journal, 613, 682, doi: 10.1086/423269

Peterson, B. M., Bentz, M. C., Desroches, L.-B., et al. 2005, The Astrophysical Journal, 632, 799, doi: 10.1086/444494

Prince, R., Hernández Santisteban, J. V., Horne, K., et al. 2025, mnras, 541, 642, doi: 10.1093/mnras/staf983

Ren, G., Sun, M., Wang, J.-X., & Cai, Z.-Y. 2024, The Astrophysical Journal, 967, 25, doi: 10.3847/1538-4357/ad3d53

Rezaeitavabe, F., Rezaie, M., Modayil, M., et al. 2024, Science of The Total Environment, 912, 169028, doi: https://doi.org/10.1016/j.scitotenv.2023.169028

Saylor, D., Lepine, S., Crossfield, I., & Petigura, E. A. 2018, The Astronomical Journal, 155, 23, doi: 10.3847/1538-3881/aa96a4

Schill, R., Nelson, K. L., Harris-Lovett, S., & Kantor, R. S. 2023, Science of The Total Environment, 871, 162069, doi: https://doi.org/10.1016/j.scitotenv.2023.162069

Secunda, A., Jiang, Y.-F., & Greene, J. E. 2024, The Astrophysical Journall, 965, L29, doi: 10.3847/2041-8213/ad34b0

Sergeev, S. G., Doroshenko, V. T., Golubinskiy, Y. V., Merkulova, N. I., & Sergeeva, E. A. 2005, The Astrophysical Journal, 622, 129, doi: 10.1086/427820

Shakura, N. I., & Sunyaev, R. A. 1973a, Astronomy and Astrophysics, 24, 337

—. 1973b, aap, 24, 337

Shih, D. C., Iwasawa, K., & Fabian, A. C. 2003, mnras, 341, 973, doi: 10.1046/j.1365-8711.2003.06482.x

Slone, O., & Netzer, H. 2012, mnras, 426, 656, doi: 10.1111/j.1365-2966.2012.21699.x

Starkey, D. A., Huang, J., Horne, K., & Lin, D. N. C. 2022, Monthly Notices of the Royal Astronomical Society, 519, 2754, doi: 10.1093/mnras/stac3579

Steele, I. A., Smith, R. J., Rees, P. C., et al. 2004, in Ground-based Telescopes, ed. J. M. O. Jr., Vol. 5489, International Society for Optics and Photonics (SPIE), 679 – 692, doi: 10.1117/12.551456

Stetson, P. B. 1987, The Publications of the Astronomical Society of the Pacific, 99, 191, doi: 10.1086/131977

Strauss, M. A., & Huchra, J. 1988, aj, 95, 1602, doi: 10.1086/114757

Su, Z.-B., Cai, Z.-Y., Guo, H., Sun, M., & Wang, J.-X. 2025, arXiv e-prints, arXiv:2507.04359, doi: 10.48550/arXiv.2507.04359

Sun, M., Grier, C. J., & Peterson, B. M. 2018a, PyCCF: Python Cross Correlation Function for reverberation mapping studies, Astrophysics Source Code Library, record ascl:1805.032. http://ascl.net/1805.032

—. 2018b, PyCCF: Python Cross Correlation Function for reverberation mapping studies, Astrophysics Source Code Library, record ascl:1805.032. http://ascl.net/1805.032

Sun, M., Xue, Y., Trump, J. R., & Gu, W.-M. 2019, mnras, 482, 2788, doi: 10.1093/mnras/sty2885

Sun, M., Xue, Y., Brandt, W. N., et al. 2020, The Astrophysical Journal, 891, 178, doi: 10.3847/1538-4357/ab789e

Thim, F., Hoessel, J. G., Saha, A., et al. 2004, aj, 127, 2322, doi: 10.1086/382244

Tie, S. S., & Kochanek, C. S. 2018, mnras, 473, 80, doi: 10.1093/mnras/stx2348

Treu, T. 2010, araa, 48, 87, doi: 10.1146/annurev-astro-081309-130924

U, V., Barth, A. J., Vogler, H. A., et al. 2022, The Astrophysical Journal, 925, 52, doi: 10.3847/1538-4357/ac3d26

Vestergaard, M., & Peterson, B. M. 2006, The Astrophysical Journal, 641, 689, doi: 10.1086/500572

Vincentelli, F. M., McHardy, I., Hernández Santisteban, J. V., et al. 2022, mnras, 512, L33, doi: 10.1093/mnrasl/slac009

Vincentelli, F. M., McHardy, I., Cackett, E. M., et al. 2021, mnras, 504, 4337, doi: 10.1093/mnras/stab1033

Walsh, J. L., Minezaki, T., Bentz, M. C., et al. 2009, apjs, 185, 156, doi: 10.1088/0067-0049/185/1/156

Wandel, A., Peterson, B. M., & Malkan, M. A. 1999, The Astrophysical Journal, 526, 579, doi: 10.1086/308017

Welsh, W. F. 1999, The Publications of the Astronomical Society of the Pacific, 111, 1347, doi: 10.1086/316457

White, R. J., & Peterson, B. M. 1994, The Publications of the Astronomical Society of the Pacific, 106, 879, doi: 10.1086/133456

Winkler, H., Glass, I. S., van Wyk, F., et al. 1992, mnras, 257, 659, doi: 10.1093/mnras/257.4.659

Woo, J.-H., Cho, H., Gallo, E., et al. 2019, Nature Astronomy, 3, 755, doi: 10.1038/s41550-019-0790-3

Woo, J.-H., Treu, T., Barth, A. J., et al. 2010, The Astrophysical Journal, 716, 269, doi: 10.1088/0004-637X/716/1/269

Wrobel, J. M., Fassnacht, C. D., & Ho, L. C. 2001, The Astrophysical Journal Letters, 553, L23, doi: 10.1086/320508

Yu, Z., Kochanek, C. S., Peterson, B. M., et al. 2019, Monthly Notices of the Royal Astronomical Society, 491, 6045, doi: 10.1093/mnras/stz3464

Zaidouni, F., Kara, E., Kosec, P., et al. 2024, The Astrophysical Journal, 974, 91, doi: 10.3847/1538-4357/ad6771

Zhou, S., Sun, M., Feng, H.-C., et al. 2025, The Astrophysical Journal, 986, 137, doi: 10.3847/1538-4357/add468

Zu, Y., Kochanek, C. S., Kozłowski, S., & Udalski, A. 2013, The Astrophysical Journal, 765, 106, doi: 10.1088/0004-637X/765/2/106

Zu, Y., Kochanek, C. S., & Peterson, B. M. 2010, JAVELIN: Just Another Vehicle for Estimating Lags In Nuclei, Astrophysics Source Code Library, record ascl:1010.007. http://ascl.net/1010.007

Zu, Y., Kochanek, C. S., & Peterson, B. M. 2011, The Astrophysical Journal, 735, 80, doi: 10.1088/0004-637X/735/2/80